

1990

Thesis/Dissertation

A Comparison of OPTically Measured and Radar-Derived  
Horizontal Neutral Winds

Michael Stewart Christie

AFIT Student at: Utah State University

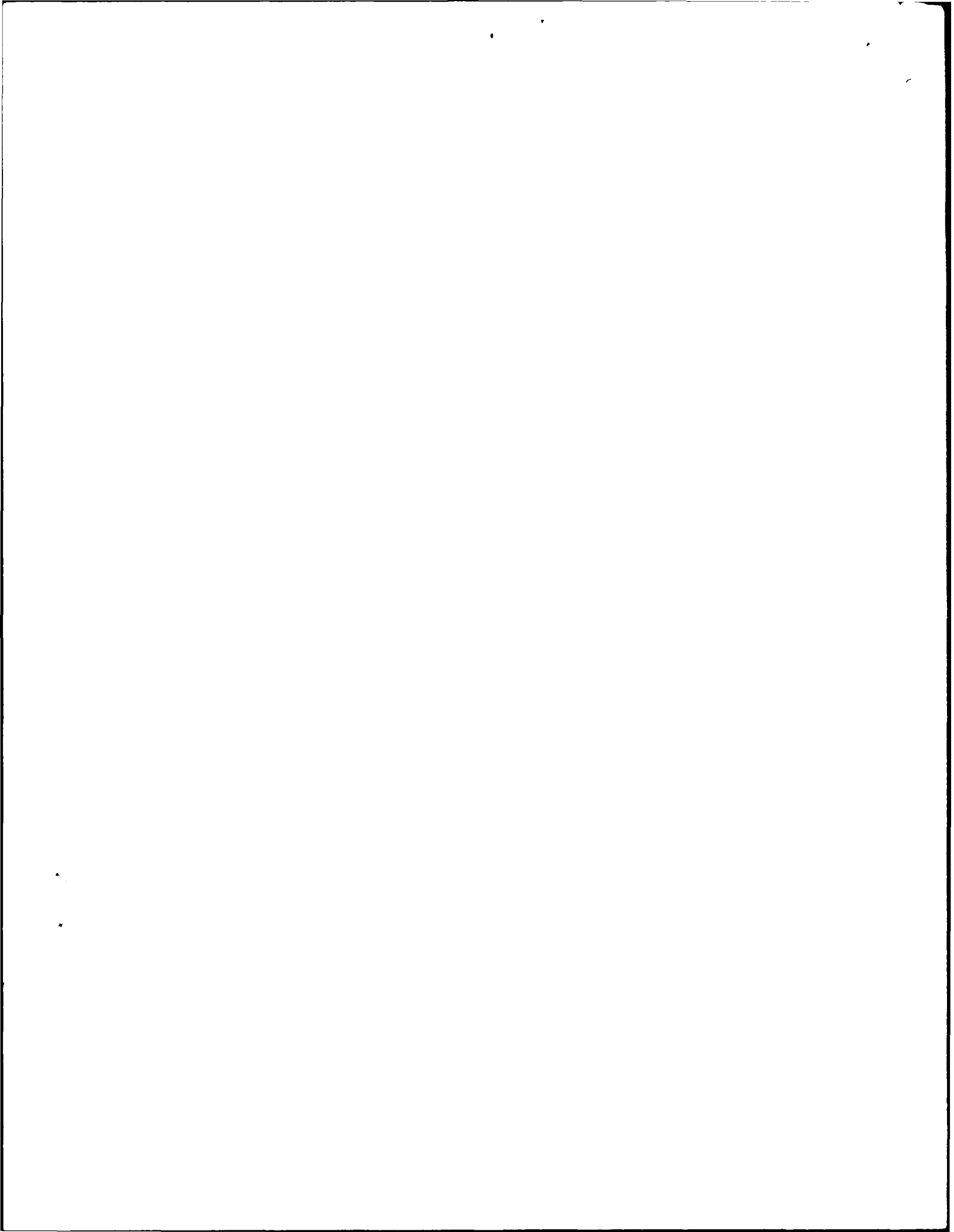
AFIT/CI/CIA -90-108

AFIT/CI  
Wright-Patterson AFB OH 45433

AD-A227 690

Approved for Public Release IAW AFR 190-1  
Distribution Unlimited  
ERNEST A. HAYGOOD, 1st Lt, USAF  
Executive Officer, Civilian Institution Programs

DTIC  
ELECTE  
OCT 24 1990  
S B D  
E



Copyright © Michael Stewart Christie 1990  
All Rights Reserved

A COMPARISON OF OPTICALLY MEASURED  
AND RADAR-DERIVED HORIZONTAL  
NEUTRAL WINDS

by

Michael Stewart Christie

A thesis submitted in partial fulfillment  
of the requirements for the degree

of

MASTER OF SCIENCE

in

Physics  
(Upper Atmospheric Physics)

Accession For	
NTIS GRA&I	<input checked="" type="checkbox"/>
DTIC TAB	<input type="checkbox"/>
Unannounced	<input type="checkbox"/>
Justification	
By _____	
Distribution/	
Availability Codes	
Dist	Avail and/or Special
A-1	

Approved:

*Vincent Wickwar*  
Dr. Vincent B. Wickwar

*Kent L. Miller*  
Dr. Kent L. Miller

*Gail E. Bingham*  
Dr. Gail E. Bingham

*Lawrence A. Pette*  
Dean of Graduate Studies



UTAH STATE UNIVERSITY  
Logan, Utah

1990

## ACKNOWLEDGEMENTS

I wish to thank Dr. Vincent B. Wickwar for allowing me to assist him with this research. His patience in taking many long hours to explain the myriad of difficult concepts was invaluable. His foresight throughout this project taught me the value of careful scientific analysis at times when deadlines threatened my resolve. I also wish to express my thanks to Dr. John W. Meriwether for taking the time to explain many details and nuances about the Fabry-Perot data used in this research and so crucial to it. I wish to thank the National Center for Atmospheric Research (NCAR), particularly Mr. Roy Barnes, and SRI International for prompt responses to request for and questions about data.

I would also like to thank Donice Loges-Simpson for her exceptional patience in dealing with the endless revisions and details associated with this manuscript. Without her, the document would not have been possible in its present form.

I would be remiss if I failed to thank my officemates, Major Willow Cliffswallow and Captain Michael Johnson. Their patience in helping me with course work was invaluable. The many long discussions regarding the physics of the upper atmosphere gave me an alternative point of view necessary to understand the complicated processes and equations involved in this area of physics.

To my friends and family, who never doubted I could complete this program even when I wasn't so sure, I am forever grateful. Finally, to my wife, Elsie, I cannot fully express my gratitude. Without her faith, support and sacrifice, none of this would have been possible. She gave me the kind support only a wife can give.

This research was in part supported by contract F49620-87-K-0007 from the Air Force Office of Scientific Research. The incoherent-scatter radar and Fabry-Perot data acquired under cooperative agreements and grants from the National Science Foundation, Division of Atmospheric Sciences, to SRI International and the University of Michigan. The data base at NCAR is also supported by the National Science Foundation, Division of Atmospheric Sciences.

Michael Stewart Christie

## TABLE OF CONTENTS

	Page
ACKNOWLEDGEMENTS . . . . .	ii
LIST OF TABLES . . . . .	v
LIST OF FIGURES . . . . .	vi
ABSTRACT . . . . .	ix
CHAPTER	
I. INTRODUCTION . . . . .	1
II. INSTRUMENTS . . . . .	9
2.1. Incoherent-Scatter Radar . . . . .	9
2.1.1. Densities . . . . .	10
2.1.2. Parallel Ion Velocities . . . . .	10
2.2. Fabry-Perot Interferometer . . . . .	11
III. DATA REDUCTION PROCEDURES . . . . .	14
3.1. Radar . . . . .	14
3.1.1. Diffusion . . . . .	14
3.1.2. Collision Frequency . . . . .	17
3.1.3. Neutral Atmosphere . . . . .	20
3.1.4. Plasma Density Gradients . . . . .	22
3.1.5. Temperature Gradients . . . . .	22
3.2. Fabry-Perot Interferometer . . . . .	23
3.2.1. Zero Velocity Determination and LOS Velocity Correction . . . . .	23
3.2.2. FPI Interpolation . . . . .	30
3.2.3. Earth Curvature Correction . . . . .	30
3.2.4. Resolving the Vector Neutral Wind . . . . .	36
3.2.5. Altitude . . . . .	39
IV. THE DATA . . . . .	43
V. DISCUSSION . . . . .	46
VI. CONCLUSIONS . . . . .	74

6.1. Results . . . . .	74
6.2. Topics for Further Research . . . . .	76
REFERENCES . . . . .	78
APPENDIX . . . . .	82

LIST OF TABLES

Table	Page
1. Comparisons of the Horizontal Neutral Winds Derived from the Radar Data Using MSIS-83 and MSIS-86 . . . . .	21
2. Comparison of Flat Earth Versus Curved Earth Correction in the Resolved Fabry-Perot Interferometer Data . . . . .	35
3. Data from the Radar and FPI Compared in this Study . . . . .	44

## LIST OF FIGURES

Figure		Page
1.1	An example of how ion flow along an inclined geomagnetic field line can respond to a horizontal neutral wind . . . . .	3
2.1	FPI scan positions . . . . .	12
3.1	Geometry used in the horizontal meridional wind calculation . . . . .	18
3.2	Assumed $T_r$ profile . . . . .	24
3.3	Plots showing the radar data (dashed) and the FPI data (solid) for 23-24 February 1984 for two independent data reductions . . . . .	26
3.4	Plot of the radar data and resolved FPI data for 23-24 February 1984 showing how the two independent reductions can affect the overall agreement between the radar and FPI . . . . .	27
3.5	Plot of two independent reductions of the data for 4 March 1987 showing differences in observed gradients . . . . .	28
3.6	Plot of resolved N-S FPI data for 4 March 1987 showing little difference between the two reductions . . . . .	29
3.7	Example of a possible arrangement of FPI scan positions in time . . . . .	31
3.8	Geometry used to calculate the range from the FPI to the observation point . . . . .	33
3.9	Geometry associated with the azimuth correction necessary due to a spherical Earth . . . . .	34
3.10	Geometry used to resolve the vector neutral wind . . . . .	37
3.11	Plots of the peak electron density altitude and peak dissociative recombination altitude for 16-17 March 1988 . . . . .	40
3.12	Plot summarizing the emission altitudes for particle precipitation and dissociative recombination . . . . .	41
5.1	Data from 23-24 February 1984 showing how changing $f$ at lower altitudes has little effect on the winds . . . . .	47
5.2	Scatter plot of the values of $f$ needed at 230 km ( $x$ -axis) versus that needed at 280 km ( $y$ -axis) . . . . .	49

5.3	Plot of radar data and FPI data from 4 March 1987 emphasizing the variability seen in the radar but not in the FPI . . . . .	50
5.4	Graph showing the range of factors needed to achieve the best agreement between the radar and FPI . . . . .	52
5.5	Graph of factors needed to achieve the best agreement between the radar and FPI for 1983, 1984 and 1988 for medium solar activity . . . . .	53
5.6	Graph showing the factors needed to achieve the best agreement between the radar and FPI for 1987, close to solar-cycle minimum . . . . .	54
5.7.	Plot of the 81-day average $F_{10.7}$ cm flux for the data in this study from the years 1983, 1984, 1987 and 1988 . . . . .	56
5.8	Graph showing the frequency of occurrence of Kp values for the data in this study . . . . .	57
5.9	Data from 23–24 February 1984 at 231 km showing how the best $f$ varies during the night . . . . .	58
5.10	Gradients in the FPI winds deduced from observations to the north and south on 23–24 February 1984 . . . . .	60
5.11	Data from 23–24 February 1984 showing representative error bars on the FPI and radar data . . . . .	61
5.12	Plots of data for 17–18 March 1988 showing the unusually low $f$ value required for agreement, $f = 1.0$ . . . . .	63
5.13	Plots of data for 17–18 March 1988 showing error bars . . . . .	64
5.14	Plots of the data for 26–27 February 1987 showing the unusually high value needed for agreement, $f > 5.1$ . . . . .	65
5.15	Plots showing the data of 26–27 February 1987 showing representative error bars . . . . .	66
5.16	FPI and radar neutral winds for the night of 4 March 1987 at three altitudes: 173, 228 and 283 km . . . . .	67
5.17	FPI and radar neutral winds for the night of 4 March 1987 with the associated error bars at three altitudes: 173, 228 and 283 km . . . . .	68

5.18	Plots of the horizontal neutral wind, parallel ion velocity and diffusion velocity for 4 March 1987 at 173 km . . . . .	70
5.19	Plots of the horizontal neutral wind, parallel ion velocity and diffusion velocity for 4 March 1987 at 228 km . . . . .	71
5.20	Plots of the horizontal neutral wind, parallel ion velocity and diffusion for 4 March 1987 at 283 km . . . . .	72

## ABSTRACT

A Comparison of Optically Measured  
and Radar-Derived Horizontal  
Neutral Winds

by

Michael S. Christie, Master of Science  
Utah State University, 1990Major Professor: Dr. Vincent B. Wickwar  
Department: Physics

Nighttime thermospheric winds for Sondrestrom, Greenland (~~66.99° N, 50.95° W,~~ 75° N) from 11 nights between 1983 and 1988, have been compared to learn about the  $O^+-O$  collision cross section and the high-latitude atomic oxygen density. The horizontal winds in the magnetic meridian were derived *indirectly* from incoherent-scatter radar (ISR) measurements on ion velocities antiparallel to the magnetic field and *directly* from Fabry-Perot interferometer (FPI) measurements of Doppler shifts of the (6300-Å) emission of atomic oxygen. In deriving the radar winds, the  $O^+-O$  collision frequency, which involves the product of the atomic oxygen density and the  $O^+-O$  collision cross section, was scaled by a factor of  $f$  that was varied from 0.5 to 5.1. On the basis of several arguments the altitude of the 6300-Å emission was assumed to be 230 km. The best agreement between the ISR and FPI winds was obtained when  $f$  was increased substantially, to between 1.7 and 3.4. If the average peak emission altitude were higher, these factors would be larger; if it were lower, they would be somewhat smaller. However, if the average altitude were substantially lower it would have been more difficult to have obtained agreement between the two techniques. If it were assumed, in agreement with *Burnside et al.* [1987], that the  $O^+-O$  collision cross section should be increased by a factor of 1.7, then any departure of  $f$  from that value would indicate a variation of the atomic oxygen density  $[O]$  from the value determined by the MSIS-86 model of the neutral atmosphere. The full range of  $[O]$  variation was then from 1/3 to 3 times the MSIS value, with the most frequently found factor being 1 during period of moderate solar activity ( $F_{10.7} > 100$ ) and 2 during periods of low solar activity ( $F_{10.7} \sim 70$ ), i.e., solar-cycle minimum. In addition,  $f$  and therefore  $[O]$  were often

found to vary significantly during the night. An increase was associated with the appearance of gradients in the FPI meridional wind, suggesting auroral activity as a common cause. Finally, superimposed on the radar wind, close to the time on a day when Kp increased from 2 to 4-, were two periods of a large-scale gravity waves.

(103 pages)

## CHAPTER I

### INTRODUCTION

In the last two decades much has been learned about the behavior of the horizontal neutral winds at  $F$ -region altitudes (200 to 300 km) in the thermosphere. The term "wind" is taken to mean large-scale motions of the neutral atmosphere. Additionally, to avoid confusion with meteorological definitions, for example, an eastward wind means from west to east. It has been found that winds can be caused by several processes: thermal (differential heating), solar wind interactions with the Earth's magnetic field in the polar cap and auroral zone causing  $\mathbf{E} \times \mathbf{B}$  drift of ions which drag the neutrals along; tides, waves propagating up from below; etc.

In the basic pattern, winds tend to blow away from the subsolar point, the hottest point of the thermosphere, to the coldest part, which occurs in the early morning or predawn sector. In addition, they tend to blow over the polar caps and zonally around the Earth at all latitudes. The neutral winds are strongly influenced by frictional forces and collisions with ions. Ions can exert a drag on the neutral wind [Rishbeth, 1972]. This "ion-drag" is a result of the Earth's magnetic field. Ions cannot move freely because their motion is strongly influenced by the geomagnetic field ( $\mathbf{B}$ ). They can move freely along (parallel to)  $\mathbf{B}$  like "beads on a string" but cannot easily move perpendicular to it except when an electric field is present. This is expressed quantitatively by the equation of motion for a charged particle (assuming  $E = 0$ ), the Lorentz force, as:

$$m \frac{d\mathbf{V}}{dt} = q\mathbf{V} \times \mathbf{B}. \quad (1.1)$$

Thus, ion drag can act to limit the neutral wind when flow is perpendicular to  $\mathbf{B}$  [Rishbeth, 1972]. However, ion drag can also act to enhance the neutral wind at high latitudes. This is a result of the  $\mathbf{E} \times \mathbf{B}$  drift of the geomagnetic field in the antisunward direction across the polar cap and sunward at lower latitudes [Schunk, 1988]. This process is called convection. Since it is roughly in the day-to-night direction within the polar cap, ions will tend to move with the neutrals "dragging" them along, this time accelerating them and increasing the neutral wind speed. Additionally, because the geomagnetic field is inclined, as ions and electrons move along perpendicular to  $\mathbf{B}$ , there will be a vertical component to their motion. This

vertical motion can have a significant role in the ion density distributions. Furthermore, returning to the wind, a poleward wind on the dayside forces ions down **B** (Figure 1.1a), lowering the ion number density by forcing the layer into a region where chemical reactions reduce the concentration. Conversely, an equatorward wind (Figure 1.1b) tends to maintain the ion concentration by elevating the layer above the region where chemical reactions deplete it [Rishbeth, 1972].

The equatorward wind is particularly important. It is obvious that solar ionization in the Earth's atmosphere stops at night. When this happens, these major chemical reactions:



reduce the ion densities [Schunk, 1983]. As previously discussed, wind-induced vertical plasma drifts are a major process in the maintenance of the nighttime ionosphere. However, the nighttime ion densities are still sharply reduced compared to those during the day.

Another significant process at *F*-region altitudes is ambipolar diffusion. The physical reasoning behind ambipolar diffusion is straightforward. In the case of a quasi-neutral ionospheric plasma, ions and electrons are moved together to prevent *large-scale* electric fields from setting up. The lighter, faster electrons will, however, separate slightly from the heavier, slower ions under the influence of gravity. As a result, a *small* polarization electric field sets up preventing any further separation between them. This is the process that prevents the large-scale electric field. The ions and electrons then move together, slightly separated, under the influence of gravity as well as density and temperature gradients, as expected in a quasi-neutral plasma [Schunk, 1983].

Near the *F*-region peak, ambipolar diffusion and chemical process are in competition with one another. Above the peak, ambipolar diffusion dominates, while below it, chemical processes dominate [Schunk, 1983]. Quantitatively, the coefficient for

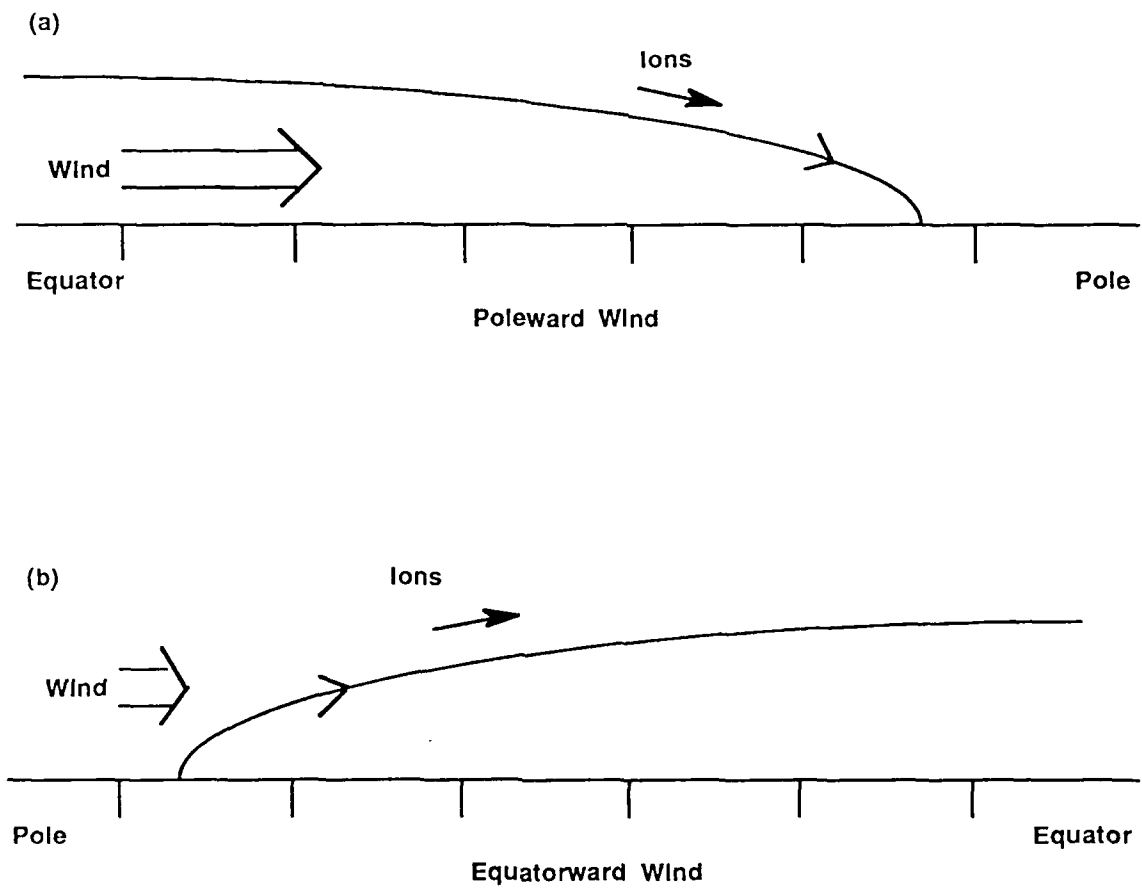


Figure 1.1. An example of how ion flow along an inclined geomagnetic field line can respond to a horizontal neutral wind. (a) shows how a poleward wind can act to move ions down  $\mathbf{B}$ . (b) shows how an equatorward wind can act to move ions up  $\mathbf{B}$ .

ambipolar diffusion is given by

$$D_a = \frac{2kT_p}{m_i \nu_{in}} \propto \frac{1}{\nu_{in}} \propto \frac{1}{n_n} \quad (1.6)$$

where  $k$  is Boltzman's constant,  $T_p$  is the plasma temperature,  $m_i$  is the ion mass,  $\nu_{in}$  is the ion-neutral collision frequency and  $n_n$  is the neutral density. The diffusion coefficient is ultimately proportional to the neutral density. As altitude increases, the neutral density decreases exponentially and, therefore,  $D_a$  increases. Thus, at high altitudes, diffusion dominates; at low altitudes, chemistry dominates. Because we are making observations at approximately 230 km, ambipolar diffusion is significant for our calculations of the winds from the radar observations. As we will see, diffusion is a significant term in our equation for the derivation of the wind from the radar data.

It is obvious that an understanding of the neutral wind is important because it affects the behavior of the ionosphere and its constituents. Clearly, the neutral wind affects the altitude of the  $F$ -layer and the ion number density. It is also important for understanding the combination of forces (solar, magnetospheric and lower atmospheric waves) that drive the upper atmospheric circulation.

Because winds are so important in the ionosphere, several methods of measuring them have been developed. The two of primary interest to this research are incoherent-scatter radar and the Fabry-Perot interferometer.

The incoherent-scatter radar (ISR) technique relies on the fact that particles (electrons) interact with a radar beam and act as individual scattering centers that scatter energy uniformly in all directions. This type of scatter is called incoherent because the phases of the scattered radio waves are random. Because the scattering cross section is very small, the return from the transmitted radar signal is weak. To obtain a strong enough signal to analyze, a powerful transmitter and large antenna are required. The returned signal can be analyzed to determine the winds because if the ions are moving, the returned signal will be Doppler shifted by an amount proportional to the ion motion [Evans, 1969]. We can then develop an equation for the horizontal neutral wind based on the radar measurements of the ion drift parallel to magnetic field lines (see Chapter III) [Wickwar, 1989; Wickwar et al., 1990].

Among the advantages of the radar are its ability to make measurements in any weather, night or day. The ISR has an added benefit in that it allows us to determine

altitude profiles of the observed parameters. This is by virtue of the fact that it can be pulsed. As with any monostatic radar, the time between when the pulse is transmitted and a signal is received gives the range of the scattering. This allows us to obtain altitude profiles subject to the resolution determined by the pulse length and signal processing methods.

The ISR technique allows us to measure ionospheric properties from which we can *derive* the horizontal neutral winds in the magnetic north-south direction. Another instrument, the Fabry-Perot interferometer (FPI), uses optical techniques to *measure* the Doppler shift of the OI ( $^1D - ^3P$ ) emission at 6300-Å in the airglow and aurora and thereby obtain the neutral winds directly [Hays and Roble, 1971; Hernandez and Roble, 1979b; Hernandez, 1980, Burnside et al., 1983]. The emission can be the result of dissociative recombination [Wickwar et al., 1974], energetic particle precipitation or hot thermal electrons [Wickwar and Kofman, 1984], or any combination of these.

The first attempts to measure upper atmospheric properties (winds and temperatures) [Armstrong, 1969] with the FPI were difficult due to the limitations of the equipment available at that time. But newer technology has made using the FPI more feasible for measuring both neutral winds and temperature [Hernandez, 1980; Hernandez, 1986]. The instrument itself is fairly simple in design. Two flat, semi-transparent mirrors are set a fixed distance apart. Any single wavelength of light incident on these mirrors, or plates, at some angle will undergo multiple reflections within the mirrors [Nagy et al., 1974; Hernandez and Roble, 1979b; Hernandez, 1980]. By virtue of the two mirrors, a constructive/destructive interference pattern is transmitted as a set of bright concentric rings against a dark background. An imaging system then resolves this pattern into a quantifiable spectrum [Hernandez, 1980]. For the 6300-Å emission, the spectrum is that of atomic oxygen, as previously stated. The Doppler shift of this spectrum will indicate the speed at which the neutral particles (atomic oxygen) are moving toward or away from the FPI. Hence, we have the component of the neutral wind in the line-of-sight (LOS) direction. By combining LOS winds from different directions, as discussed in Chapter III, a vector neutral wind may be resolved.

One disadvantage of this instrument is its inability to be pulsed like a radar. It does not produce altitude profiles. The wind we obtain represents an average over the emitting layer [Hernandez, 1980; Meriwether, 1983]. For chemical excitation (airglow), the peak of the emission profile is about 50 km below the *F*-region peak,

i.e., typically between 225 and 300 km altitude [Wickwar *et al.*, 1974]. For energetic particle excitation (aurora), the peak depends on the energy of the particles and the quenching. It is typically between 180 and 270 km [Rees and Roble, 1986; Meier *et al.*, 1989]. This question of emission altitude will be specifically addressed in Chapter III. However, the two instruments should reflect the same wind field because in principle, the variation of horizontal neutral wind with height above approximately 200 km is usually small [Meriwether, 1983] and can often be neglected. This is primarily due to viscosity. This term is expressed mathematically in the equation of motion as

$$\frac{\mu}{\rho} \times \frac{\partial^2 U_x}{\partial z^2} \quad (1.11)$$

where  $\mu$  is the coefficient of molecular viscosity,  $\rho$  the density and  $U_x$  the horizontal neutral wind velocity [Rishbeth, 1972]. We assume  $\mu$  is constant and  $\rho$  varies with  $z$ . At the upper boundary of the atmosphere it is usually assumed that the vertical momentum flux  $\partial U_x / \partial z$  is zero. From that it follows that  $U_x$  is constant at high altitudes. A more detailed treatment such as Richmond [1983] has shown that  $U_x$  should be constant down to altitudes approaching 200 km. Detailed calculations, such as those with the NCAR thermospheric global circulation model, show the horizontal wind almost constant above a region beginning between 200 and 300 km [e.g., Figures 12 and 13 in Johnson *et al.*, 1987]. Then, if the vertical velocity gradient is small due to viscosity, the bulk motion of neutrals in the emission region will be Doppler shifted due to the neutral wind velocity component along the line-of-sight of the FPI [Hays and Roble, 1971]. Therefore, the wind averaged over the emitting region is fairly indicative of the actual horizontal neutral wind of the layer (assuming small vertical gradients). There has been concern that the vertical shear of the horizontal neutral wind is not small, especially in auroral regions [Schunk and Walker, 1973; Wickwar *et al.*, 1984a]. This is something we will consider as well when we look at the data.

Another limitation to the accuracy of the Fabry-Perot technique is determining the location of the observed fringe for zero velocity. This important reference point is not known beforehand. It has to be determined from the observations.

Since we have two methods of measuring the horizontal neutral winds, one direct and one derived, the obvious question is how do they compare? In addition, if they differ, what can we learn about the two techniques in the upper atmosphere. That is the topic of this research.

In order to compare the radar-derived winds with those of the FPI, there are some variables that need to be known before the radar calculations can be made. Specifically, we need to know the ambipolar diffusion coefficient

$$D_a = \frac{k(T_e + T_i)}{m_i \nu_{in}} \quad (1.12)$$

(see Chapter III for a detailed derivation of this parameter), which depends on the ion-neutral collision frequency,  $\nu_{in}$ . This parameter is the Achilles heel of the radar calculation. The ion-neutral collision frequency is proportional to the product of the neutral density,  $n_n$  and the collision cross section,  $Q$ ,

$$\nu_{in} \propto n_n Q. \quad (1.13)$$

At *F*-region altitudes, the dominant neutral is atomic oxygen, and the major ion is  $O^+$ . The collision cross section we need is that of  $O^+$ -O. There have been attempts to obtain a value for  $Q$  [Dalgarno, 1958; Banks, 1966] using various techniques. Dalgarno [1958] deduced, based on theoretical estimates, values for  $Q$  to an accuracy within a factor of two. There have also been laboratory experiments designed to measure it. However, the necessary measurements are extremely difficult to make due to the high reactivity of atomic oxygen with the walls of the container. Therefore, these attempts have met with various levels of success. Stebbings *et al.* [1964] used cross-beam experiments to measure it in the laboratory to an uncertainty of 25%, while Carlson and Harper [1977] deduced it from ISR observations to an uncertainty of 40%. Roble [1975] deduced it by combining ionospheric observations and numerical models. Thomas and Williams [1975] also found, through observations of time lag response to changes in the electric field, that  $\nu_{in}$  needed to be increased. Djuth [private communication, 1990] as well found an increase was necessary through ionospheric heating experiments.

The collision frequency is not solely dependent on  $Q$ . The neutral atomic oxygen density,  $[O]$ , enters as well. It is not adequately known either. There are empirical models of the neutral atmosphere available that provide neutral densities, temperatures and composition, but they are empirical models, not simultaneous observations. Roble [1975] had to increase his model-predicted nighttime values of  $[O]$  by 50% at 120 km over those of the daytime values to get agreement with observation. Other neutral atmospheric models like Jacchia's [1971] and MSIS [Hedin *et al.*, 1977; Hedin, 1983, 1987] are more recent. They are generally very good on av-

erage but can vary significantly from observation on a day-by-day, or hour-by-hour basis.

By using these neutral models to calculate winds from ISR data, comparing them to FPI-measured winds and varying the product of the neutral oxygen density and the collision cross section to obtain the best match, new values of  $Q$  can be deduced by assuming MSIS is correct on average [Burnside *et al.*, 1983, 1987; Sipler and Hagan, 1989]. The FPI serves as a benchmark for the comparison. This type of experiment uses either the Jacchia or MSIS model in one form or another. Most of this experimentation agrees with the other results described above in that  $Q$  needs to be increased. For example, Burnside *et al.* [1987] found  $Q$  needed to be increased by a factor of 1.7 (70%).

Clearly, there is some ambiguity in  $[O]$  and  $Q$ . This means there is also uncertainty in  $\nu_{in}$  and  $D_a$ . Since  $D_a$  and  $\nu_{in}$  are important to all thermospheric and ionospheric models that include transport effects, we need to better understand the neutral density and collision cross section,  $Q$ . It is my intent in this research to see if any of the above findings apply to a high-latitude data set consisting of some 11 nights of overlapping ISR and FPI data. Comparisons of these two sets of wind data will help us learn more about the  $O^+-O$  collision cross section and neutral atomic oxygen density. In addition, because this type of comparison has not been done at such high latitudes before, new effects previously not observed may emerge.

Previous research with different data sets at different locations seems to indicate the ion-neutral collision frequency or  $[O]$  used to derive the radar neutral winds is either too low or has a rather large associated error [Thomas and Williams, 1975; Carlson and Harper, 1977; Burnside *et al.*, 1987; Wickwar, 1989; Sipler and Hagan, 1989; Djuth, private communication, 1990]. The above authors generally obtain the atomic oxygen density from some form of a neutral atmospheric model such as MSIS or Jacchia and assume it is representative of the actual densities. It is my intent in this thesis to see if these previous findings apply at high latitudes or what changes are needed in the analysis to improve them. It may also tell us about the behavior of the atomic oxygen at high latitudes. This, then, will tell us how well we can determine the winds with the radar. The ISR technique is important because of the clear, dark sky limitation of the FPI. The radar can help us fill in details about diurnal and seasonal variations which, in turn, reflect different combinations of solar and magnetospheric processes.

## CHAPTER II

### INSTRUMENTS

#### 2.1. Incoherent-Scatter Radar

The incoherent-scatter radar located at Sondre Stromfjord, Greenland, began operation in February 1983. The radar was previously located at Chatanika, Alaska. When it was moved to Sondrestrom, it was upgraded and its capability increased [Kelly, 1983]. The Sondrestrom location is  $66.987^{\circ}$  N,  $59.949^{\circ}$  W. Its present location anchors a meridional chain of incoherent-scatter radars that provide coverage from the equator to the pole. This makes it a prime instrument for studying magnetospheric, ionospheric and neutral atmospheric interactions.

The magnetic field at Sondrestrom has a geographic azimuth of  $-39^{\circ}$  (declination) to the north with an  $80^{\circ}$  dip angle at  $F$ -region altitudes [Kelly, 1983; Wickwar *et al.*, 1984b].

The normal operating parameters for the radar are as follows:

Frequency	1290 MHz
Pulse Length	$320 \mu$ or $60 \mu s$ and $320 \mu s$
Peak Power	4 MW

with an antenna diameter of 32 meters [Kelly, 1983; Wickwar *et al.*, 1984b].

For the data I am using, the radar was operated in one of several modes. In the simplest it was directed parallel to the local magnetic field. In the most complex it was used in a multi-position scan pattern comprised of 11 fixed position. The pairs of pointing directions were at elevation angles of  $30^{\circ}$ ,  $50^{\circ}$  and  $65^{\circ}$  to the north;  $30^{\circ}$  and  $50^{\circ}$  to the south; and parallel to the local magnetic field [Wickwar *et al.*, 1984b]. It is the last position that was used for this research.

The physical parameters that are derived from the radar data depend on: The sequence of the antenna positions, the sequence of the transmitted pulses and the sampling of the return signal [Wickwar, 1984]. For this reason, details of specific radar parameters are presented in the following subsections. The material for the succeeding sections was obtained from the catalog and header records which accompany the data tape from the incoherent-scatter data base at the National Center for Atmospheric Research (NCAR). Those records were written by the primary investigator, Dr. V. B. Wickwar.

### 2.1.1. Densities

The plasma densities were obtained from observations parallel to **B**. They were fully corrected for temperature ratio and Debye length. To get these, the raw densities were obtained from the actual radar power measurements. These raw densities are then corrected for temperature and Debye-length effects and smoothed as a function of altitude.

The raw density profile is obtained from the long-pulse data or is constructed using the data obtained from two pulse lengths. The short pulse data is appropriate to the small scale heights at low altitude. The long pulse data is appropriate to the longer scale heights in the *F*-region and has a much better signal-to-noise ratio. The combined raw density profile is corrected and smoothed.

### 2.1.2. Parallel Ion Velocities

The geophysical parameters are derived by fitting theoretical autocorrelation functions to an observed autocorrelation function via a non-linear least squares fit. *Wickwar et al.* [1981] gives details and references. The procedure to calculate these parameters apply from altitudes ranging from high in the *D*-region where ion-neutral collisions dominate (not to include negative ions), up through the *E* and *F*-regions.

The ion composition is assumed to be 75%  $\text{NO}^+$  and 25%  $\text{O}_2^+$  (a molecular mass of 30.5 AMU) in the *E*-region to predominantly  $\text{O}^+$  in the *F*-region. A smooth transition from molecular ions to  $\text{O}^+$  is assumed inbetween. These are reasonable estimates most of the time. Occasionally, however, the relative concentration of molecular ions is underestimated. When this occurs the effect is to underestimate the electron and ion temperatures. The deduced ion velocity is unaffected and the electron density is practically unaffected.

$\text{H}^+$  has not been seen in the Sondrestrom data over the operating range of altitudes and at the level of precision available. As a result, it is not taken into account.

The neutral density comes from a model. The model used for the  $\text{N}_2$ ,  $\text{O}_2$  and  $\text{O}$  densities is either *Jacchia* [*Jacchia*, 1971] or *MSIS* [*Hedin et al.*, 1977; *Hedin* 1983, 1987]. For our derivation of the winds, we use *MSIS-86*. These estimates are good, on average, provided there is no auroral heating. These models, specifically *MSIS*, do not reflect rapid changes in geomagnetic activity because they utilize the 24-hour

Ap variation. Additionally, they do not have as much data from the high latitude region as from mid to low latitudes [Hedin, 1983, 1987], especially during solar-cycle minimum. During magnetic storms, MSIS may also significantly overestimate the atomic oxygen density [Hecht *et al.*, 1989].

## 2.2. Fabry-Perot Interferometer

With the Sondrestrom radar facility is an optical facility. The FPI in use is a 10-cm aperture instrument with an etalon spacing of .624 cm used for the 1983-84 observations and 1.116 cm spacing for the observations after that [Meriwether and Shih, 1987]. The spacing was changed due to the decrease in exospheric temperature toward solar-cycle minimum. The smaller spacing corresponded to solar-cycle maximum when the 6300-Å signal was wide while the larger spacing corresponded to a decrease in the width for solar-cycle minimum. The different conditions required a spacing change to obtain the needed precision ( $\sim 15$  m/s) in determining the winds [Meriwether and Shih, 1987].

Observations were taken in eight directions separated in azimuth by  $45^\circ$  with a zenith angle of  $45^\circ$  (Figure 2.1). The stability of the instrument was deduced by observing a neon source. Neon was selected due to its proximity to the 6300-Å emission [Meriwether, private communication, 1989]. The neon source also serves as a baseline against which the zenith measurements are compared. The reason for doing this is the neon source, unlike the zenith measurement, is stable. It does not drift or fluctuate in wavelength throughout the course of the night. By combining the neon and vertical observations, the zero velocity reference can be established as a function of time and then used to correct the observed line-of-sight winds [Meriwether and Shih, 1987].

Additionally, the etalons in the FPI were maintained at a constant pressure of 1.7 PSI in an atmosphere of  $N_2$  gas [Meriwether, private communication, 1989]. This is important because the index of refraction between the etalon mirrors is dependent on the temperature, type and pressure of the gas in the cavity [Hernandez, 1986].  $N_2$  was chosen for its stability [Meriwether, private communication, 1989].

The 6300-Å emission in the airglow is due to dissociative recombination. The following reactions describe the dissociative recombination source:



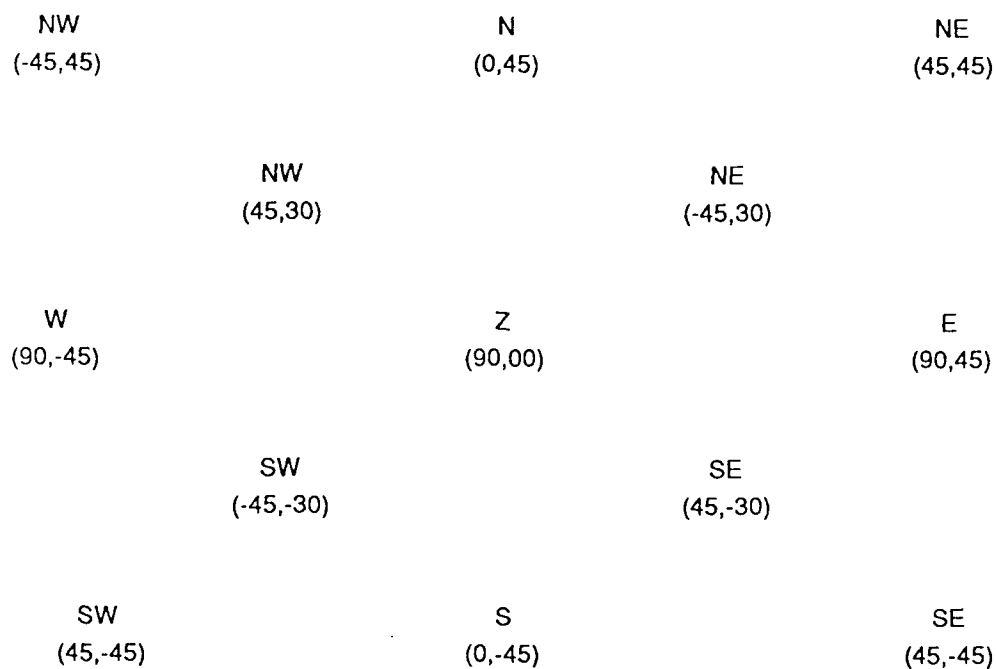


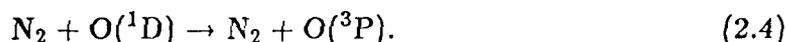
Figure 2.1. FPI scan positions. The numbers below the direction are the measured azimuth and zenith angles respectively. Azimuth is defined in the usual way, increasing from north toward east. The zenith angle is positive when in the direction of the azimuth; negative when in the opposite direction.



where the number in each equation represents the amount of energy given off by the specific reaction [Dalgarno and Walker, 1964; Wallace and McElroy, 1966]. In reaction 2.2, it is enough to excite one or both O atoms into the  $^1\text{D}$  state or to excite one of them into the  $^1\text{S}$  state from which they can cascade into the  $^1\text{D}$  state. The threshold for exciting the  $\text{O}(^1\text{D})$  state is 1.96 eV. An additional *minimal* source for the emission in the airglow is [Vallance-Jones, 1974]:



For the  $\text{OI}(^1\text{D}-^3\text{P})$  emission, the radiative lifetime is 147 seconds [Link *et al.*, 1981]. Because of this long time, the emission can be easily quenched by collisions and the effective lifetime can be significantly reduced. As a result, it is "quenched" in the laboratory and below about 300 km in the ionosphere due to loss of excitation energy through collisions with  $\text{N}_2$  [Peterson *et al.*, 1966; Vallance-Jones, 1974; Link *et al.*, 1981] as follows:



This emission, as described above, is focused on the etalon. The interference pattern emerging from the etalon was focused on a twelve channel photo-multiplier detector. The 12 channels are sampled to determine the emission spectrum. The Doppler shift of this spectrum provides the line-of-sight neutral wind. These line-of-sight winds can then be resolved into horizontal or vector velocities as discussed in Chapter III.

## CHAPTER III

## DATA REDUCTION PROCEDURES

## 3.1. Radar

There is a different form of data reduction required for each instrument involved in this comparison. Of the two, the radar data requires the most processing. We adopted a program developed by Dr. V. Wickwar while at SRI called MERWIND to derive the winds from the radar data. This program retrieves the data from an NCAR formatted record, performs the calculations outlined below and dumps the horizontal neutral winds at various altitudes to various plot files.

## 3.1.1. Diffusion

The horizontal neutral winds play an important role in the physics of the ionosphere. Ion motion parallel to the geomagnetic field arises from ambipolar diffusion as well as both horizontal and vertical neutral winds. We can measure this ion flow along  $\mathbf{B}$  by measuring the Doppler shift of the ISR return signal [Evans, 1969].

The process of ambipolar diffusion discussed in Chapter I will now be discussed mathematically. From Boltzmann's relation we can derive a generalized ion and electron momentum equation appropriate for the  $F$ -region that describes ion and electron motion (in MKS units),

$$n_i m_i \left[ \frac{\partial \mathbf{U}_i}{\partial t} + (\mathbf{U}_i \cdot \nabla) \mathbf{U}_i \right] + \nabla P_i + \nabla \cdot \boldsymbol{\tau} - en_i [\mathbf{E} + \mathbf{U}_i \times \mathbf{B}] - n_i m_i \mathbf{G} =$$

$$n_i m_i \Sigma \nu_{ie} (\mathbf{U}_e - \mathbf{U}_i) + n_i m_i \Sigma \nu_{in} (\mathbf{U}_n - \mathbf{U}_i) \quad (3.1.1)$$

[Schunk, 1983] where the following notation is used:

$n_{i,e}$ , the electron or ion number density,

$m_{i,e}$ , the ion or electron mass,

$\mathbf{U}_{i,e,n}$ , the vector velocity of the ions, electrons or neutrals,

$P_{i,e}$ , the ion or electron pressure,

$\boldsymbol{\tau}$ , the stress tensor,

$e$ , the elemental charge, negative for electrons,

$\mathbf{E}$ , the electric field,

$\mathbf{B}$ , the Earth's magnetic field,

$I$ , the inclination angle of the magnetic field,

$\mathbf{G}$ , the gravity vector,

$g$ , the acceleration due to gravity, such that  $\mathbf{G} = -g\hat{z}$ ,

$\nu_{in,en}$ , the electron or ion collision frequency with each neutral species,

$k$ , Boltzmann constant,

$T_{i,e}$ , the ion or electron temperature.

This ion momentum equation (3.1.1) can be simplified by making several initial assumptions:

- (1) The Magnetic Field is Vertical;
- (2) Steady State,  $\frac{\partial}{\partial t} = 0$ ;
- (3) Subsonic Flow,  $(\mathbf{U}_i \cdot \nabla)\mathbf{U}_i = 0$ ;
- (4) Charge Neutrality;
- (5) No Currents,  $\mathbf{U}_e = \mathbf{U}_i$ ;
- (6) No Stress,  $\tau = 0$ .

If we assume all the neutrals have the same velocity, then  $-n_i m_i \Sigma \nu_{in}(\mathbf{U}_i - \mathbf{U}_n) = -n_i m_i \nu_i(\mathbf{U}_i - \mathbf{U}_n)$  and equation (3.1.1) becomes

$$\nabla P_i - e n_i (\mathbf{E}_n + \mathbf{U}_i \times \mathbf{B}) - n_i m_i \mathbf{G} = -n_i m_i \nu_i [\mathbf{U}_i - \mathbf{U}_n]. \quad (3.1.2)$$

For a horizontally stratified ionosphere, the one-dimension momentum equation parallel to the magnetic field for ions is

$$\frac{\partial P_i}{\partial z} - e n_i E + n_i m_i g = -n_i m_i \nu_i (U_i - U_n), \quad (3.1.3)$$

and where the equation of state for each ion type is

$$P_i = n_i k T_i. \quad (3.1.4)$$

$U_i$  and  $U_n$  are the components of the ion and neutral velocity, respectively, parallel to the magnetic field. When (3.1.4) is substituted into the ion momentum equation (3.1.3) we obtain

$$kT_i \frac{\partial n_i}{\partial z} + n_i k \frac{\partial T_i}{\partial z} - en_i E + n_i m_i g = -n_i m_i \nu_i (U_i - U_n). \quad (3.1.5)$$

A similar result can be obtained for the electrons,

$$kT_e \frac{\partial n_e}{\partial z} + n_e k \frac{\partial T_e}{\partial z} + en_e E + n_e m_e g = -n_e m_e \nu_e (U_e - U_n). \quad (3.1.6)$$

We can now combine the ion and electron momentum equations (3.1.5) and (3.1.6) to obtain

$$k(T_i + T_e) \frac{\partial n}{\partial z} + nk \frac{\partial}{\partial z} (T_i + T_e) + nm_i g = -nm_i \nu_i (U_i - U_n). \quad (3.1.7)$$

Where we use the fact that the mass of the electron,  $m_e$ , is much less than that of the ion,  $m_i$ . We also use our assumption of charge neutrality ( $n_e = n_i = n$ ). Additionally, we realize that the contribution to the change in momentum as a result of electron-neutral collisions is small compared with ion-neutral collisions. Solving the combined momentum equation (3.1.7) for  $U_i$ , the parallel ion velocity becomes

$$U_i = U_n - \frac{k(T_e + T_i)}{m_i \nu_i} \left[ \frac{1}{n} \frac{\partial n}{\partial z} + \frac{1}{(T_e + T_i)} \frac{\partial (T_e + T_i)}{\partial z} + \frac{m_i g}{2kT_p} \right]. \quad (3.1.8)$$

Equation (3.1.8) is for one ion species only. Obviously there may be more than one ion present in what the radar is measuring as  $U_i$ . Therefore,  $U_i$  is essentially an average velocity of all the ions observed in motion parallel to  $\mathbf{B}$ . If  $q$  is taken to be the fraction of the ion present, we can approximate this measured  $U_i$  by using  $\langle m_i \rangle = \sum q_i m_i$  for the average ion mass and  $\langle m_i \nu_i \rangle = \sum q_i m_i \nu_i$  for the average  $m_i \nu_i$ .  $q_i$  is provided by a model [Wickwar *et al.*, 1990]. So,

$$D_a = \frac{k(T_e + T_i)}{\langle m_i \nu_i \rangle} \quad (3.1.9)$$

the ambipolar diffusion coefficient [Wickwar, 1989],

$$H_p = \frac{2kT_p}{\langle m_i \rangle g} \quad (3.1.10)$$

the plasma scale height and

$$T_p = \frac{1}{2}(T_e + T_i) \quad (3.1.11)$$

is the plasma temperature. In actuality the field line is inclined at angle  $I$ , the dip angle, as indicated in Figure 3.1. The parallel ion velocity, equation(3.1.8), must be corrected for this. If we take the diffusion velocity in the vertical, or  $\hat{z}$  direction, to be

$$U_d = -D_a \left[ \frac{1}{n} \frac{\partial n}{\partial z} + \frac{1}{T_p} \frac{\partial T_p}{\partial z} + \frac{1}{H_p} \right] \quad (3.1.12)$$

and,  $U_n$  to be the horizontal neutral velocity, positive toward magnetic north, then the parallel ion velocity corresponding to equation (3.1.8) becomes

$$U_i = -U_n \cos I + U_d \sin I. \quad (3.1.13)$$

Solving the parallel ion velocity equation (3.1.13) for  $U_n$  and rearranging,

$$U_n = -\frac{U_i}{\cos I} - D_a \tan I \left[ \frac{1}{n} \frac{\partial n}{\partial z} + \frac{1}{T_p} \frac{\partial T_p}{\partial z} + \frac{1}{H_p} \right] \quad (3.1.14)$$

[Wickwar, 1989], we obtain the fundamental equation used to derive the horizontal neutral wind from the radar observations. We can see from equation (3.1.13) that parallel ion velocities,  $U_i$ , originate from two sources: ambipolar diffusion and horizontal neutral winds as previously discussed.

With the use of the MSIS model [Hedin, 1983; 1987] and the horizontal neutral wind equation (3.1.14), calculations can be made using measurements of the ion motion parallel to the magnetic field. The density, ion and electron temperatures and parallel ion velocity profiles are all obtained from the ISR measurements. Equation (3.1.14) for the horizontal neutral wind is then used. A discussion of how the various terms in (3.1.14) are calculated follows.

### 3.1.2. Collision Frequency

The ion-neutral collision frequency,  $\nu_{in}$ , is determined by combining contributions from each of the ions  $O^+$ ,  $NO^+$  and  $O_2^+$  with the neutrals  $N_2$ ,  $O_2$  and  $O$ . For example,  $O^+$  is combined as:  $O^+ - O$ ,  $O^+ - N_2$  and  $O^+ - O_2$  to get  $\nu_{O^+}$ . This is done using the respective collision frequencies tabulated in Schunk and Walker [1973], Schunk and Nagy [1978] and Schunk [1983, 1988] and densities obtained

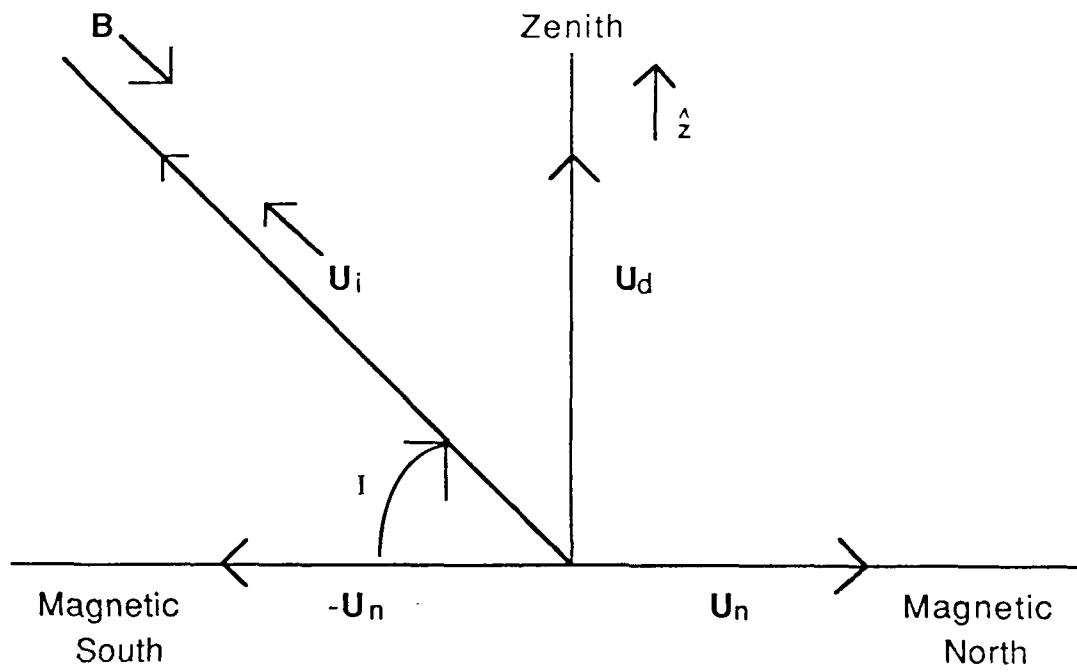


Figure 3.1. Geometry used in the horizontal meridional wind calculation [adapted from Wickwar, 1989].

from the neutral atmosphere. For example,

$$\nu_{O^+-N_2} = (\text{constant})(Q_{O^+-N_2})(\text{density of } N_2) = 6.82 \times 10^{-10}[N_2] \quad (3.1.15)$$

for  $[N_2]$  in  $\text{cm}^{-3}$ .  $Q_{O^+-N_2}$  represents the collision cross section for momentum transfer. The collision frequencies for each ion,  $\nu_{O^+}$ ,  $\nu_{NO^+}$  and  $\nu_{O_2^+}$  are simply the sum of the respective ion collision frequency with each of the neutrals' or simply

$$\nu_i = \sum \nu_{in} \quad (3.1.16)$$

the sum of the collision frequency of ion  $i$  with neutral  $n$ . These collision frequencies for each ion are then combined based on the ion concentration at a particular altitude. The concentration for  $O^+$  is obtained from the ISR data using an assumed ion composition profile, the same profile used in reducing the ISR data [Wickwar *et al.*, 1990]. Given the  $O^+$  concentration, the  $NO^+$  concentration is assumed to be 75 percent of what is left over and  $O_2^+$  is the other 25%. For example, if the concentration of  $O^+$  is given as 50%, then the  $NO^+$  concentration will be  $.75(1-.5) = 37.5\%$  and that for  $O_2^+$  will be  $1-(.875) = 12.5\%$ . Or generally, if we take  $q_i$  to be the fraction ion  $i$  is of the total ion concentration and define  $q_{O^+} = q$ , then  $q_{NO^+} = 0.75 * (1 - q)$  and  $q_{O_2^+} = 0.25 * (1 - q)$ . These concentrations are then multiplied by the respective collision frequencies and summed to give the total or average ion-neutral collision frequency

$$\langle \nu_i \rangle = q_{O^+}\nu_{O^+} + q_{NO^+}\nu_{NO^+} + q_{O_2^+}\nu_{O_2^+}. \quad (3.1.17)$$

We assume molecular ions below 150 km (75%  $NO^+$ , 25%  $O_2^+$ ), atomic ions above 250 km ( $O^+$  only) with a height-dependent variation of composition in between.

One additional calculation is made using the individual ion collision frequencies,  $\nu_{O^+}$ ,  $\nu_{NO^+}$  and  $\nu_{O_2^+}$ . This calculation is for the product of the ion mass and the ion-neutral collision frequency,  $m_i\nu_{in}$ . This is essentially the same calculation as described above except the ion mass now enters into the sum of the products such that

$$\langle m_i\nu_i \rangle = \sum q_i m_i \nu_{in}. \quad (3.1.18)$$

Given the  $\langle m_i\nu_i \rangle$ , the diffusion coefficient  $D_a$  can be calculated.

A new feature has been added to this calculation in MERWIND. Because  $\nu_{O^+-O} \propto [O]Q$  as discussed in Chapter I and in equation (3.1.15), a multiplicative factor ( $f$ ),

was added to this term such that  $\nu_{O^+ - O} \propto f[O]Q$ . This facilitates changing the size of this product so we can obtain the best possible agreement with the FPI winds. This follows a similar procedure used by *Burnside et al.* [1987].

### 3.1.3. *Neutral Atmosphere*

One of the major modifications to the program that calculates the horizontal neutral wind from the radar data was to incorporate the 1986 version of the MSIS (Mass Spectrometer/Incoherent Scatter) [*Hedin, 1987*] empirical model of the neutral atmosphere. This was done to take advantage of some of the changes made to MSIS-83 and designated MSIS-86. The model still produces the neutral temperatures and densities needed to calculate the horizontal neutral winds. It represents seasonal, longitudinal (UT), semi-annual and solar activity effects as well as local time variations in both the high (polar cap) and low latitude regions during magnetically quiet and disturbed periods [*Hedin, 1987*]. One modification was the inclusion of atomic nitrogen to the other previously included neutrals: N<sub>2</sub>, O<sub>2</sub>, He, O, H and Ar. The updated model also includes additional data from various sources including the Dynamics Explorer satellites.

The base of the model is still at 85 km, which we can extrapolate down to 60 km in MERWIND. However, the altitudes of interest to this research are above the 85 km value so the details of the extrapolation to lower altitudes will not be discussed.

There are several important points to note regarding the model. First, it is based on actual data. It gives a realistic description of neutral density and temperature in the region of interest. Second, the model can represent magnetic activity effects by using either the daily magnetic index, *Ap*, or the 3 hour, *ap* index. We use the daily *Ap* index. Third, the model atmosphere is recalculated for every data record because the solar zenith angle changes. Fourth, since molecular oxygen is important low down, the O<sub>2</sub> modelling is based on direct measurements by mass spectrometer and atmospheric absorption of Extreme Ultra Violet (EUV) radiation rather than derived from chemistry arguments [*Hedin, 1987*]. Fifth, the MSIS model is the internationally agreed upon model comprising part of the COSPAR model of the neutral atmosphere.

For a more detailed description of how the modelling is done, see *A. E. Hedin* [1983, 1987] listed in the references. Table 1 gives a comparison of the radar derived winds between the two models, MSIS-83 and MSIS-86. Clearly, there is a difference, but it is very small.

Table 1. Comparisons of the Horizontal Neutral Winds Derived from the Radar Data Using MSIS-83 and MSIS-86. The Wind and Error are from Calculations of the Horizontal Neutral Wind made Using the Neutral Composition, Density and Temperature from the Respective Models. The Last Column Labeled '% Change' is how much of a Change Occurred in the Wind Speed as a Result of the New Model. All Dates and Times are in UT.

Model Comparisons						
DATE (YYMMDD)	TIME (HHMM)	ALT (km)	MSIS-83 WIND (m/s)	MSIS-86 WIND (m/s)	CHANGE 86-83 (m/s)	% CHANGE MSIS-86
831206	0005	228	-202.0	-195.2	6.8	-3.48%
831206	2029	228	332.1	344.4	12.3	3.57%
840224	0033	231	-71.4	-71.2	0.2	-0.28%
840224	2032	231	295.9	297.9	2.0	0.67%
840223	0838	231	-122.6	-128.2	-5.6	4.37%
840223	0330	227	-321.9	-325.8	-3.9	1.20%
870226	0829	228	-218.5	-217.5	1.0	-0.46%
870226	0217	228	-284.3	-281.4	2.9	-1.03%

### 3.1.4. Plasma Density Gradients

The vertical density gradient was calculated using a parabolic fit to the natural logarithm of the density profile. The parabolic fit works well over half a scale height in altitude with data points every four to nine kilometers. This method generates a smooth density curve that is easily differentiated.

### 3.1.5. Temperature Gradients

The measured ion and electron temperatures are handled differently partly because those data points are separated by 50 to 60 km. A B-spline is fitted using several knots located between the mesopause and upper thermosphere. The spline then provides smooth and continuous profiles of electron and ion temperatures, and of their first derivatives, over the same altitude range as the density profile. The spline gives us temperature values and derivatives at the density altitudes.

To completely overlap the range of density points, the temperature profiles are extended both above and below the measured values. This gives a reasonable estimate of temperatures outside the measured ranges. To extend the values below the measured range, new values are added as follows:

<u>Alt (km)</u>	<u><math>T_e</math> (°K)</u>	<u><math>T_i</math> (°K)</u>	<u>Uncert</u>
105	245	245	$T_e/20$
120	395	395	$T_e/20$

Above these levels the actual data points are used. For a data point to be considered good and coded as such, on the data record that MERWIND then retrieves, it must pass several tests. First, the reduced chi square fit must be between 0.4 and 1.6. Second, the uncertainty on  $T_e$  and  $T_i$  must each be less than 25%. Third, the difference in the radar velocity found by two different techniques must be less than 80 m/s. And finally, the temperatures must be above 100° K. If there is a bad point among the good ones in the profile, it is rejected and replaced by a point midway between the surrounding good points.

Another point 25 km above the altitude of the highest good point is added based on that point's value. The uncertainty is also based on the last good point. A spline fit is then made to these modelled and measured temperatures. A weighting of  $(1/\sigma)^2$ , where  $\sigma$  is the uncertainty, is used at each point. The altitudes and temperatures of these points (knots) through which the spline will be fitted are saved (up to 8).

If there are fewer than three radar-measured temperatures, the ion and electron temperatures are constructed from a neutral temperature profile that is calculated from the exospheric temperatures,  $T_\infty$  (as generated from MSIS), obtained from a running average over the last 20 records (or over however many are available). In this case, the following assumptions are made:

- 1)  $T_n = T_\infty - (T_\infty - T_{120})e^{-s(h-120)}$ , where  $h$  = altitude and  $s = 0.02$ ;
- 2)  $T_i = T_n$ ;
- 3)  $T_e/T_i = T_r$ , as shown in Figure 3.2.

The uncertainties are all set to 1 in this case.

At this point, the spline smooth fitting procedure is applied using the eight knots to interpolate temperatures to the altitudes of the density points between 105 to 700 km.

Once this profile is generated, the temperature gradients are calculated based on:

$$\nabla T_p = \frac{1}{2} \left[ \frac{\partial T_e}{\partial z} + \frac{\partial T_i}{\partial z} \right]. \quad (3.1.19)$$

This term is then included in the meridional wind equation (3.1.14).

### 3.2. Fabry-Perot Interferometer

The FPI requires less actual manipulation than the radar because it measures the LOS winds directly. Prior to processing, all data are screened for clouds and small zenith angles that may adversely effect the data. Then the reduction is begun. With the exception of the zero velocity determination and LOS correction, all processing is done via programs FPIRED and WNDVEC.

#### 3.2.1. Zero Velocity Determination and LOS Velocity Correction

The (FPI) data had to undergo several modifications before being provided to us for comparison to the radar-derived horizontal neutral winds. The raw data consisted of relative line-of-sight velocities and associated error bars.

The LOS velocities ( $V_{LOS}$ ) can be corrected to zero in a three-step process [J. W. Meriwether, private communication, 1989]. First, a polynomial based on the time ( $t$ ) is fitted to the neon calibration measurements, which indicate the instrument stability,

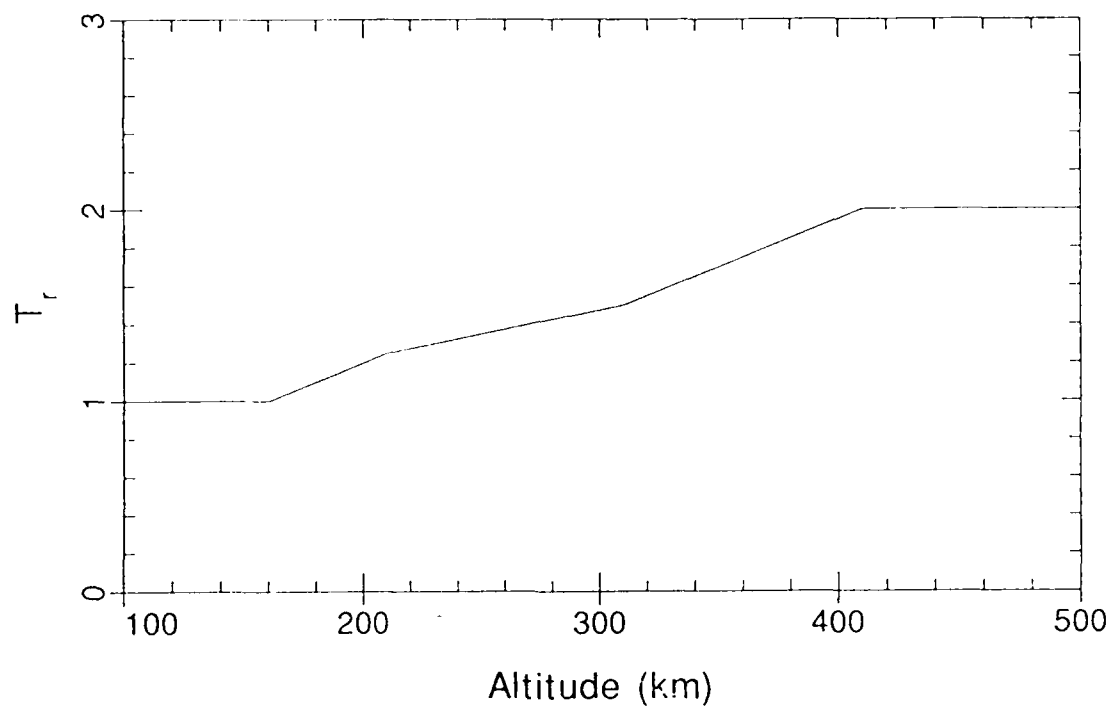


Figure 3.2. Assumed  $T_r$  profile. These  $T_r$  values are used when constructing the temperatures needed for the radar calculation of the neutral wind on those occasions without temperature observations.

$$P(t) = a + bt + ct^2 + dt^3 + \dots \quad (3.2.1)$$

Typically, a third order fit was found to give a smooth, slowly varying fit to the data points.

Once this curve representing how the FPI wavelength stability varies during the night is defined, it can be fitted to the zenith velocities. Although there may be periods of vertical winds, it is assumed that during a night the net vertical wind is zero. The weighted average,  $A$ , of the difference or offset between the zenith observations,  $y_i$  and the polynomial,  $P(t_i)$  is given by

$$A = \frac{\sum_{i=1}^n \left( \frac{P(t_i) - y_i}{\sigma_i^2} \right)}{\sum_{i=1}^n \left( \frac{1}{\sigma_i^2} \right)}, \quad (3.2.2)$$

where  $\sigma_i$  is the uncertainty of  $y_i$ . This expression for the offset  $A$  is equivalent to a least squares fit of  $P(t)$  to the zenith data points  $y_i$ . This fit can be refined by comparing  $P(t) + A$  to the  $y_i$  and dropping any of the  $y_i$  that differ from this curve by more than two standard deviations. A new value of  $A$  can then be found. This fit then provides the zero velocity baseline for the Fabry-Perot. The offset can be then applied to each measured LOS velocity according to:

$$V_{RLOS} = V_{LOS} - A, \quad (3.2.3)$$

where  $V_{RLOS}$  is the corrected LOS velocity. In the case of the zenith observations, an estimate of vertical velocities is given by  $v_{zen} = y_i - A$ .

It is important to note that this zero velocity determination described above is of critical importance to the data analysis. This is illustrated in Figures 3.3 through 3.6. Figures 3.3 and 3.5 show the radar data as the dashed line and the FPI observations to the north and south plotted separately using two independent FPI data reductions and zero velocity determinations. The top reduction in both figures was done by Dr. Rick Niciejewski (R. N.) of the University of Michigan while the lower plot was done by Dr. John Meriwether (J. M.) of GL. Figures 3.3 and 3.5 show significant differences in the FPI north and south observations. Figures 3.4 and 3.6 show the resolved FPI and radar data. The different reductions shown in Figure 3.4 lead to significant differences in the FPI velocities, the largest being 50

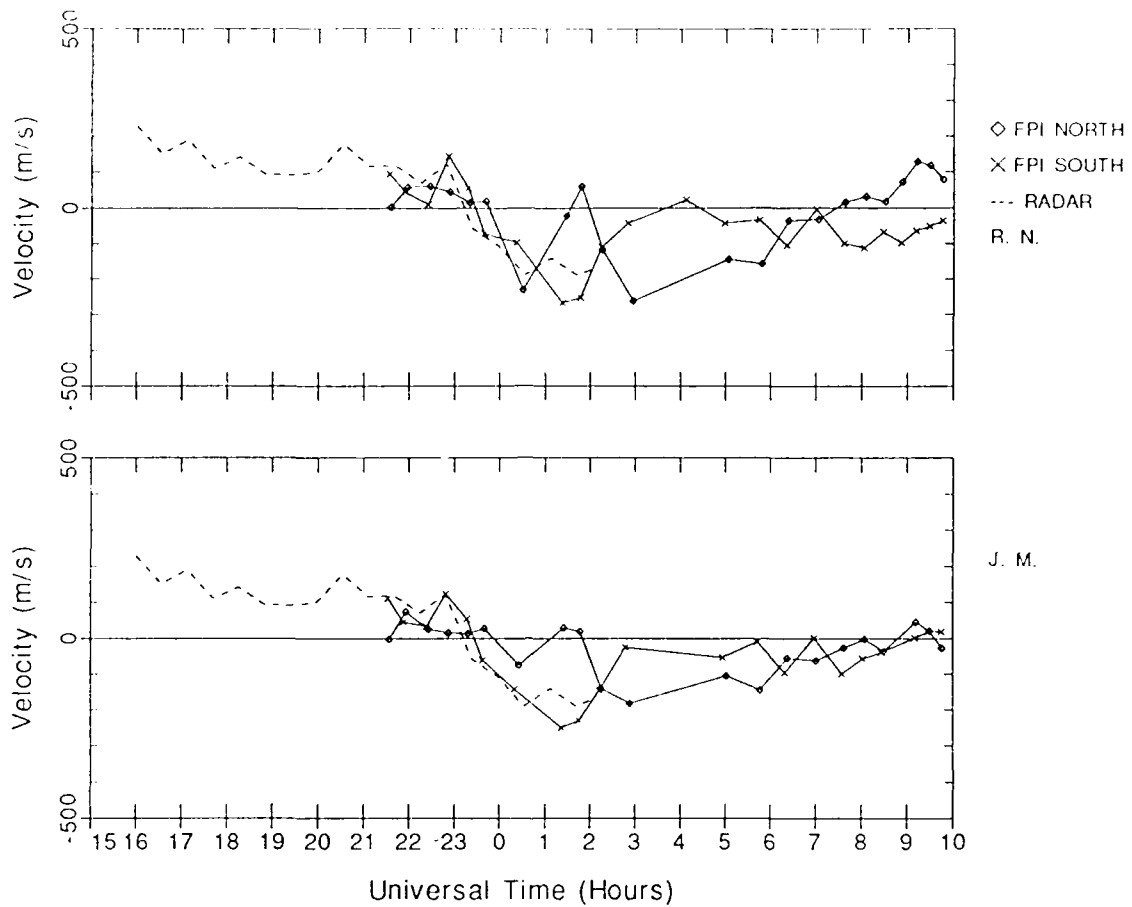


Figure 3.3. Plots showing the radar data (dashed) and the FPI data (solid) for 23–24 February 1984 for two independent data reductions. Clearly there are significant differences, reaching 50 m/s, in the FPI north and south observations especially after 00 UT. The altitude for the radar winds is 231 km and  $f = 1.7$ .

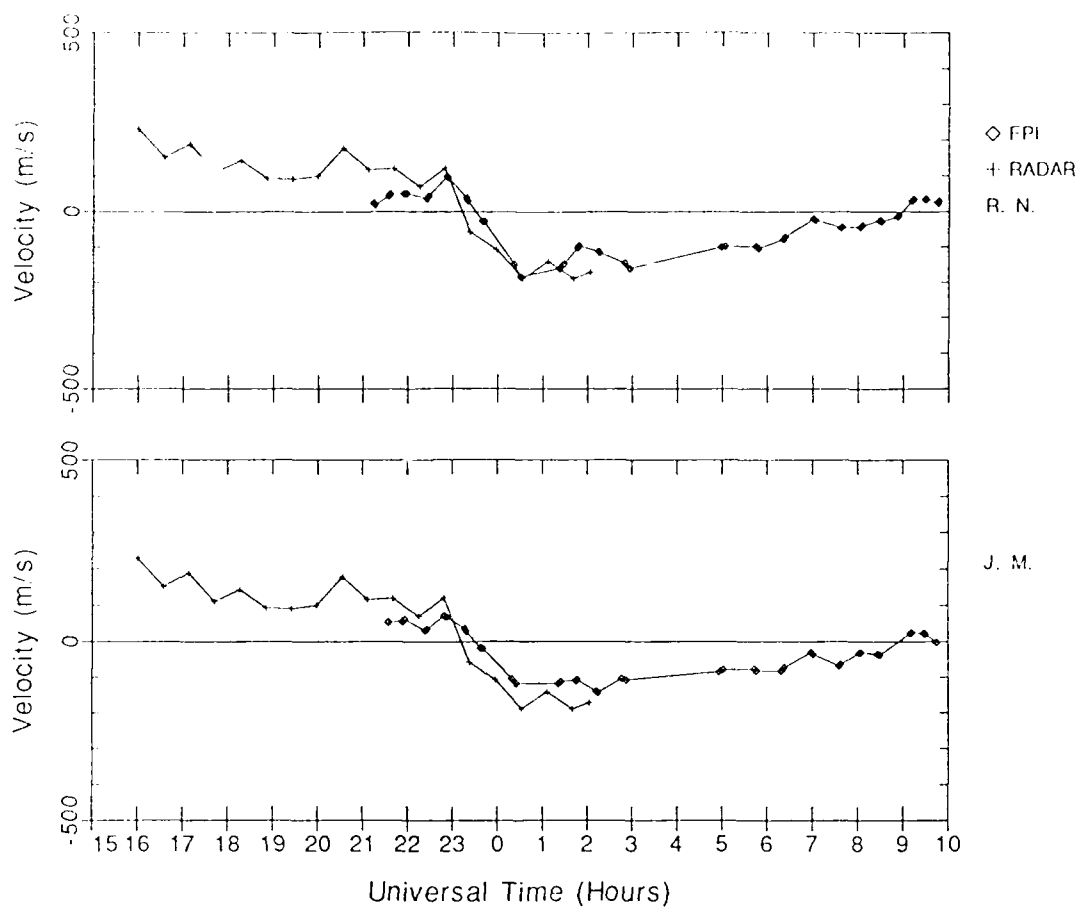


Figure 3.4. Plot of the radar data and resolved FPI data for 23-24 February 1984 showing how the two independent reductions can affect the overall agreement between the radar and FPI. While usually smaller, the difference at 0030 UT is approximately 50 m/s. The altitude of the radar plots is 231 km for  $f = 1.7$ .

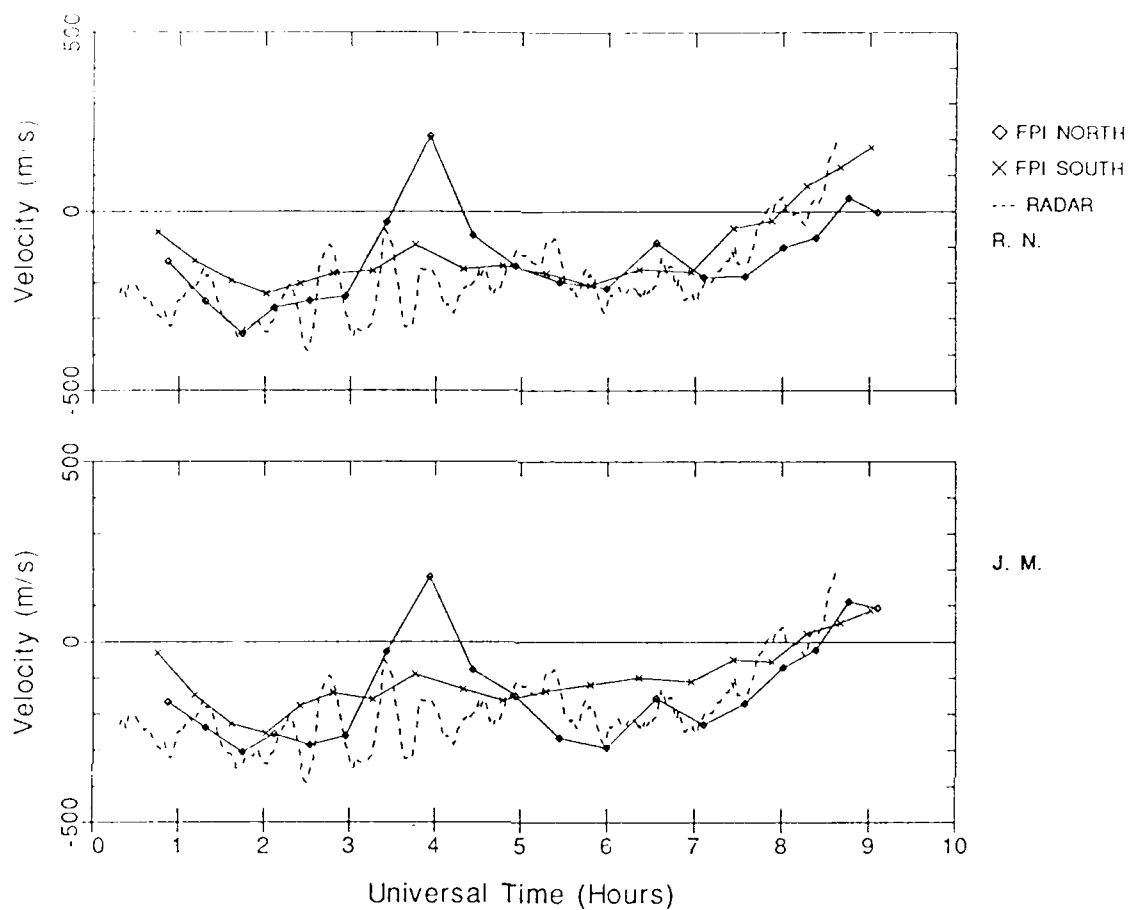


Figure 3.5. Plot of two independent reductions of the data for 4 March 1987 showing differences in observed gradients. After 05 UT the differences reach 100 m/s. The altitude of the radar data is 228 km at  $f = 3.4$ .

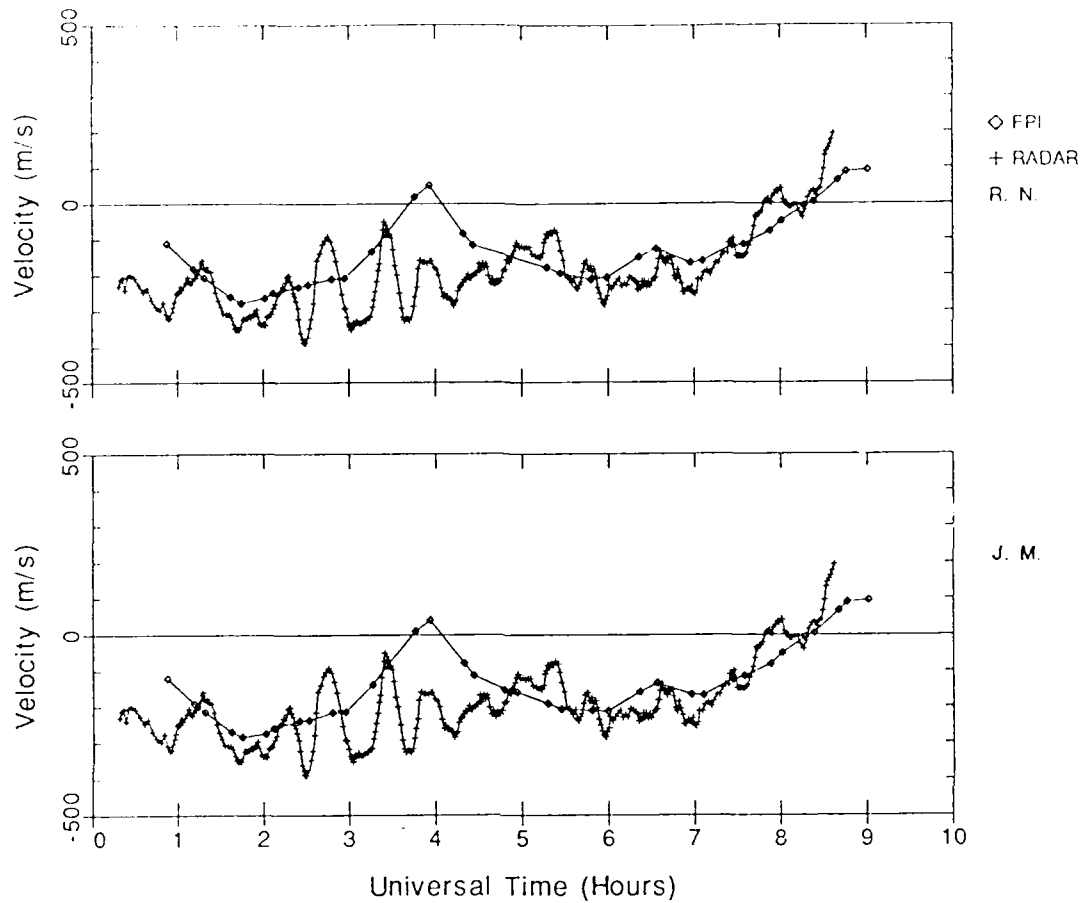


Figure 3.6. Plot of resolved N-S FPI data for 4 March 1987 showing little difference between the two reductions. Despite the large differences in the line-of-sight velocities from the two reductions, the resolved velocities are nearly identical in this example. The altitude of the radar data is 228 km and  $f = 3.4$ .

m/s. This affects the ISR-FPI comparisons. In Figure 3.6 the differences are not as great. Clearly, the way in which the FPI data is reduced is extremely important in a comparison of this sort.

### 3.2.2. FPI Interpolation

Once the data are corrected for the zero offset it is ready for interpolation. This is done by the *FPIRED* program. Because the data in the magnetic north and south directions are at different times, interpolation of the LOS's to a common time is performed to resolve the vector. The interpolation is a linear interpolation of the north and south LOS velocities to each other's time. This is done for our geomagnetic data from 1983, 1984 and 1987. Therefore, for each input time two velocities are generated, one north and one south. This is done via the following equations:

$$V(t) = \left( \frac{t - t_1}{t_2 - t_1} \right) (V_2 - V_1) + V_1 \quad (3.2.4)$$

and

$$\sigma^2 = \left( \frac{t - t_1}{t_2 - t_1} \right)^2 \sigma_2^2 + \left[ \left( \frac{t - t_1}{t_2 - t_1} \right) - 1 \right]^2 \sigma_1^2 \quad (3.2.5)$$

[Bevington, 1969] where  $t$  is the time,  $V$  the LOS wind and  $\sigma$  the error on the wind. It is important to note that as a result of the averaging involved the data are smoothed. Also, the first and last data records in each day's data are lost because it takes two like points in each direction to do the interpolation. Otherwise a more complicated interpolation is required.

A four-point interpolation is performed for observations in the geographic N, E, S and W. A linear interpolation of the form (3.2.4) and (3.2.5) is performed at each position. Therefore, for each FPI observation, four LOS velocities are generated (see Figure 3.7). These four velocities are then used to derive the neutral wind *vector* velocity. This vector velocity is in geographic coordinates and the horizontal components are transformed into geomagnetic coordinates for the radar comparison.

### 3.2.3. Earth's Curvature Correction

Many FPI calculations neglect the curvature of the Earth and assume it to be "flat". We take the curvature into account in our WNDVEC program to better calculate the range to the observation point and better resolve the vector. This

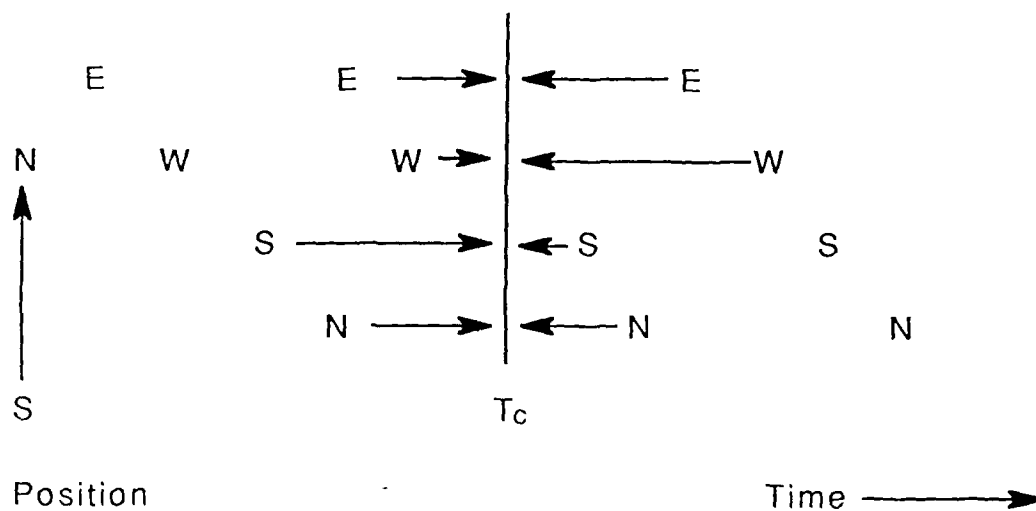


Figure 3.7. Example of a possible arrangement of FPI scan positions in time.  $T_c$  is the common time to which the FPI data will be interpolated. Arrows indicate which points are involved in the interpolation.

program was adapted from one developed by Dr. V. Wickwar while at SRI. The situation is illustrated in Figure 3.8. From the data, we know the elevation angle of the observation ( $\alpha$ ). The angle between the Earth's radius vector and the FPI elevation vector is given by

$$\gamma = 90 + \alpha. \quad (3.2.6)$$

Armed with this information and the law of cosines, we can calculate the distance from the center of the Earth to the observation point,  $R$ , as:

$$R^2 = R_e^2 + (D)^2 - 2R_e(D)\cos(\gamma) \quad (3.2.7)$$

where  $R_e$  is the radius of the Earth,  $D$  is the range from the FPI to the observation point,  $H$  is the altitude above the Earth's surface and  $R = R_e + H$ . Simplifying, the law of cosines expressions (3.2.7), we obtain

$$(D)^2 - 2[R_e \cos(\gamma)](D) + R_e^2 - (R_e + H)^2 = 0 \quad (3.2.8)$$

or

$$(D)^2 - 2[R_e \cos(\gamma)](D) - [2R_e H + H^2] = 0. \quad (3.2.9)$$

Applying the quadratic formula to solve for the range we obtain the following expression

$$D = \frac{-b + \sqrt{b^2 - 4c}}{2} \quad (3.2.10)$$

where  $a = 1$ ,  $b = -2R_e \cos(\gamma)$  and  $c = -2R_e H - H^2$ . We have chosen the positive root because  $-b < \sqrt{b^2 - 4c}$ .

Additionally, the azimuth may be different at the observation point than at the instrument location as shown in Figure 3.9. For this reason, once the range is known a new azimuth angle is calculated at the point of observation.

The effect of these corrections is to reduce the error associated with the Earth's curvature. While the correction is small at the 45° zenith angle, these corrections become much bigger at 70 and 80 degree zenith angles (20° and 30° elevation angles). Although most of the FPI data are for 45° elevation angles, the routine has been made general so it can be used at any zenith angle. See Table 2 for comparison of data with and without corrections.

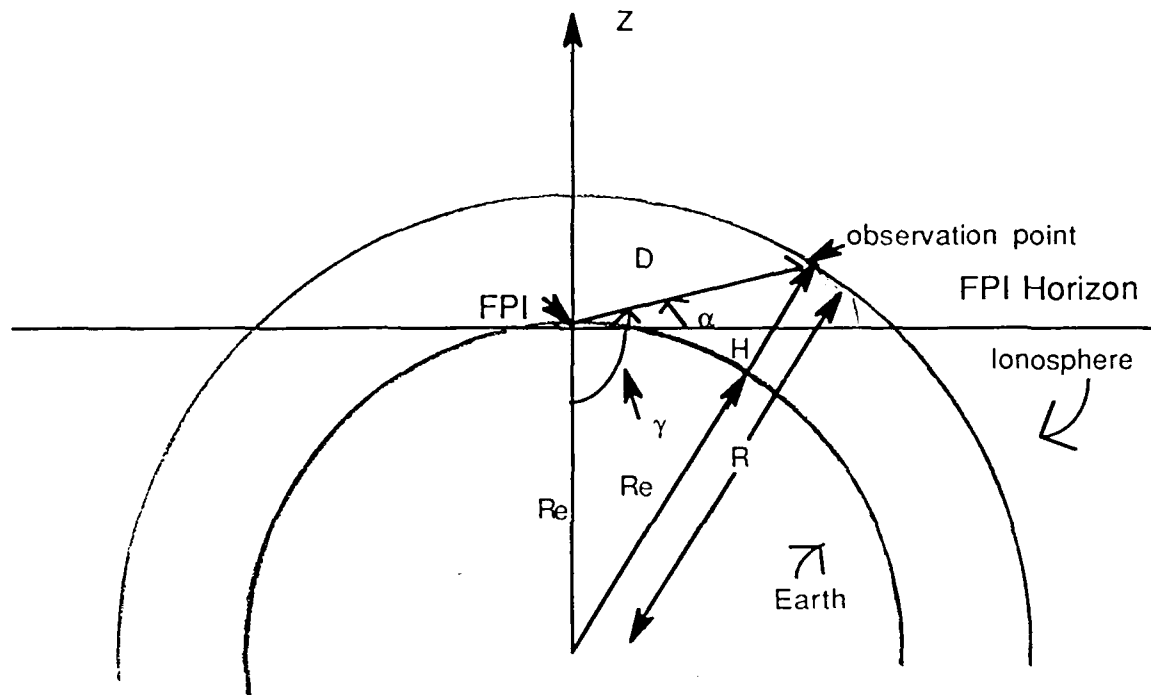


Figure 3.8. Geometry used to calculate the range from the FPI to the observation point.

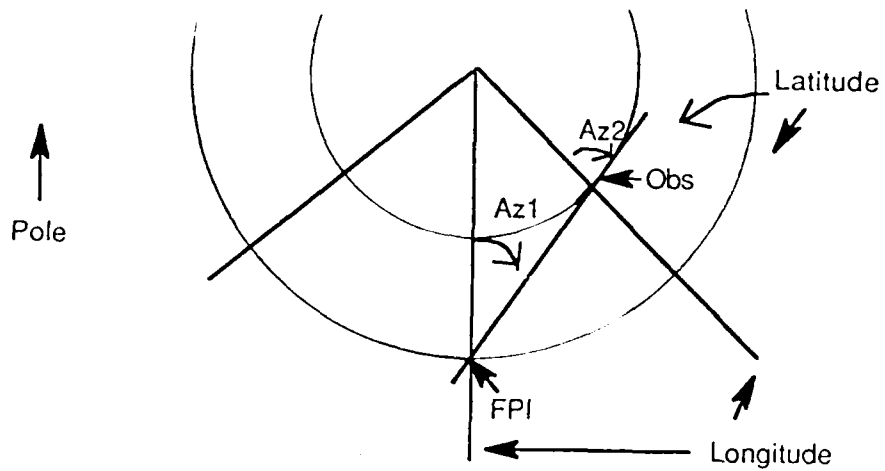


Figure 3.9. Geometry associated with the azimuth correction necessary due to a spherical Earth. Effect is exaggerated. Clearly,  $Az_1 \neq Az_2$ .

Table 2. Comparison of Flat Earth Versus Curved Earth Correction in the Resolved Fabry-Perot Interferometer Data.

Earth's Curvature Correction				
Elevation Angle	Height (km)	Flat Earth Range (km)	Curved Earth Range (km)	Difference km
10	220	1267.0	912.0	355.0
20	220	643.0	578.0	65.0
30	220	440.0	420.0	20.0
40	220	342.0	335.0	7.0
45	220	311.0	306.0	5.0
50	220	287.0	284.0	3.0
60	220	255.0	253.0	2.0
70	220	234.0	234.0	0.0
80	220	223.0	223.0	0.0
90	220	220.0	220.0	0.0

### 3.2.4. Resolving the Vector Neutral Wind

The simplest way to resolve the FPI data is to assume a flat Earth and no vertical wind. Then the horizontal wind giving rise to the LOS observation is

$$U_H = \frac{V_{LOS}}{\cos(\alpha)} \quad (3.2.11)$$

where  $\alpha$  is the elevation angle. Specifically, when  $V_{LOS}$  is toward the magnetic north

$$U_N = \frac{V_{LOS}}{\cos(\alpha)}. \quad (3.2.12)$$

When  $V_{LOS}$  is toward magnetic south

$$U_N = -\frac{V_{LOS}}{\cos(\alpha)}. \quad (3.2.13)$$

By interpolating the northward observations to the times of the southward observations and vice versa, as just described, the two FPI northward components could be averaged to find a better value of  $U_N$ . Or they could be subtracted to find a north-south gradient in the meridional neutral wind. In averaging them, any error in the zero correction would cancel. In finding the gradient, any error in the zero correction would be doubled.

While this procedure is particularly easy, it is not always clear that there is no vertical wind and it leaves out the corrections needed for a curved Earth. Therefore, we also used another procedure.

Once the interpolation is done and the azimuth and elevation have been corrected for the Earth's curvature, the horizontal neutral wind vector can be calculated. The geometry for this calculation is shown in Figure 3.10. The vector  $\ell$  is the position vector (of unit length) to the observation point as defined by the range, azimuth and elevation obtained from the FPI measurements. From the geometry we see that

$$\ell_x = \sin(\text{az}) \cos(\text{el}) \quad (3.2.14)$$

$$\ell_y = \cos(\text{az}) \cos(\text{el}) \quad (3.2.15)$$

$$\ell_z = \sin(\text{el}) \quad (3.2.16)$$

where  $\ell_H$  is the position vector projected on the  $x$ - $y$  plane. If, for example, we use

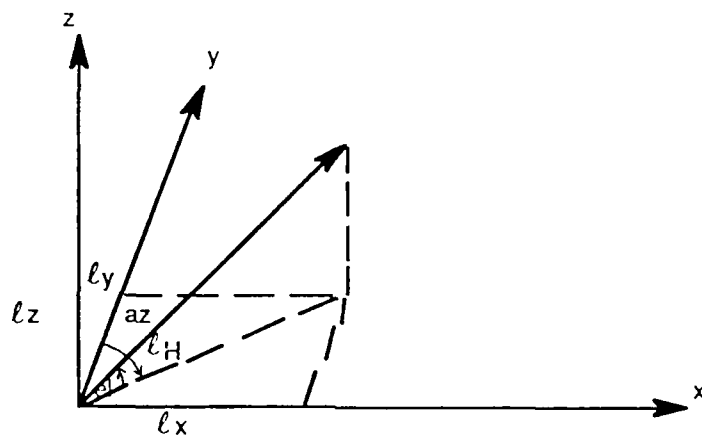


Figure 3.10. Geometry used to resolve the vector neutral wind.  $x$  is positive to east,  $y$  to north, and  $z$  up.

three points to resolve our vector then

$$\mathbf{V}_{LOS1} = \ell_1 \cdot \mathbf{U} \quad (3.2.17)$$

$$\mathbf{V}_{LOS2} = \ell_2 \cdot \mathbf{U} \quad (3.2.18)$$

$$\mathbf{V}_{LOS3} = \ell_3 \cdot \mathbf{U} \quad (3.2.19)$$

where  $\mathbf{U}$  is the neutral wind vector,  $\ell_i$  are the unit vectors along the line-of-sight and  $\mathbf{V}_{LOS_i}$  the line-of-sight velocities. Here we assume  $\mathbf{U}$  is spatially uniform. Another way of writing equations (3.2.17) thru (3.2.19) is in matrix form

$$\begin{bmatrix} V_{LOS 1} \\ V_{LOS 2} \\ V_{LOS 3} \end{bmatrix} = \begin{bmatrix} \ell_{x 1} & \ell_{y 1} & \ell_{z 1} \\ \ell_{x 2} & \ell_{y 2} & \ell_{z 2} \\ \ell_{x 3} & \ell_{y 3} & \ell_{z 3} \end{bmatrix} \cdot \begin{bmatrix} u_x \\ u_y \\ u_z \end{bmatrix} \quad (3.2.20)$$

or

$$\mathbf{V}_{LOS} = \mathbf{A} \cdot \mathbf{U}. \quad (3.2.21)$$

Clearly, we know the values for terms  $\mathbf{V}_{LOS_i}$  and  $\mathbf{A}$  in (3.2.21) and can solve (3.2.21) for  $\mathbf{U}$  using matrix algebra where

$$\mathbf{A}^{-1} \mathbf{V}_{LOS} = \mathbf{A}^{-1} \mathbf{A} \mathbf{U} = \mathbf{U}, \quad (3.2.22)$$

using the inverse matrix  $\mathbf{A}^{-1}$ . This is how the calculation is made. With the use of equation (3.2.14) to (3.2.16) and (3.2.22) we can write equation (3.2.22) as

$$\begin{bmatrix} u_x \\ u_y \\ u_z \end{bmatrix} = \left| \mathbf{A}^{-1} \right| \cdot \begin{bmatrix} V_{LOS 1} \\ V_{LOS 2} \\ V_{LOS 3} \end{bmatrix}. \quad (3.2.23)$$

Once (3.2.23) is solved, we have the necessary vector neutral wind to compare with the radar data. In a similar fashion we can derive the covariance matrix from the *LOS* variances

$$\begin{bmatrix} \sigma_{xx}^2 & \sigma_{xy}^2 & \sigma_{xz}^2 \\ \sigma_{yx}^2 & \sigma_{yy}^2 & \sigma_{yz}^2 \\ \sigma_{zx}^2 & \sigma_{zy}^2 & \sigma_{zz}^2 \end{bmatrix} = \left| \mathbf{A}^{-1} \right| \cdot \begin{bmatrix} \sigma_{LOS1}^2 & 0 & 0 \\ 0 & \sigma_{LOS2}^2 & 0 \\ 0 & 0 & \sigma_{LOS3}^2 \end{bmatrix} \left| \mathbf{A}^{-1} \right|^T. \quad (3.2.24)$$

The uncertainties for  $U_x$ ,  $U_y$  and  $U_z$  are given by  $\sqrt{\sigma_{xx}^2}$ ,  $\sqrt{\sigma_{yy}^2}$  and  $\sqrt{\sigma_{zz}^2}$ , respectively.

The above discussion illustrates the case for three line-of-sight observations. This is the minimum number needed to derive a vector. However, two line-of-sights in the same plane (e.g., toward the magnetic north and south) can be used to derive the horizontal and vertical components in that plane. The procedure is a two-dimensional version of the three-dimensional procedure just presented. If four (or more) line-of-sight velocities are available, the above procedure can be developed into a least squares fit to derive the vector neutral wind.

As already discussed, most of our data (between 1983 and 1987) had two line-of-sight observations in the magnetic meridian. The 1988 data had four line-of-sights in the geographic cardinal directions.

### 3.2.5. *Altitude*

As discussed in Chapter I, there are several sources of the OI 6300-Å optical emission. The most important at high latitudes are particle excitation and dissociative recombination (equation 2.2) [Meier *et al.*, 1989]. These two sources are assumed to contribute the most to the emission at Sondrestrom.

To find the best altitude for comparison between the two instruments, we calculated the peak dissociative recombination altitude for this data set. Figure 3.11 shows a plot of the peak *F*-region electron density and peak dissociative recombination altitudes for a day with little evidence of energetic auroral precipitation, i.e., without a strong auroral *E*-region. The emission peak is approximately 50 km below the *F*-region peak and its average value on this night is between 230 and 280 km. These were obtained using the ISR-measured electron density profiles. The neutral atmospheric parameters came from MSIS-86 which were calculated at the electron density altitudes. The equations for the dissociative recombination calculation were obtained from Wickwar *et al.* [1974] while the coefficients came from Sharp [1983]. The altitude of the radar gates are shown in Figure 3.11 as the three horizontal lines at 180, 230 and 280 km.

The emission altitudes for particle precipitation have been calculated by Rees and Roble [1986] and Meier *et al.* [1989]. They are summarized along with the dissociative recombination results in Figure 3.12. The vertical bars show the altitude range where the emission is at or above 75% of the maximum value. They are shown for soft particle precipitation (100 eV for Rees and Roble; 250 eV for Meier *et al.*) where the electrons stop in the *F*-region, and for diffuse auroral precipitation (2 keV for both groups) where the electrons penetrate to the *E*-region. The two

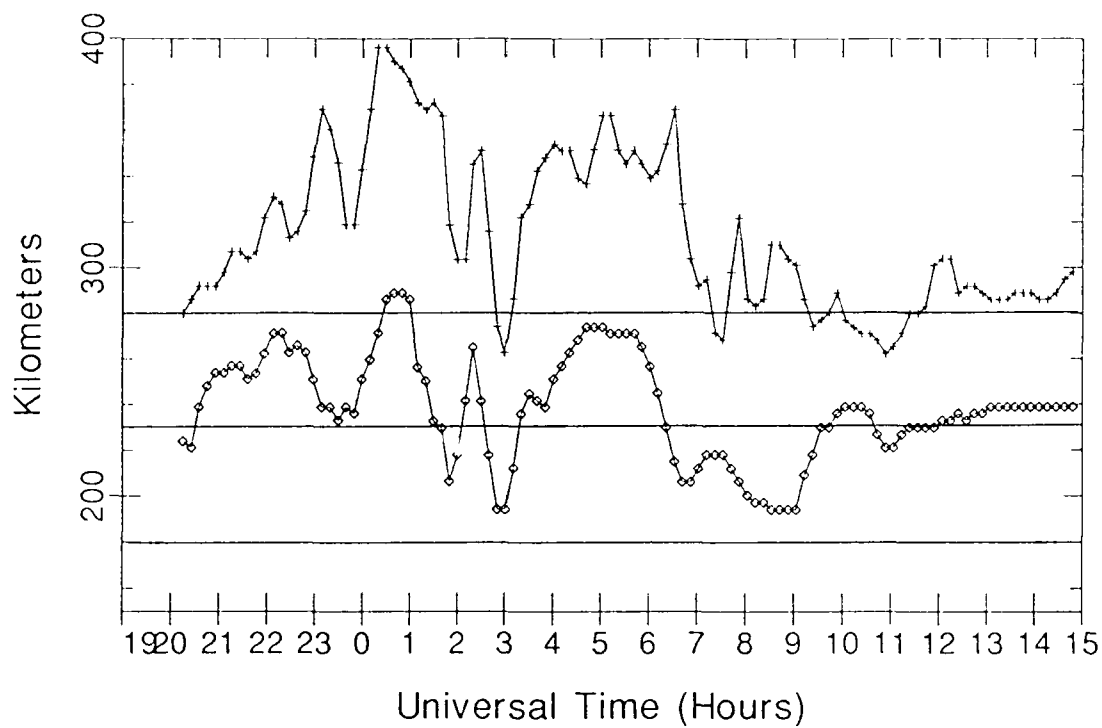


Figure 3.11. Plots of the peak electron density altitude and peak dissociative recombination altitude for 16-17 March 1988. The three horizontal lines correspond to the altitudes at which the radar makes its measurements.

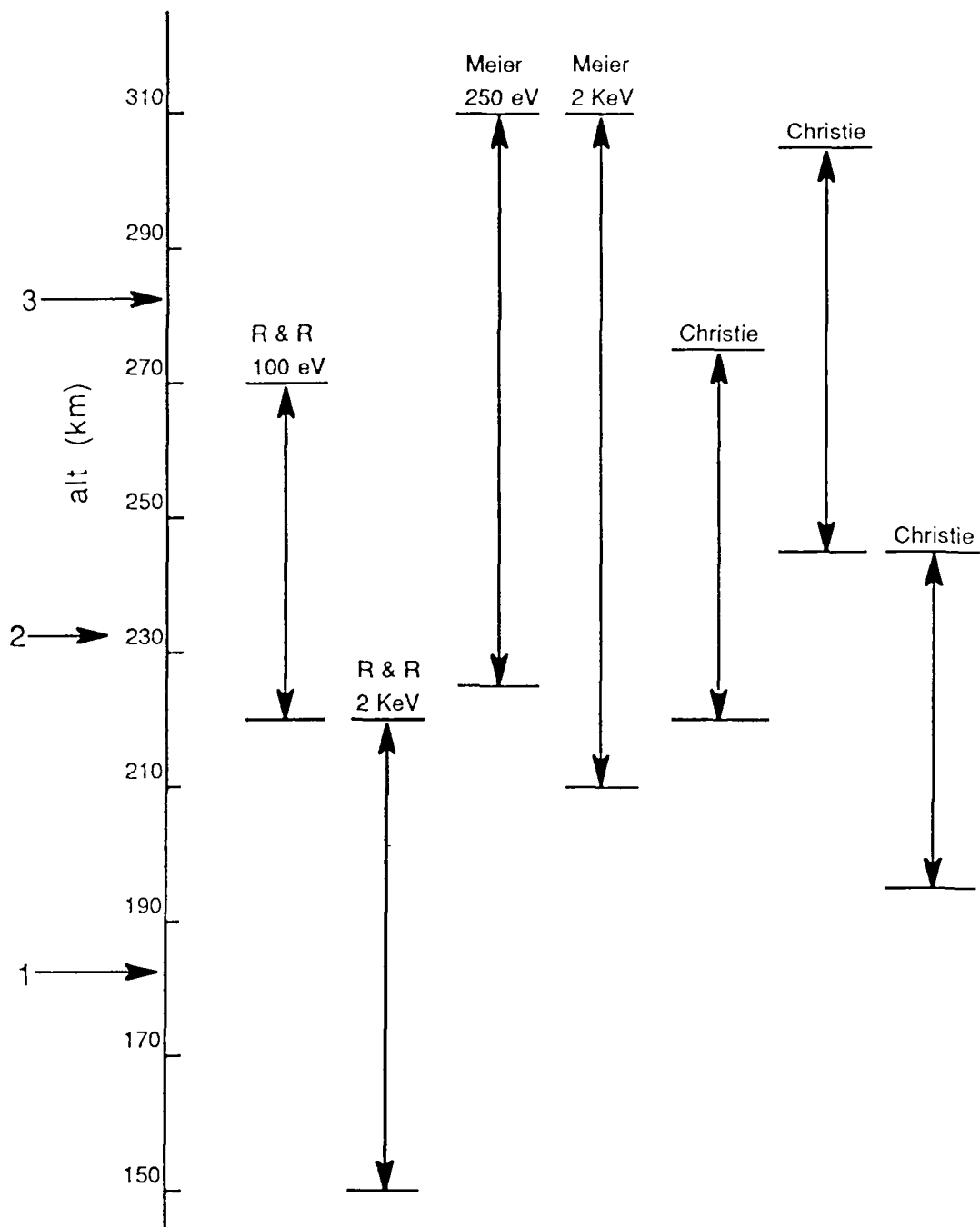


Figure 3.12. Plot summarizing the emission altitudes for particle precipitation and dissociative recombination. R and R refer to *Rees and Roble* [1986]; Meier refers to *Meier et al.* [1989] and Christie refers to this study.

calculations differ considerably from one another. Taken together, they show a possible range between 150 km and 310 km for significant emission, with the peak emission rates between 180 and 270 km. This is the same altitude range as the three radar gates used in this study.

The results of the FPI-ISR comparisons presented in Chapter V strongly suggest that an average altitude near 230 km is most likely for these emissions.

## CHAPTER IV

## THE DATA

We began this comparison with a list of 50 nights in which overlapping FPI and ISR data had been acquired. Days with less than four hours of overlap, cloudy skies (see below) or poor data, were not used. This left us with eleven days of data we could compare as shown in Table 3. In Table 3, it is apparent that the magnetic activity for this data set was generally low to moderate. Also, because of the dark sky requirement of the FPI and the high latitude location, the data are from the September to March time frame. There are no data from 1985 or 1986 primarily due to problems with the FPI instrument.

The radar data were supplied by two sources. NCAR supplied the world days and SRI International supplied the others. The radar data came on magnetic tape in NCAR format. These tapes consisted of the radar-measured geophysical parameters:  $N_e$ ,  $T_e$ ,  $T_i$  and  $V_i$ . These parameters were the inputs to MERWIND as previously discussed. Additional inputs to MERWIND were the 81-day average  $F_{10.7}$  flux, that day's  $A_p$  and the previous day's  $F_{10.7}$  flux. These additional inputs were required by MSIS-86 to calculate the neutral atmospheric parameters needed by MERWIND. MERWIND was then run with several values of  $f$  and compared with the FPI data.

The FPI data were supplied by several sources. The primary supplier was Dr. J. W. Meriwether of GL, who established the FPI at Sondrestrom and ran it for many years. The other supplier was Dr. Rick Niciejewski of the University of Michigan, either directly or through the CEDAR database.

Initially, it appeared that we would have to perform the zero velocity correction on the FPI data as discussed in the previous chapter. However, the data arrived with that correction already made. That is to say, we were supplied with the corrected line-of-sight velocities. In addition, for the data prior to 1988, we were provided with cloud cover data by Rick Niciejewski of the University of Michigan, which was obtained by Sondrestrom meteorologists. For the 1988 data, the cloud cover information was included in the CEDAR database catalog.

Table 3. Data from the Radar and FPI Compared in this Study. Values of  $Kp$  are Given for Each 3 Hour Period Beginning with the 21-0 UT Value on Line 1 of Each Day. Note: PSN Means Position, e.g., 5-PSN Means 5-Position Scan.

## DATA SET

Date	Time (UT)		$\langle F_{10.7} \rangle$	Prev. $F_{10.7}$	$A_p$	$Kp$	Mode	
	Radar	FPI					Radar	FPI
13-14 Sep 83	13/2246 14/2254	13/2314 14/0727	118.05 117.46	104.9 104.4	7 6	2+ 2,1+,2	World Day	8-PSN Scan
08-09 Oct 83	08/2357 09/0604	08/2317 09/0850	107.9 107.6	133.9 131.1	16 5	2+ 3-,2-,1	World Day	8-PSN Scan
06-07 Nov 83	07/0046 07/0535	06/1928 07/1100	101.25 100.9	105.1 105.1	3 12	0+ 0+,1+,3-	Up B	4-PSN Scan
23-24 Feb 84	23/0200 24/0220	23/2128 24/0956	125.57 128.95	158.0 166.1	15 10	2 3-,2-,2	World Day	8-PSN Scan
28-29 Jan 87	28/0000 29/0000	28/2000 29/1117	70.44 70.44	69.9 70.8	11 10	3+ 5-,3+,2	World Day (GITCAD)	4-PSN Scan
25-26 Feb 87	26/0055 26/0830	25/2142 26/0937	71.9 72.2	72.1 73.5	7 6	1 1+,0+,1	Up B	4-PSN Scan
26-27 Feb 87	27/0039 27/0444	26/2141 27/0933	72.2 72.5	73.5 73.9	6 12	1 1,2-,3-	Up B	4-PSN Scan
04 Mar 87	04/0013 04/0843	03/2200 04/0911	73.9 74.3	73.3 71.6	6 10	2 4-,2,1+	Up B	4-PSN Scan
16-17 Mar 88	16/1237 17/2359	16/2254 17/0807	114.5 114.52	112.6 114.1	14 9	2 3-,3,2+	World Day	5-PSN Scan
17-18 Mar 88	17/2200 18/2359	17/2259 18/0803	114.52 114.5	114.1 117.4	9 7	2- 2+,2-,2+	World Day	5-PSN Scan
18-19 Mar 88	18/2300 19/2359	18/2303 19/0806	114.5 114.46	117.4 116.1	7 4	2- 1,2-,2-	World Day	5-PSN Scan

We handled the data in several ways. First, we restricted the data to periods when the cloud cover was less than 3 on a scale where 0 is clear and 8 is overcast. This has been determined, by previous work, to be the threshold where clouds begin to affect the data [Meriwether, private communication, 1990; Niciejewski, private communication, 1990]. For the data prior to 1988, we projected the data obtained in the magnetic north and south direction onto the horizontal. Then a two-point interpolation was done using program FPIRED. We then ran program WNDVEC to resolve the horizontal meridional and vertical winds. For the 1988 data, we used a four-point interpolation in program FPIRED and ran WNDVEC to resolve the wind vector and determine the horizontal meridional wind. The data from this study are presented in the Appendix at the best  $f$ -factor.

## CHAPTER V

## DISCUSSION

Once the data are reduced as discussed in Chapter III, then it can be plotted and compared. Starting from a list of over 50 nights, we obtained 11 good nights of data (as shown in Chapter IV) with sufficient overlap for the comparison. In order to facilitate the comparison, all the radar data were smoothed using a running average whose period was either 10 minutes (10 points) or 1.5 hours (3 points) based on the number of data points available. From looking at all the data, generally speaking, the ISR-derived and the FPI-measured horizontal neutral wind in the magnetic north-south direction basically agree. There are several categories of data that become apparent with any particular day often falling into either one or more than one group. By analyzing these broad classes of data, we can learn something about how the horizontal meridional neutral winds at high latitudes vary with altitude, measurement technique, neutral density, solar-cycle, time and latitude.

We begin with altitude. As discussed earlier, the radar technique allows the horizontal meridional wind to be deduced at various altitudes. For this research, the wind was deduced for three altitudes corresponding to roughly 180, 230 and 280 kilometers. The altitudes varied slightly from night to night, but remained near these levels. The data show variability with altitude, particularly between 180 and 230 km. A basic pattern can be seen in which the wind generally becomes more equatorward with increasing altitude. There also appears to be a small phase shift. This phase shift can be seen on nine of the eleven nights and is usually negative (i.e., earlier at higher altitudes), particularly between 180 and 230 km. This shift is on the order of less than 30 minutes. The phase shift is not unexpected between these altitudes. It is damped out at higher altitudes because of viscosity.

Figure 5.1 shows how changing the  $f$ -factor at low altitudes has little effect on the radar-derived horizontal wind for the night of 23-24 February 1984. The plot is for 181 km. The reason for the small change is because the contribution to the wind from diffusion is very small at 181 km and the  $f$ -factor enters the calculation in the diffusion coefficient. Therefore, we have little control over the agreement at the lower radar gate (180 km).

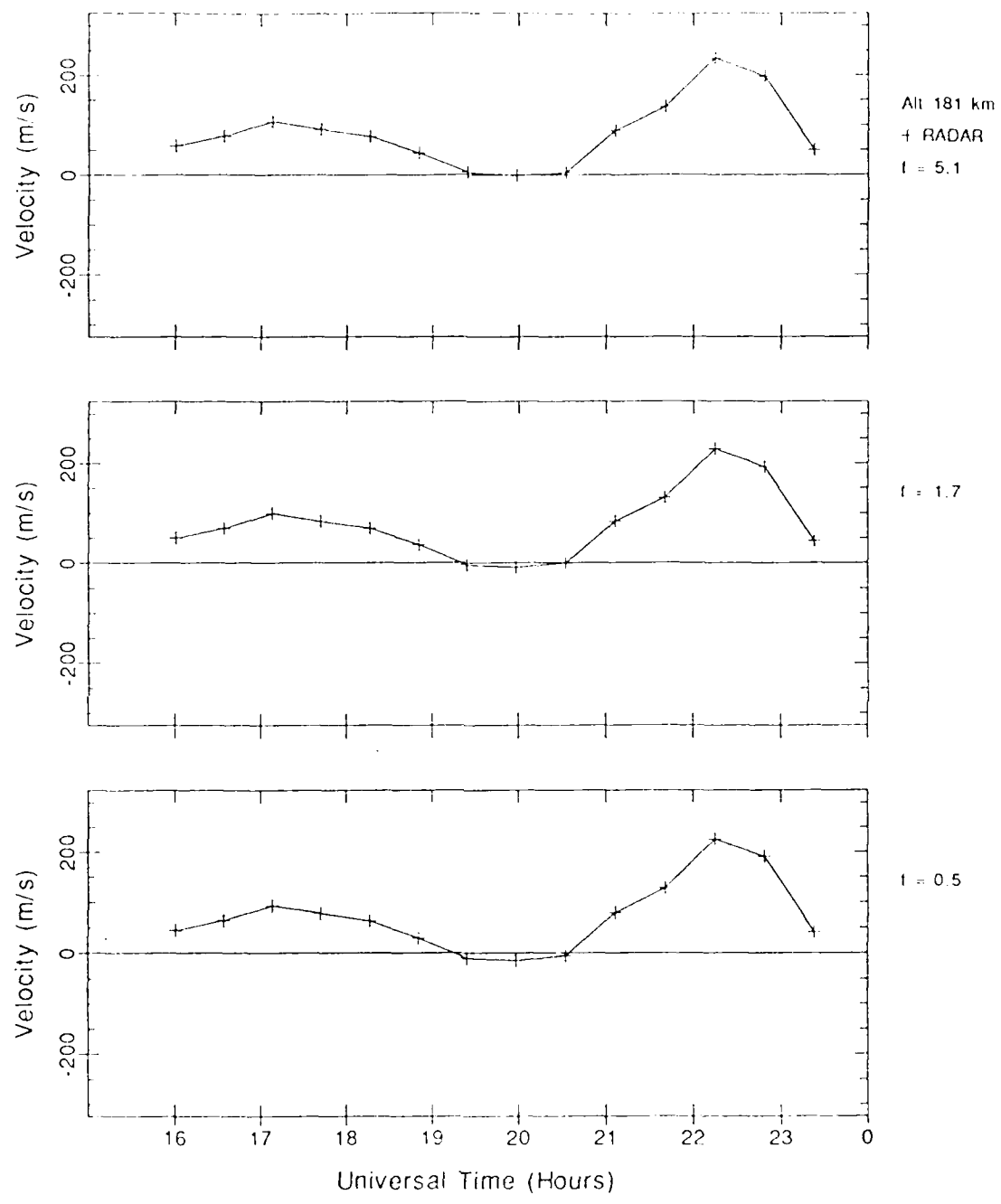


Figure 5.1. Data from 23-24 February 1984 showing how changing  $f$  at lower altitudes has little effect on the winds.

Figure 5.2 shows a scatter plot for the value of  $f$  deduced at the middle altitude (230 km) plotted on the  $x$ -axis while the value of  $f$  deduced at the highest altitude (280 km) is plotted on the  $y$ -axis. The diagonal line is for  $y = x$ . It is evident from Figure 5.2 that a higher  $f$  was needed to bring the FPI and ISR data into agreement at the higher altitude. In order to minimize  $f$ , and for the reasons outlined above and in Chapter III, we chose to do the comparison at 230 km. This is as expected because the peak of the OI 6300-Å emission generally occurs above 170 km but below 280 km (see Figure 3.12) [Rees and Roble, 1986; Sica et al., 1986; Meier et al. 1989].

In comparing the two sets of winds, several things of a general nature regarding the two measurement techniques stand out. The overall shape is primarily the same. Specifically, the shape of the radar data is similar in the middle and high altitudes. This is not necessarily the case at the lowest radar altitude. Therefore, the comparison of the two data sets supports an average emission height well above the lowest radar gate at  $\sim 180$  km.

The radar-derived winds show much more variation than the FPI-measured winds. Figure 5.3 shows an extreme example of this for 4 March 1987. The radar shows a remarkable wavelike pattern, particularly between 02 and 04 UT, while the FPI measurements are much smoother. This difference in behavior involves several factors. The radar time resolution is one minute (with 10 minute smoothing), while the FPI time resolution is closer to 45 minutes. The optical emission, whether from dissociative recombination or particle precipitation, may originate from as much as a 100-kilometer altitude region whereas the radar observations originate from approximately a 50-kilometer altitude region. Some of these variations appear to originate from vertical motion to which to ISR at an  $80^\circ$  elevation angle is much more sensitive than the FPI at a  $45^\circ$  elevation angle. To make the two data sets more comparable, the radar data were smoothed. Also, the error bars on the radar are significantly less than the oscillations. The comparison then emphasizes trends in both data sets that can be analyzed.

The trends between these two instruments have been compared. The winds were plotted at an altitude of primarily 230 km. The FPI winds were plotted directly from the resolved horizontal vector velocity. The radar winds were plotted with varying values of  $f$  ranging from 0.5 to 5.1. This factor, as previously discussed, acts to change the product of the  $O^+$ -O collision cross section and the atomic oxygen density. This is the same factor examined by Burnside et al. [1987]. They found the

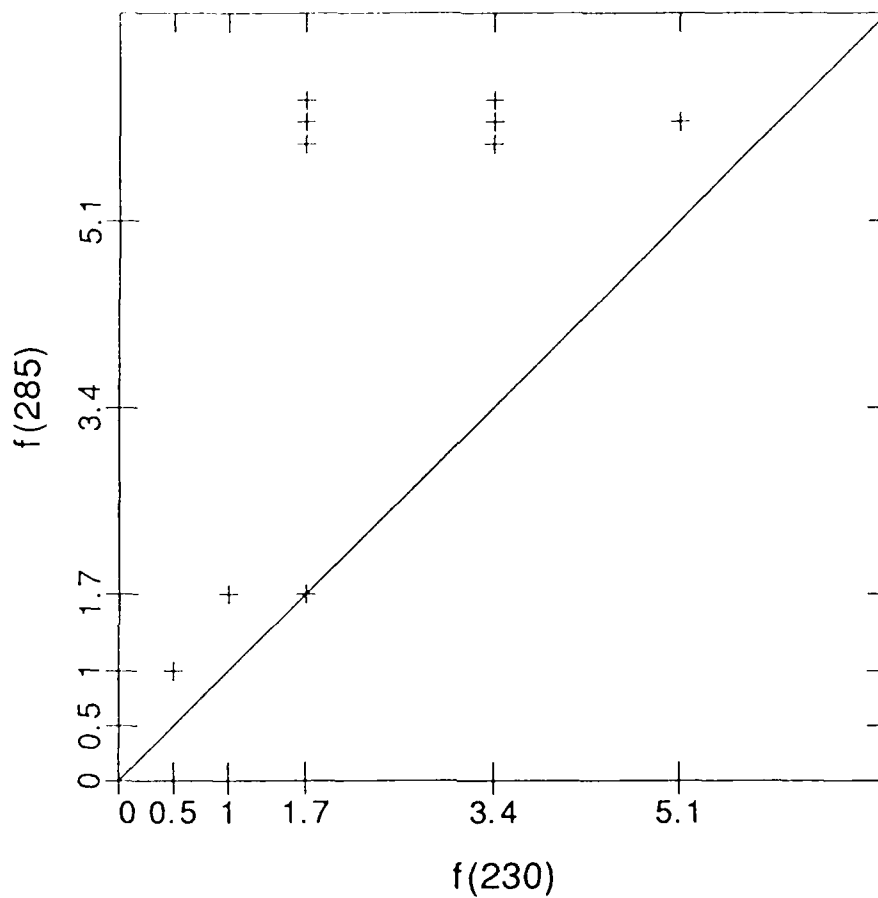


Figure 5.2. Scatter plot of the values of  $f$  needed at 230 km ( $x$ -axis) versus that needed at 280 km ( $y$ -axis). The higher altitude generally required a higher value of  $f$ . The diagonal line is the line where  $x = y$ .

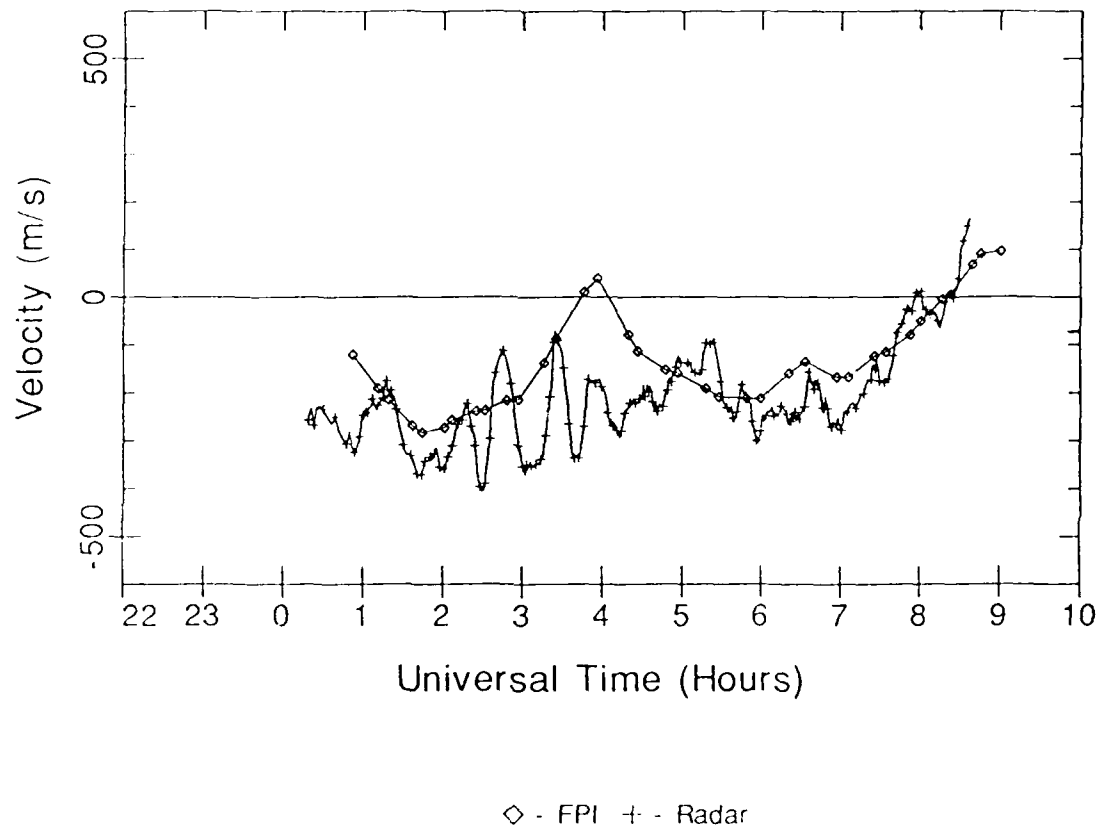


Figure 5.3. Plot of radar data and FPI data from 4 March 1987 emphasizing the variability seen in the radar but not in the FPI. The altitude is 228 km. The radar data are smoothed using a running average of over 10 minutes. For clarity only every third radar point is plotted with a symbol.

best agreement between the two techniques was a factor of 1.7. Because the days they examined came from a variety of conditions, they concluded that, on average, the MSIS densities were correct. Therefore, they concluded it was the collision cross section that needed to be increased.

In the high latitude region of this study, the atmosphere is more variable and the MSIS model is not as good in the sense that there appears to be less data to define it [Hedin *et al.*, 1977; Hedin, 1983, 1987]. For instance most of the low solar activity data from these high latitudes came from the short-lived AE-D satellite [Hedin, private communication, 1990]. We will, therefore, perform a much cruder comparison than that of Burnside *et al.* Figure 5.4 shows a graph of the comparisons. The number of nights requiring a particular factor are presented on the *y*-axis while the various factors are shown on the *x*-axis. The factors 0.5, 1.0, 1.7, 3.4, and 5.1 were used for the radar winds. "The best" factors were determined by comparing the overall match of the radar with the FPI for the period of overlap. This was done by counting the number of radar points within one standard deviation of the FPI. The factor with the most number of points meeting that criteria was deemed the best fit. The most common values are factors of 1.7 and 3.4. The average, including only those values between 1.0 and 5.1, is 2.57. This large value is consistent with that determined by Burnside *et al.* in that it is larger than 1.0.

We do not have enough comparisons under a wide variety of conditions to attempt to separate the cross section and atomic oxygen density affects. But, if we accept Burnside *et al.*'s value of 1.7 for the cross section, then our results provide information about the high-latitude atomic oxygen in the MSIS-86 model. They suggest that the MSIS model underestimates the atomic oxygen density by a factor of 1.5, on average, in the polar cap.

Other differences emerge from the comparison of the two techniques. We will now look at some of those in more detail. We have organized this portion according to time-scale. We will discuss the longer time-scale phenomena first and work down to the shorter duration events. This by no means indicates the relative importance of the processes involved.

There appears to be a solar activity or solar-cycle dependence in the comparisons. In general, the data from 1983, 1984 and 1988 ( $F_{10.7} \gtrsim 100$ ) show agreement for a lower factor than do the data for 1987 ( $F_{10.7} \sim 70$ ). Figure 5.5 and 5.6 illustrate this. Figure 5.5 shows a graph of the 1983, 1984 and 1988 data while Figure 5.6 shows a graph of the 1987 data. The *x*-axis is the factor used to obtain the best

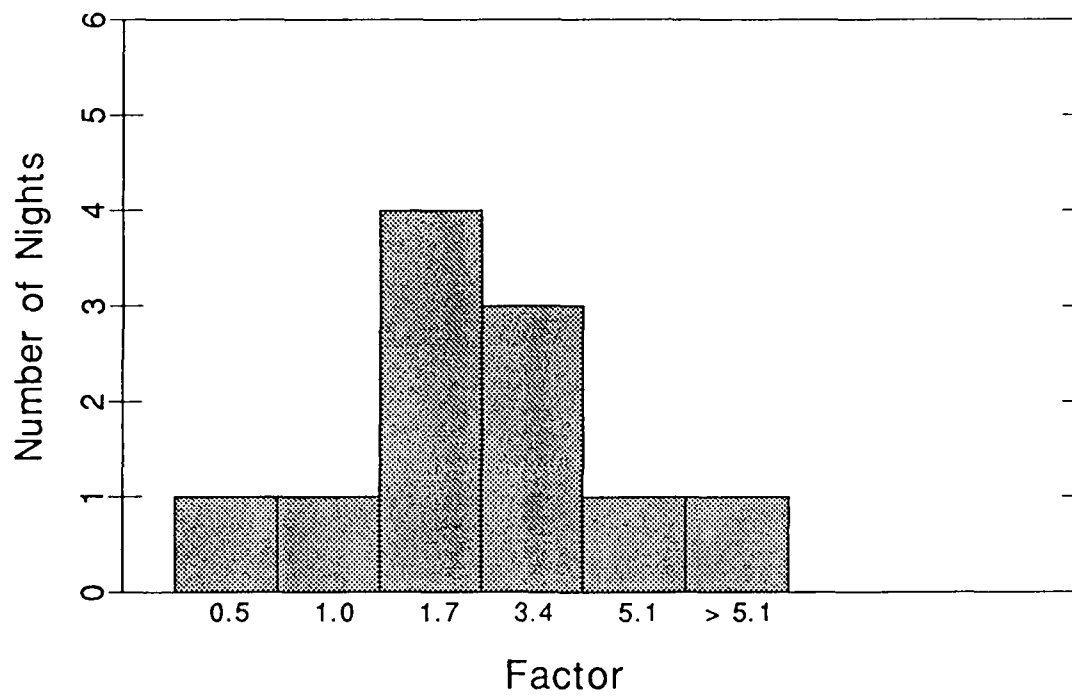


Figure 5.4. Graph showing the range of factors needed to achieve the best agreement between the radar and FPI.

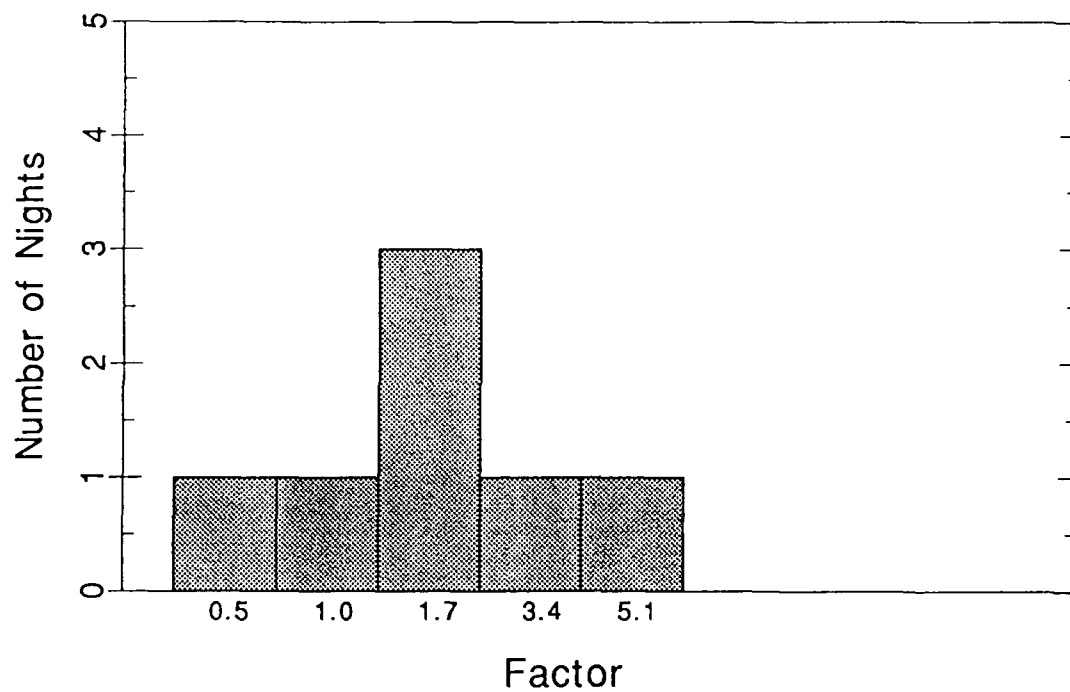


Figure 5.5. Graph of factors needed to achieve the best agreement between the radar and FPI for 1983, 1984 and 1988 for medium solar activity.

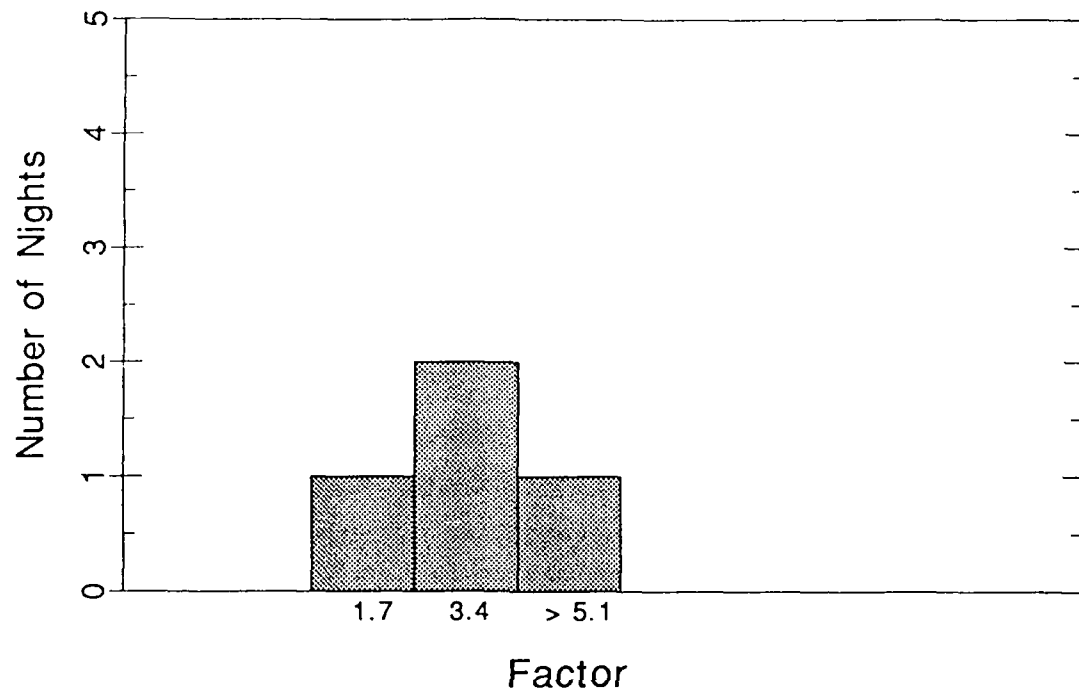


Figure 5.6. Graph showing the factors needed to achieve the best agreement between the radar and FPI for 1987, close to solar-cycle minimum.

agreement while the  $y$ -axis is the number of nights requiring a particular factor. The data from 1987 are very close to solar-cycle minimum whereas the other data are for much higher solar activity. Figure 5.7 shows plots of the 81-day average  $F_{10.7}$  cm flux for the data from the four years in question. Here the  $x$ -axis is the day number and the  $y$ -axis the flux. Clearly, the 1987  $F_{10.7}$  cm flux is well below that of the other three years. In the "high-activity" set the most frequent value, and the center of the distribution, is 1.7 whereas in the "low-activity" set it is 3.4.

The mix of magnetic activity is similar during these two periods, as shown in Figure 5.8. Figure 5.8 is a plot of the  $K_p$  values during the period of overlap ( $x$ -axis) and the frequency of occurrence of that  $K_p$  ( $y$ -axis). On average, the  $K_p$  for this data set was below 3.0. Therefore, the different behavior appears to be related to solar activity, not geomagnetic activity.

Because the cross section has to be constant in time, it appears that the solar-cycle variation of the thermospheric atomic oxygen is not being correctly modelled by MSIS-86. While it appears to be approximately correct in the "high-activity" period, it appears to be underestimated by a factor of two in the "low-activity" period.

However, there is another possible interpretation. As indicated in connection with Figure 5.2, there is an altitude dependence to the  $f$  factor. Could the observed increase in  $f$  with decreasing solar activity be explained by an altitude effect? For  $f$  to increase, the emission altitude would have to increase. This is contrary to what would be expected for lower solar activity levels. Because of lower exospheric temperatures, constant pressure surfaces, hence, chemical reactions and stopping ranges, would shift to lower altitudes under these conditions. Thus, if we assume our small sample is representative, MSIS-86 underestimates the high latitude atomic oxygen density by approximately a factor of two near solar-cycle minimum.

There is another variation evident. Eight of the nights show trends in which there is a definite variation in  $f$  over the course of the night. The sense of this variation (increasing or decreasing) does not seem to be a constant. Figure 5.9 shows an example of how the factor changes during the course of the night of 23-24 February 1984. On this night, there was a general increasing trend. The factor rose from less than 1.7 near 22 UT to near 5.1 after approximately 00 UT. Assuming the height of the layer stays constant throughout the night, we were not able to find any consistent patterns that could help explain this trend.

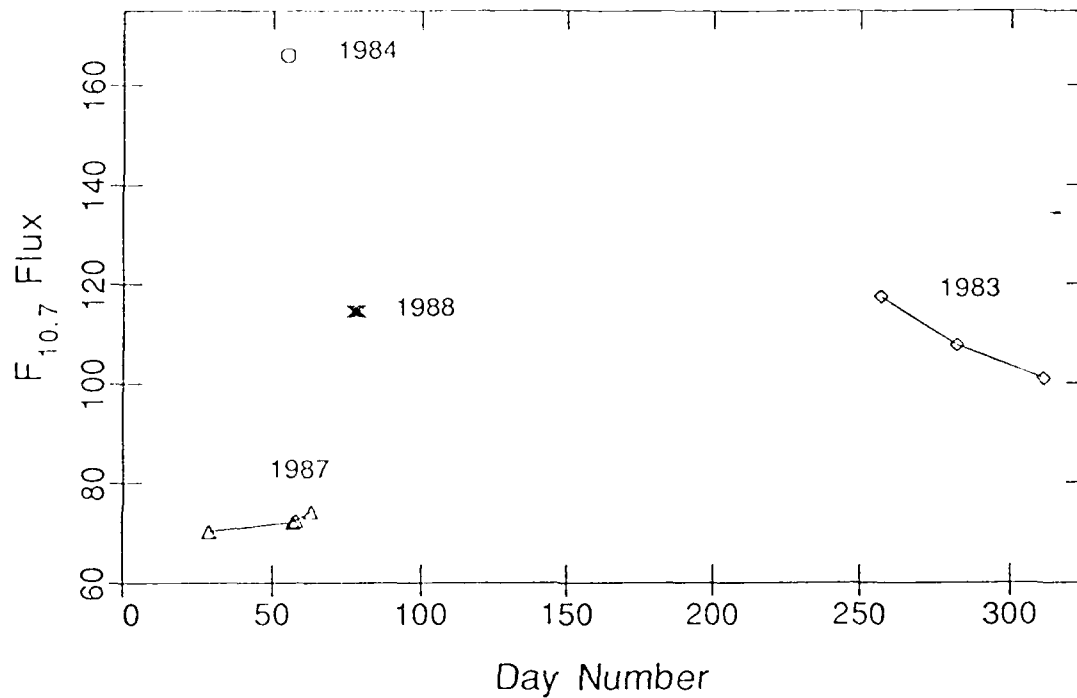


Figure 5.7. Plot of the 81-day average  $F_{10.7}$  cm flux for the data in this study from the years 1983, 1984, 1987 and 1988. 1987 is from near solar-cycle minimum. Note that there are four points for 1987 and three points for 1988.

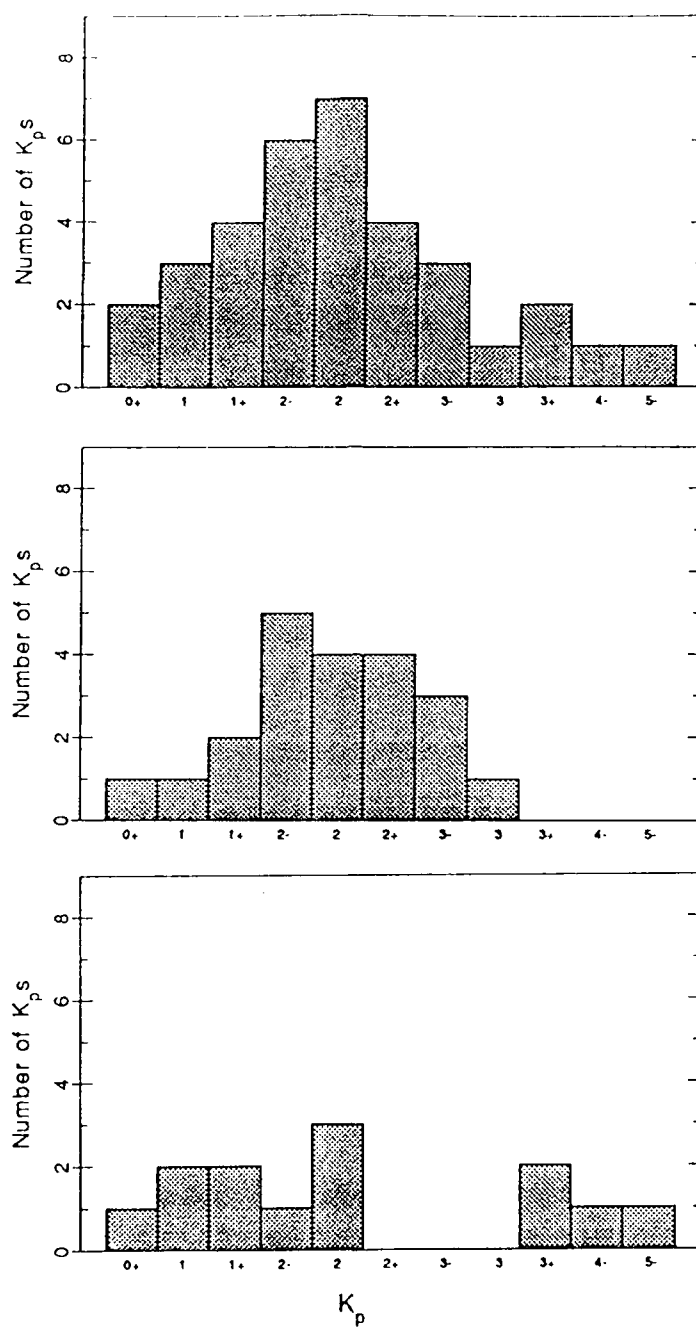


Figure 5.8. Graph showing the frequency of occurrence of  $K_p$  values for the data in this study. The  $K_p$  values are for the period of overlap on each days data. Generally, the data set was for low magnetic activity. The top plot shows the  $K_p$  for the combined data set, the middle for the data from 1983, 1984 and 1988 and the bottom for 1987.

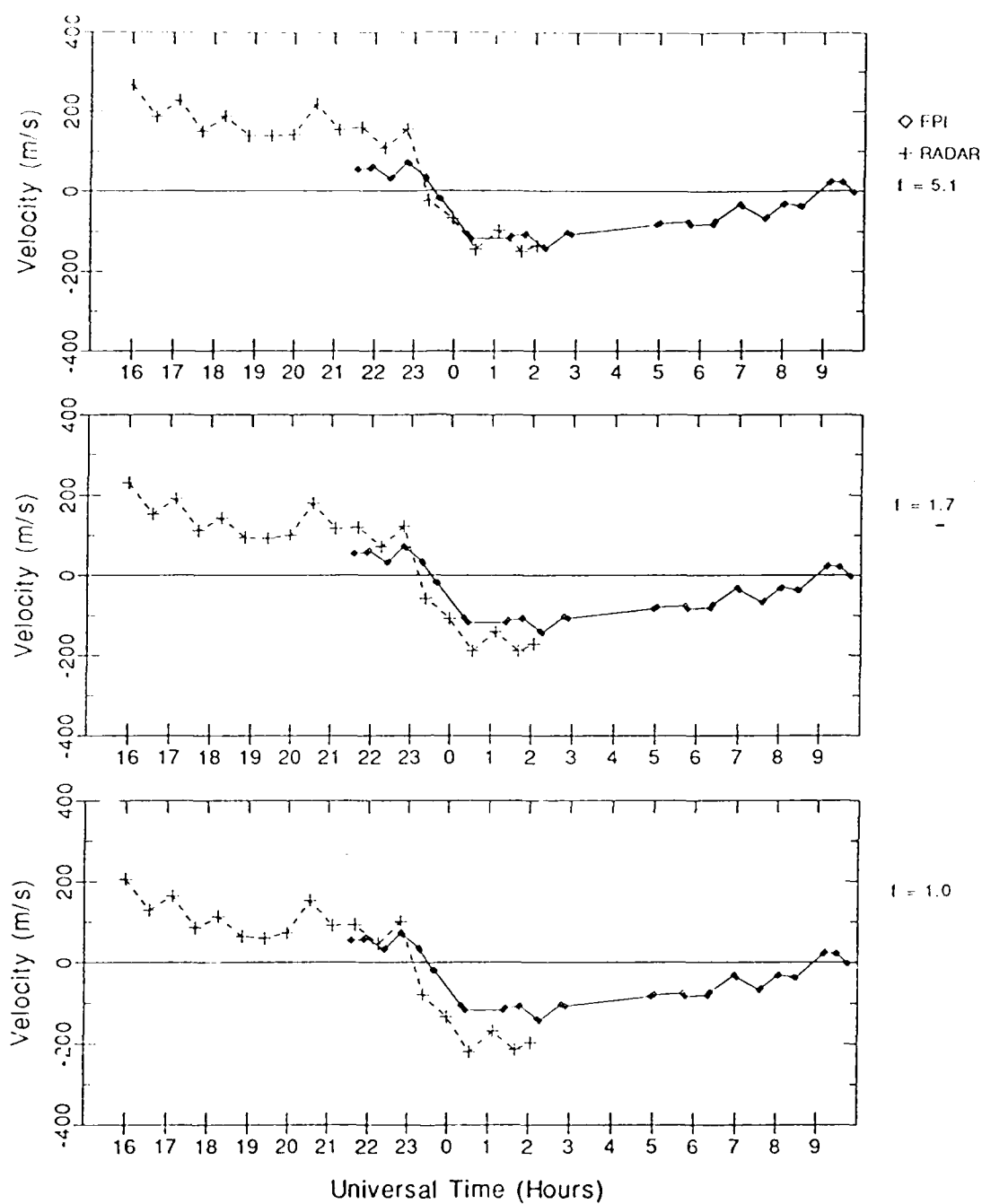


Figure 5.9. Data from 23-24 February 1984 at 231 km showing how the best  $f$  varies during the night. It changes from 1.0 near 22 UT to 5.1 near 01 UT. The radar data are shown with the large symbols (+) and dashed line. The radar data are smoothed using a running average of 3 points over 1.5 hours.

One last trend is evident in the data that bears discussion. Five of the eleven nights, at times, show significant differences between the FPI winds measured to the north and those measured to the south. A good example of this occurred on 23–24 February 1984. Several views of the winds for this night are presented in Figures 5.9 thru 5.11. Figure 5.9 shows the winds plotted at various factors ranging from 1.0 to 5.1. Figure 5.10 shows the FPI data of Figure 5.9 broken out into measurements made in the geomagnetic north and south direction from the observation site. The radar data is the dashed curve with the larger symbols. Figure 5.11 gives representative error bars for this night. The altitude of these figures is 231 km. If we assume that the FPI data was calibrated properly and the zero velocity level was correctly established, in Figure 5.10 we can see significant gradients, on the order of  $0.3$  to  $0.5 \text{ ms}^{-1} \text{ km}^{-1}$ , between 00 and 0615 UT. Although details differ, the two independent reductions for this day (Figure 3.3) both clearly show these gradients. This gives strong support to their reality. Initially, the measurements made to the south are more equatorward than those to the north which are, at times, poleward. This trend reverses at 0215 UT. The north measurement becomes more equatorward than the south. In both cases, the gradient is larger than can be explained by the error bars (see Figure 5.11). During the period of FPI gradients, a large  $f$  is needed to bring the radar and FPI data into agreement (see Figure 5.9).

*Hernandez and Roble* [1976a, 1976b, 1979a] report seeing this type phenomena in the FPI data from Fritz Peak at about  $50^\circ \Lambda$ . They attributed this latitudinal difference in the winds to enhanced latitudinal temperature gradients that are larger in the summer at mid-latitudes. *Burnside et al.* [1981] also see a latitudinal gradient at Arecibo. They attribute the difference in the winds to the midnight temperature enhancement seen at Arecibo and the pressure bulge associated with it. *Meriwether et al.* [1984] report it at Sondrestrom and attribute it to a midnight abatement between the evening and morning convection cells. In our example, auroral heating is the most likely cause of this gradient. When the auroral oval is near Sondrestrom, particle precipitation or joule heating could heat the neutral atmosphere in a local region causing temperature gradients to be set up and hence pressure gradients. Depending on the location of the heating with respect to the location observed, different winds would be deduced. The neutral densities would also be affected. Increased temperatures would lead to bigger scale heights and greater  $F$ -region neutral densities than those predicted by MSIS. The radar-derived winds, which rely on MSIS, would be affected as well. We would expect the radar winds to

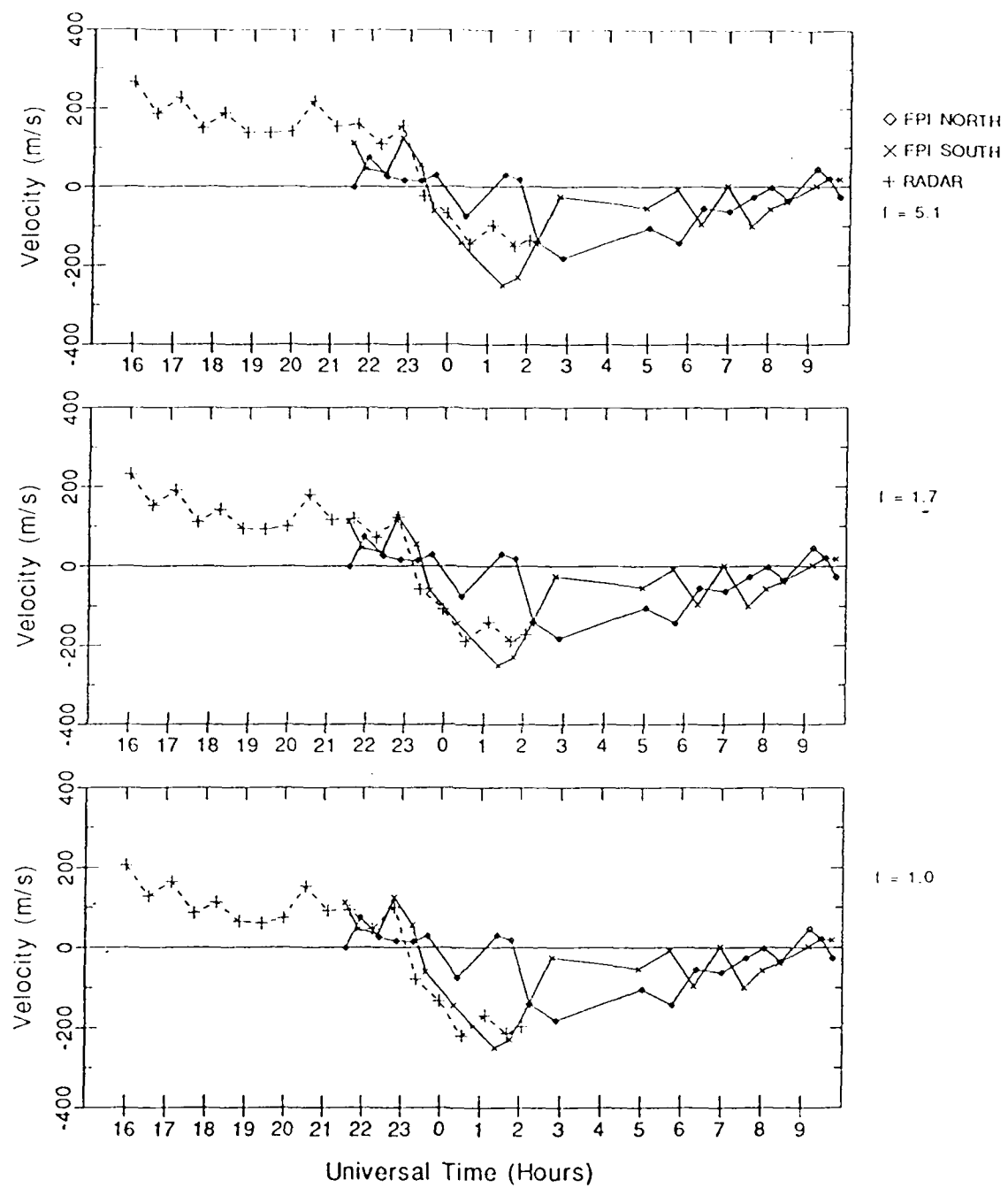


Figure 5.10. Gradients in the FPI winds deduced from observations to the north and south on 23-24 February 1984. Large gradients appear between 01 and 06 UT. Refer also to Figure 3.3 for a second independent reductions of the FPI data.

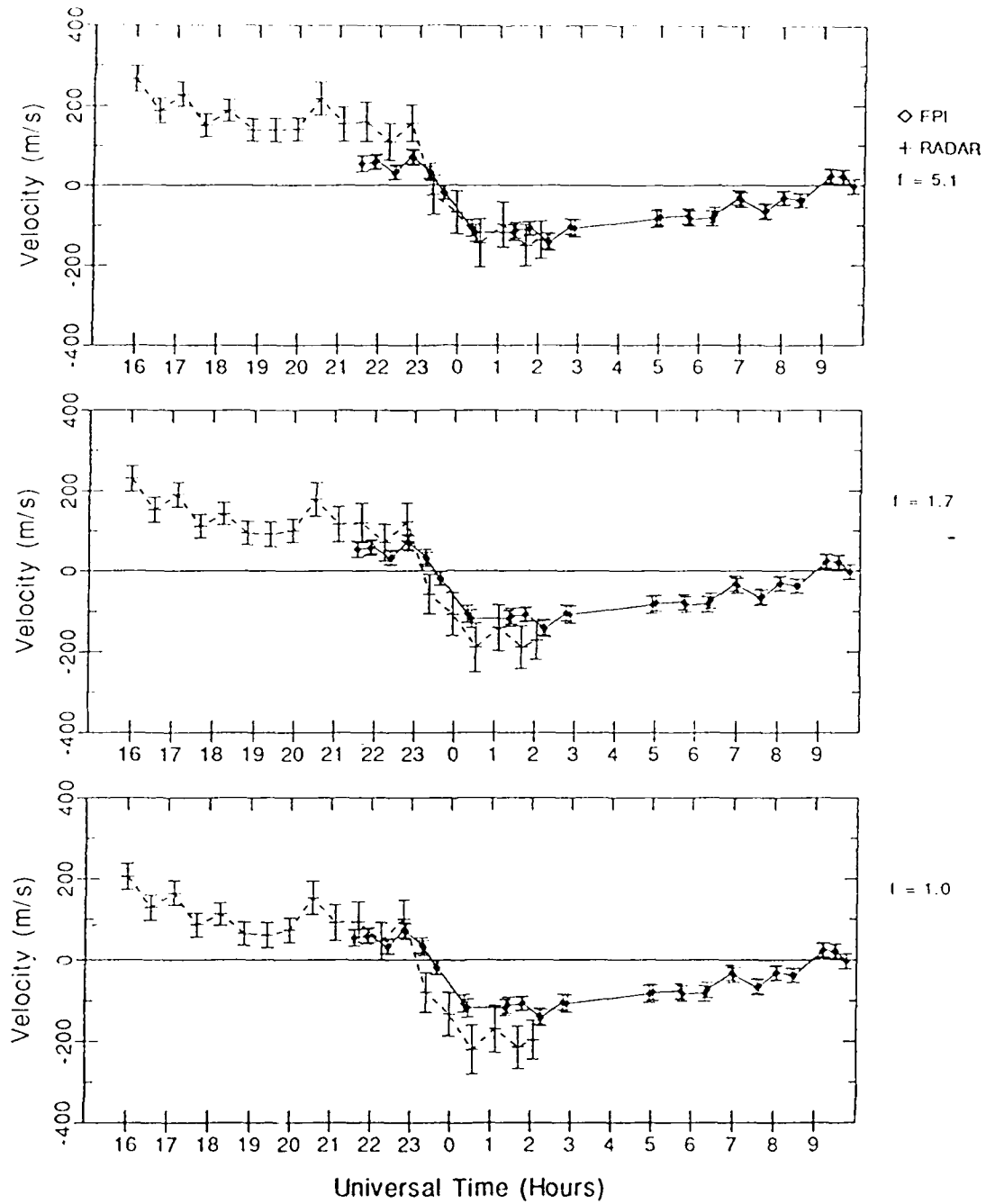


Figure 5.11. Data from 23-24 February 1984 showing representative error bars on the FPI and radar data. To radar data are smoothed using a running average of 3 points over 1.5 hours.

require a higher  $f$ , and therefore a higher density, to achieve agreement with the FPI in this region. This explanation would account for the change in the  $f$  value and the occurrence of the latitude gradient.

There are a couple of special cases to consider. The night of 17-18 March 1988 exhibits an unusually low factor of  $f$ , 1.0. Figure 5.12 shows the radar and FPI data while Figure 5.13 shows representative error bars. The radar plot meeting the criteria of the most points within one standard deviation of the FPI is at  $f = 1.0$ . This unusually low factor would imply a large reduction in the neutral atmospheric atomic oxygen density compared to the rest of the data set. We were not able to find any consistent pattern that could explain this unusually low value for  $f$ .

The night of 26-27 February 1987 is another anomaly. On this night, an unusually high value of  $f$  was needed to bring the radar into agreement with the FPI. These data are shown in Figure 5.14 without error bars and in Figure 5.15 with error bars. Clearly, in looking at these two figures, the  $f$  exceeded 5.1. This is more than a factor of 3 increase above the 1.7 level previously discussed. Again, the average  $K_p$  for the night and the  $F_{10.7}$  cm flux are typical of the other days in the data set. The  $A_p$  does increase from 6 on the 26th to 12 on the 27th, an increase of 6, but again, this is not the only day in the data set that has this happen and the values are very low anyway. This is a remarkably large increase, and there is no apparent reason for it. Either the atomic oxygen density is three times what MSIS would predict or there are undetected instrumental problems.

One final effect is evident on several days, waves. The data from 4 March 1987 show a particularly good example, particularly between 0230 and 0400 UT. The data for 173, 228 and 283 km are presented in Figure 5.16. A plot with representative error bars is shown in Figure 5.17. The factor used to produce these plots was 3.4. The period of the radar oscillation (peak to peak) at all altitudes is the same, the order of 30 to 45 minutes. The amplitude of the oscillation increases with altitude, especially between 173 and 228 km. It also appears in the electron density (not shown). Additionally, the peak between 03 UT and 04 UT, for example, exhibits a negative phase shift with altitude, i.e., it occurs 15 minutes earlier at 283 km than at 173 km. For a 30 to 45 minute period, that would imply a 200 to 300 km vertical wavelength. This would also help explain why the wave is not evident in the FPI data, the wavelength is too small. The point near 04 UT in the FPI data appears to be anomalous. While two points are shown, the one with the stronger poleward velocity arises from a very strong line-of-sight observation to the north. The other

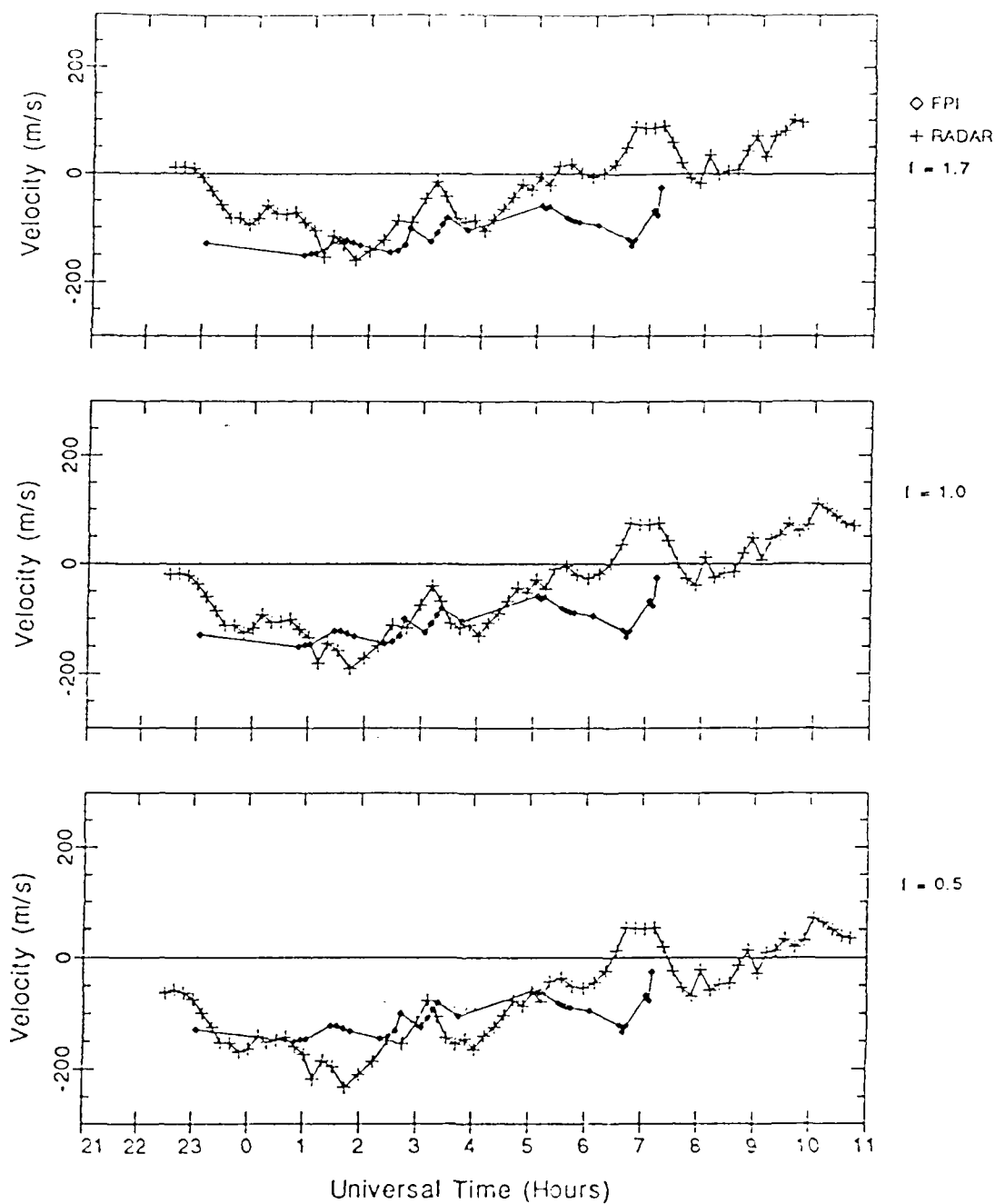


Figure 5.12. Plots of data for 17-18 March 1988 showing the unusually low  $f$  value required for agreement,  $f = 1.0$ . The radar data are from 231 km and were smoothed using a 1 hour running average.

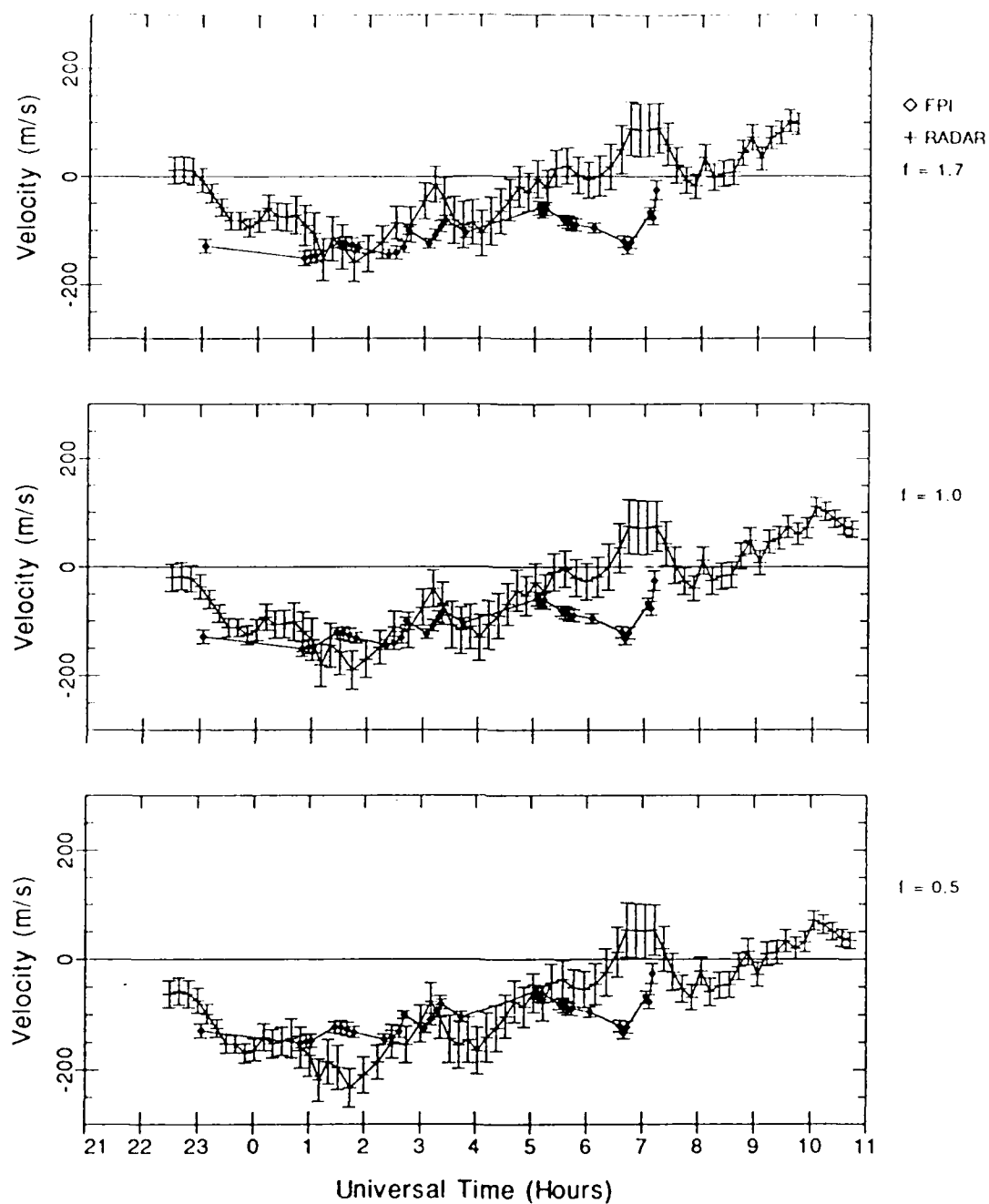


Figure 5.13. Plots of data for 17-18 March 1988 showing error bars.

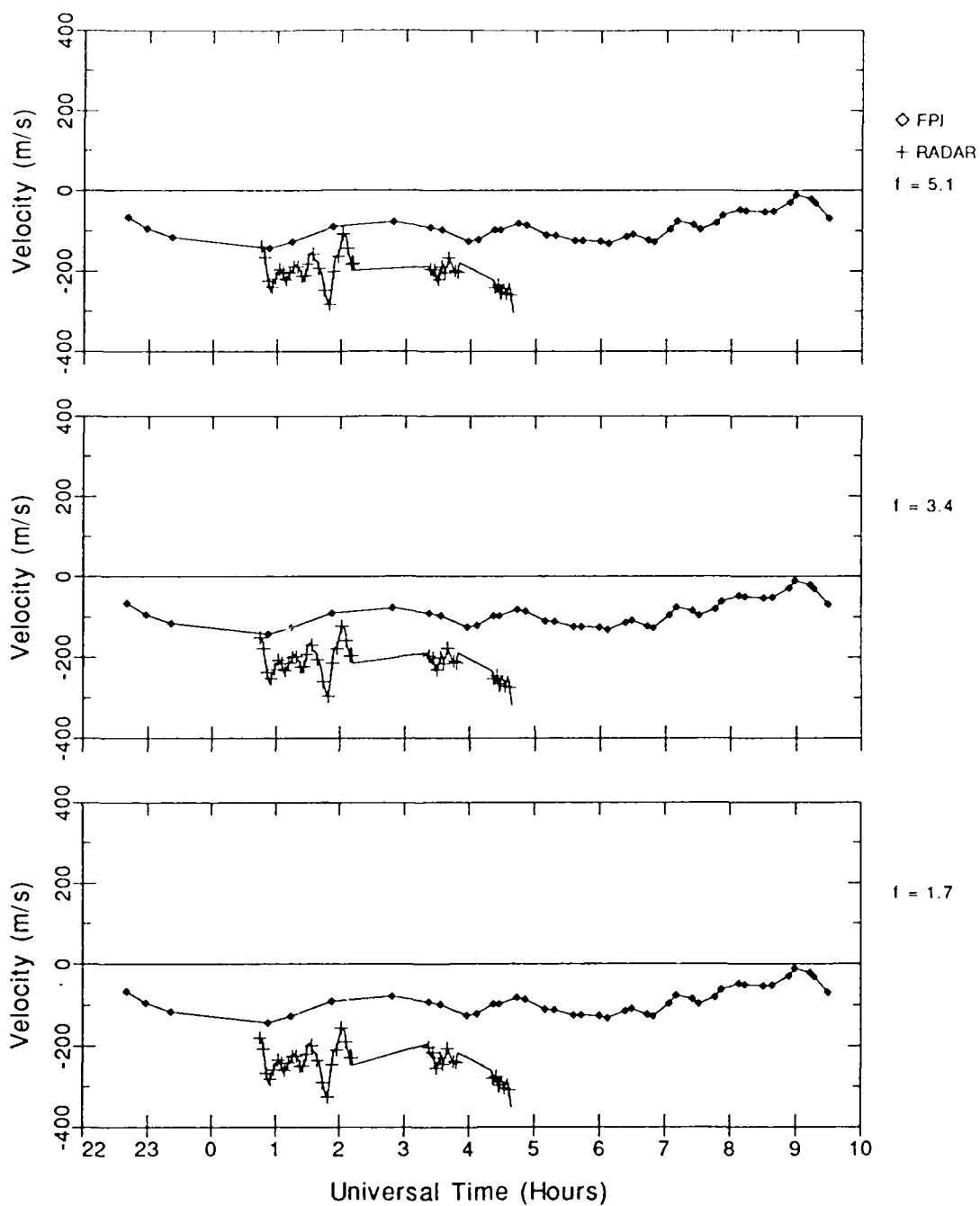


Figure 5.14. Plots of the data for 26–27 February 1987 showing the unusually high value needed for agreement,  $f > 5.1$ . The radar data was smoothed using a 1 hour running average. The radar altitude is 228 km.

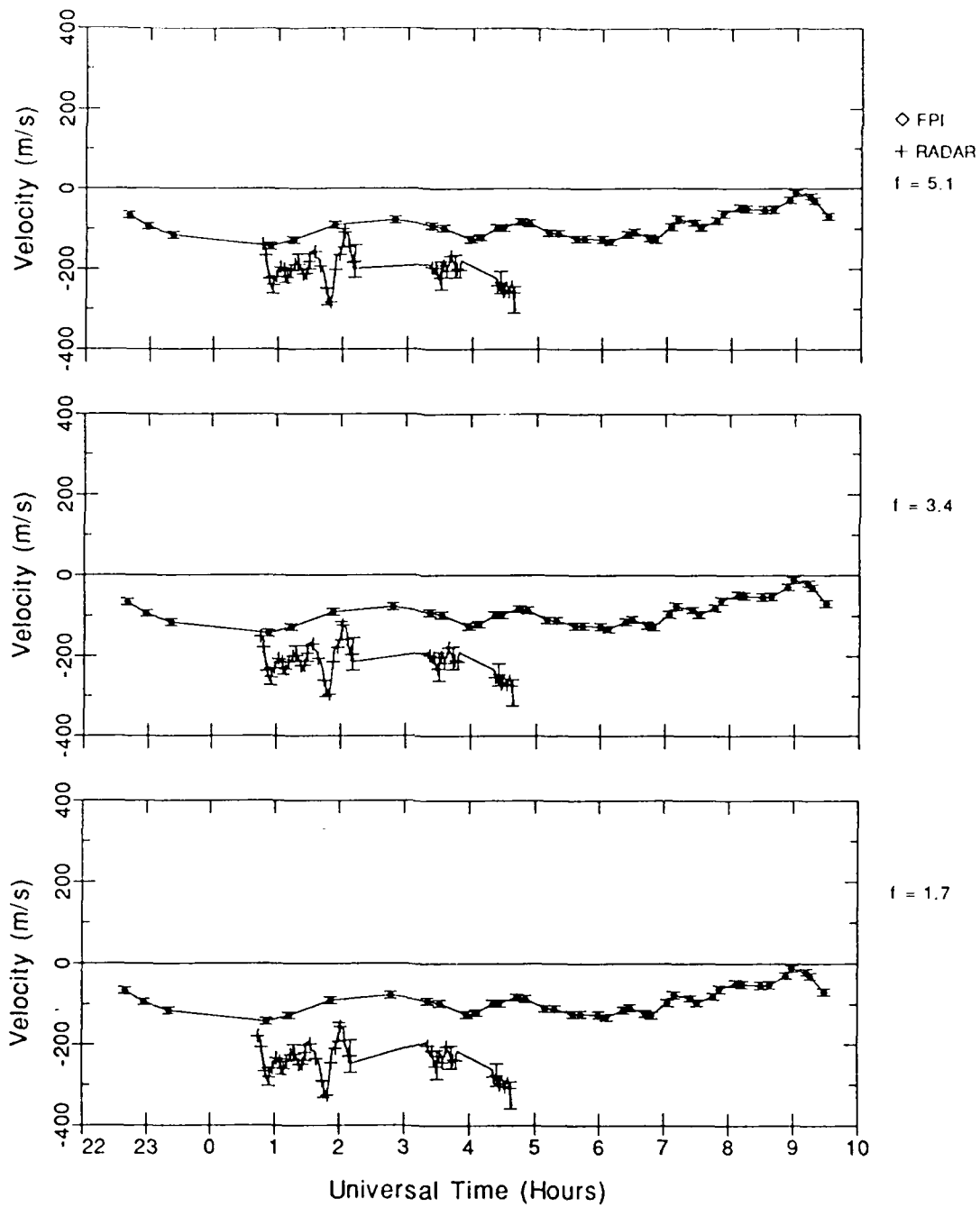


Figure 5.15. Plots showing the data of 26–27 February 1987 showing representative error bars. For clarity, only every 10th error bar is plotted on the radar data. The altitude is 228 km.

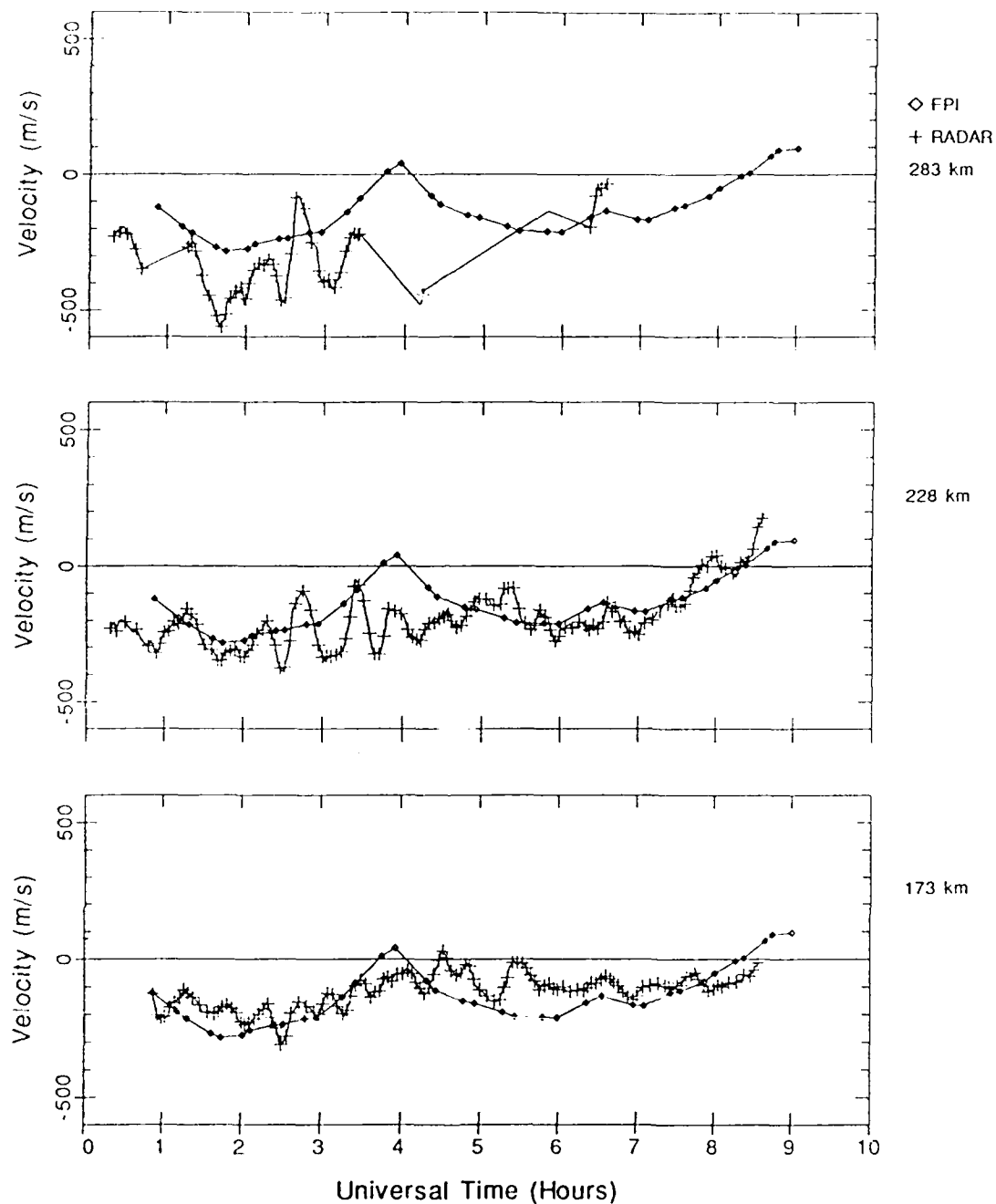


Figure 5.16. FPI and radar neutral winds for the night of 4 March 1987 at three altitudes: 173, 228, and 283 km. The factor used to produce these plots was  $f = 3.4$ . The radar data are smoothed using a 10 minute running average. For clarity, every 3rd radar point has a symbol plotted.

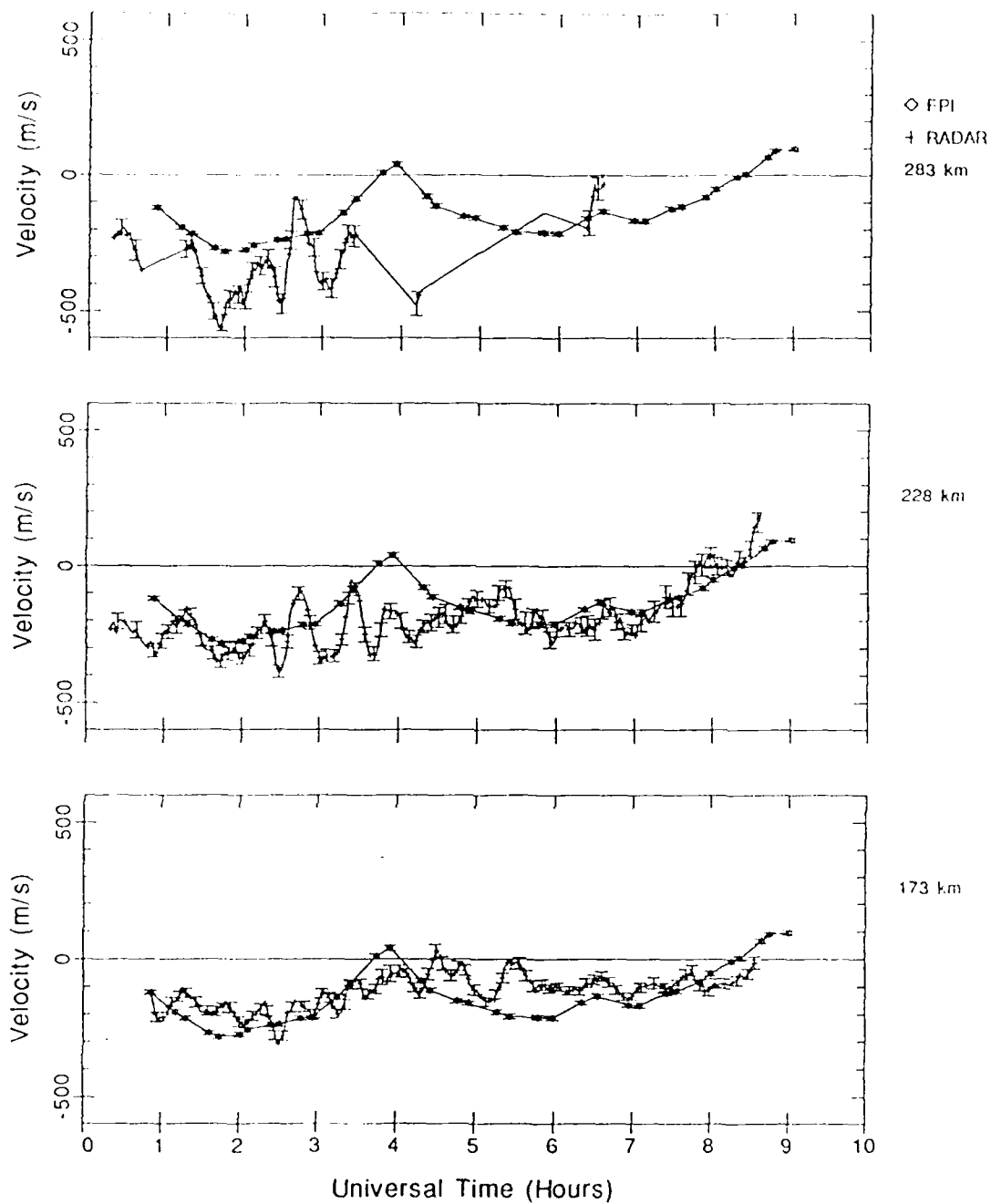


Figure 5.17. FPI and radar neutral winds for the night of 4 March 1987 with the associated error bars at three altitudes: 173, 228, and 283 km. The radar data are smoothed using a 10 minute running average. For clarity, every third radar point has been plotted with a symbol.

one, slightly earlier, arises from the interpolation of the first point to the time of an observation to the south. Not only is the velocity of the first point different from the radar velocity, but the temperature is approximately  $400^{\circ}\text{K}$  greater than for adjacent points [Niciejewski, private communication, 1990]. Beyond noting that the behavior of the FPI data point at 04 UT is anomalous in both velocity and temperature, its behavior has not been understood.

In addition to these oscillations that behave like large-scale gravity waves, there are many variations throughout the night that take place on time scales of about 30 minutes. In contrast to the radar-derived winds, the FPI winds do not show these waves and short time-scale variations. To some extent, this happens because the FPI does not have the time resolution of the radar in this operating mode and it also tends to washout altitude variations because it averages over the emission layer. Additionally, it may be because most of the motion is in the vertical direction instead of the horizontal. For instance, the radar pointing at an 80 degree elevation angle is much more sensitive to vertical motion than horizontal as previously discussed. Thus, the 300 m/s peak-to-peak wind variation shown at 228 km between 0230 and 0245 UT might only be a 50 m/s peak-to-peak variation in vertical velocity. (The radar cannot distinguish between vertical and horizontal motion. It is sensitive only to the projection along the magnetic field.) By contrast, the reduction of the FPI data by combining observations to the magnetic north and south at  $45^{\circ}$  elevation angles to obtain the horizontal winds would not detect a vertical wind. It would, however, easily detect a horizontal wind of the magnitude (300 m/s) deduced from the radar data, if the velocity fields were at all close to uniform over the two points of observation. Thus, the combined data sets indicate that the oscillations are vertical not horizontal.

The above behavior between 0200 and 0400 UT could have resulted from increased magnetic activity. The Kp for 00–03 UT rose to 4-, up from 2 during the 21–24 UT interval. This would be consistent with observations of large-scale gravity waves or traveling ionospheric disturbances by *Testud* [1970], *Hunsucker* [1982].

The contributions of the parallel ion velocity and diffusion to the meridional wind are shown in Figure 5.18 through 5.20. Each figure represents one altitude 173, 228 and 283 km, respectively, for each of the three values: the horizontal wind, the parallel ion velocity projected onto the horizontal and the diffusion velocity projected onto the horizontal. The sign convention is for positive to be a wind to the north. At all three altitudes it is obvious that most of the structure in the wind

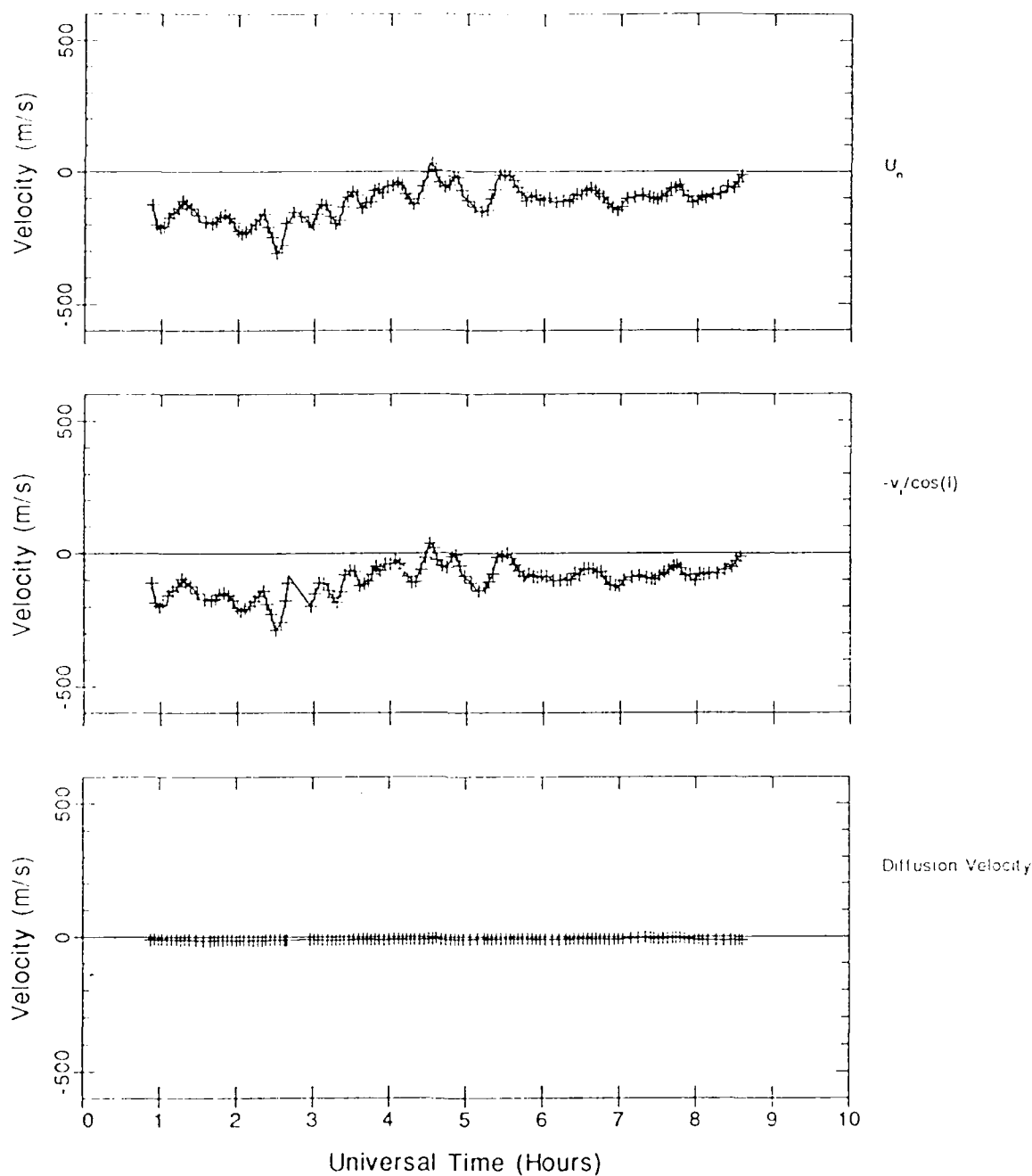


Figure 5.18. Plots of the horizontal neutral wind, parallel ion velocity and diffusion velocity for 4 March 1987 at 173 km. The data are projected onto the horizontal and the signs adjusted such that a positive value is a contribution to the wind toward the north. The data are smoothed using a running average over 10 minutes. For clarity, every third data point are plotted with a symbol. For this plot,  $f = 3.4$ .

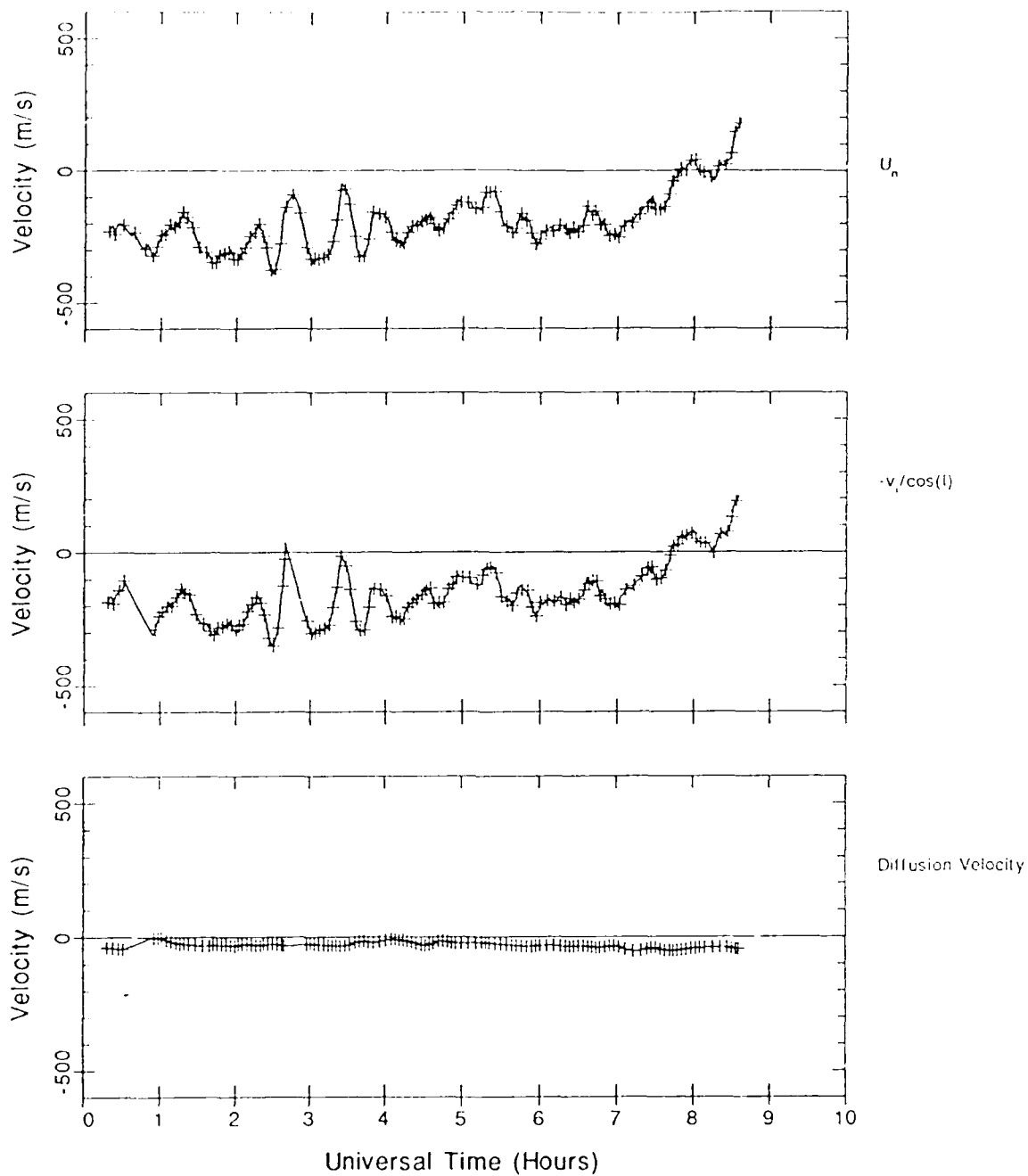


Figure 5.19. Plots of the horizontal neutral wind, parallel ion velocity and diffusion velocity for 4 March 1987 at 228 km. The data are projected onto the horizontal and the signs adjusted such that a positive value is a contribution to the wind toward the north. The data are smoothed using a running average over 10 minutes. For clarity, every third data point are plotted with a symbol. For this plot,  $f = 3.4$ .

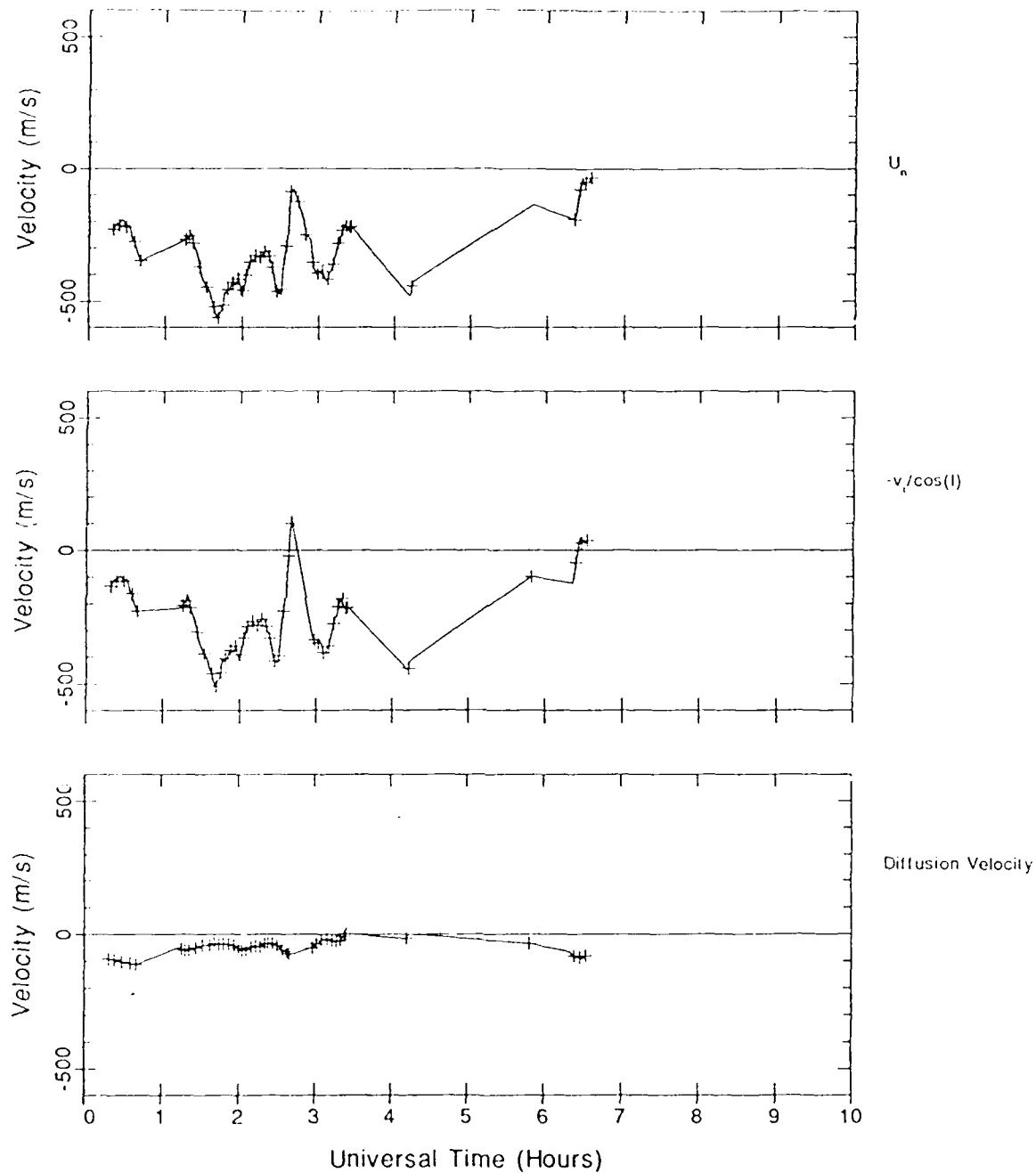


Figure 5.20. Plots of the horizontal neutral wind, parallel ion velocity and diffusion velocity for 4 March 1987 at 283 km. The data are projected onto the horizontal and the signs adjusted such that a positive value is a contribution to the wind toward the north. The data are smoothed using a running average over 10 minutes. For clarity, every third data point are plotted with a symbol. For this plot,  $f = 3.4$ .

originated from structure in the ion velocity not the diffusion velocity. It should be noted that the oscillations are also evident in the electron density which implies they are real oscillations.

It is interesting to note that, as expected, the contribution to the horizontal neutral wind from the diffusion term is smaller at the lower altitudes. This is the reason the lower level neutral wind (Figure 5.16, 173 km) shows much less variation when  $f$  is changed than the other altitudes.

The behavior described above is consistent with the description of large-scale gravity waves and travelling ionospheric disturbances. These perturbations are indicative of the dynamics associated with the high latitude auroral regions [Wickwar, 1989].

## CHAPTER VI

### CONCLUSIONS

As we can see from the discussion in Chapter V, there is a lot happening in the high latitude polar-cap region. The ISR-FPI wind comparison we have performed is the first of its kind at such high latitudes. Much has been learned from this research and much has been identified that we don't understand. The intent of this final chapter is to outline what we have learned, and more importantly, where we need further research to understand the processes at such high latitudes.

#### 6.1. Results

This research shows that agreement can be obtained between the ISR and FPI techniques for measuring the horizontal neutral winds. This agreement is best for altitudes near 230 km. To first order, both instruments agree. However, closer examination shows differences between them that can be affected or controlled by the choice of an  $f$ -factor in the derivation of the radar winds. The variation of this factor provides us with information about the  $O^+$ -O collision cross section and the atomic oxygen density.

Our results show that an  $f$ -factor of between 1.7 and 3.4 is most frequently needed to obtain good agreement between the two techniques. That a large increase is needed is in agreement with *Burnside et al.* [1987]. They imply that the product of the  $O^+$ -O collision cross section for momentum transfer and the atomic oxygen density has to be increased by a sizable amount. Our results further imply that the amount is at least as big as the factor of 1.7 found by *Burnside et al.*

While *Burnside et al.* were able to suggest that MSIS-83 was on average correct for the Arecibo data, we cannot make that conclusion for Sondrestrom, as will be discussed shortly. If MSIS-83 were correct, then the average Arecibo results show the  $O^+$ -O cross section has to be increased by a factor of 1.7.

If we accept a factor of 1.7 for the cross section, then our results show that at high latitudes the MSIS-86 model densities most frequently vary from being correct to being too small by a factor of 2. Furthermore, we found a solar-cycle (or solar activity) dependence on how well MSIS-86 predicts these atomic oxygen densities. This has not previously been noted. We found an underestimate by MSIS-86 by a factor of 2 near solar-cycle minimum ( $F_{10.7} \sim 70$  in 1987) while for moderate solar

activity a factor of 1 was needed ( $F_{10.7} > 100$  for 1983, 1984 and 1988). *Burnside et al.* [1987] suggested MSIS-83 might be less reliable in predicting [O] for solar-cycle minimum. However, this is the first time a solar-cycle variation has been inferred and quantified. Although our results used the updated MSIS-86 model, our numerical experiment in Chapter III showed practically no difference between the two versions of the model for deducing the winds.

If we were to increase the  $O^+$ -O cross section by 3.4, the implication would be that MSIS-86 [O] is most frequently correct at solar-cycle minimum and is underestimated by a factor of two during periods of moderate solar activity. However, a further implication would be that the MSIS [O] densities at Arecibo were usually underestimated by a factor of two. This interpretation does not seem reasonable. Furthermore, a factor of 3.4 for the cross section would be inconsistent with the factors found by other procedures [e.g., *Roble, 1975; Carlson and Harper, 1977*].

In view of these findings, an operational conclusion is that the radar data should be reduced using  $f = 1.7$  to obtain the best estimate of meridional winds.

There were some deviations from the most frequent value of 1.7. These extremes were a factor 0.3 less and a factor of 3 more. Assuming the cross section had to be increased by a factor of 1.7, these results imply a day with a factor of 0.3 lower [O] and a day with a factor 3 higher [O] than predicted by MSIS-86. These are significant variations from the model predictions.

In addition, we observed time-variations in how  $f$  varies over the course of many nights. On some nights it increased, on others it decreased. An increase in  $f$  implies an increase in [O] relative to MSIS and vice versa. Again, this has not previously been observed. We were not able to identify any consistent pattern that could explain this phenomena, but we did suggest auroral heating on days when  $f$  increased, as discussed below.

We identified that gradients in the meridional components of the neutral winds often exist in the FPI data. These gradients coincide with times when the factor needed to bring the radar into agreement with the FPI increased. Gradients have been observed by *Hernandez and Roble* [1976a, 1976b, 1979a], *Burnside et al.* [1981], and *Meriwether et al.* [1984]. These authors attribute them to various causes. We attribute them to auroral heating which acts to increase the neutral temperature thereby increasing [O] above levels predicted by MSIS. The radar wind, which uses the lower MSIS [O], will then require a large  $f$  to agree with the FPI. This was clearly observed on 23-24 February 1984.

Finally, we have seen strong evidence of large-scale gravity waves on 4 March 1987. They show up well in the radar data but not the FPI data. The source of these waves is not clear, but they appear after a significant increase in  $K_p$ , in agreement with previous findings of excitation by auroral processes [Testud, 1970; Hernandez and Roble, 1976b; Hunsucker, 1982].

## 6.2. Topics for Further Research

As with any research, the more one learns, the more one realizes what one doesn't know. This study is no exception. Listed below are some areas I have identified that require further research:

1. Because we had an insufficient amount of data over a wide enough variety of geophysical conditions, we were forced to do a rather crude wind comparison. A better comparison should be done with a wider variety of data to better identify which factor,  $[O]$  or the collision cross section, is in need of adjustment. If the 1984 through 1986 FPI data could be salvaged, this could be done. Otherwise, it is important to continue to operate the FPI and ISR in modes and at times to maximize the possibility of acquiring good simultaneous data.
2. Study the solar-cycle dependence on the factor  $f$ . Use a wider range of data from solar-cycle maximum and minimum to clarify the difference in the model between the two extremes and see if our results persist.
3. Study the trend of  $f$  to increase or decrease throughout the night. Try to determine its cause by examining other radar data (electron densities, temperatures and convection velocities) as well as satellite data.
4. Explore the source of the gradients observed in the FPI data and attempt to resolve their cause. Again, include more radar observations to accomplish this.
5. Explore the large-scale gravity waves we observed on 4 March 1987. Information on the source may be learned from sudden changes in the convection pattern or in the ion temperatures. More information about the waves may come from studying the vertical velocities that can be derived from the FPI. Above all, more experiments have to be made with high time resolution. Periods of about 30 minutes imply the observing sequence has to take no more than 15 minutes. To that end it would be helpful if the FPI were to

again make observations in the magnetic meridian instead of in geographic coordinates.

This has been a rewarding study in that it has done much to reveal some of the processes and interactions occurring at high latitudes. It has also raised many questions. With each study like this we move closer to understanding and eventually predicting the processes observed in the upper atmosphere.

## REFERENCES

- Armstrong, E. B., Doppler shifts in the wavelength of OI 6300 line in the night airglow, *Planet. Space Sci.*, *17*, 957-974, 1969.
- Banks, P. M., Collisions frequencies and energy transfer ions, *Planet. Space Sci.*, *14*, 1105-1122, 1966.
- Bevington, Philip R., *Data reduction and Error Analysis for the Physical Sciences*, McGraw-Hill Book Company, New York, 1969.
- Burnside, R. G., F. A. Herrero, J. W. Meriwether, and J. C. G. Walker, Optical observations of thermospheric dynamics at Arecibo, *J. Geophys. Res.*, *86*, 5532-5540, 1981.
- Burnside, R. G., R. A. Behnke, and J. C. G. Walker, Meridional neutral winds in the thermosphere at Arecibo: Simultaneous incoherent scatter and airglow observations, *J. Geophys. Res.*, *88*, 3181-3189, 1983.
- Burnside, R. G., C. A. Tepley, and V. B. Wickwar, The O<sup>+</sup>-O collision cross-section: Can it be inferred from aeronomical measurements?, *Annales. Geophysical*, *5A*, 343-350, 1987.
- Carlson, H. C., and R. M. Harper, An experimental estimate of the O<sup>+</sup>-O resonant charge transfer cross section, collision frequency, and energy transfer rate, *J. Geophys. Res.*, *82*, 1144-1148, 1977.
- Dalgarno, A., The mobilities of ions in their parent gases, *Phil. Trans. Roy. Soc.*, *A250*, 426-439, 1958.
- Dalgarno, A., and J. C. Walker, The red line of atomic oxygen in the day airglow, *J. Atmos. Sci.*, *21*, 463-474, 1964.
- Evans, J. V., Theory and practice of ionosphere study by Thomson scatter radar, *Proceedings of the IEEE*, *4*, 496-530, 1969.
- Hays, P. B., and R. G. Roble, Direct observation of thermospheric winds during geomagnetic storms, *J. Geophys. Res.*, *76*, 5316-5321, 1971.
- Hocht, J. H., A. B. Christensen, D. J. Strickland, and R. R. Meier, Deducing composition and incident spectra from ground-based auroral optical measurements: Variations in oxygen density, *J. Geophys. Res.*, *94*, 13,553-13,563, 1989.
- Hedin, A. E., A revised thermospheric model based on mass spectrometer and incoherent scatter data: MSIS-83, *J. Geophys. Res.*, *88*, 10,170-10,188, 1983.
- Hedin, A. E., MSIS-86 thermospheric model, *J. Geophys. Res.*, *92*, 4649-4662,

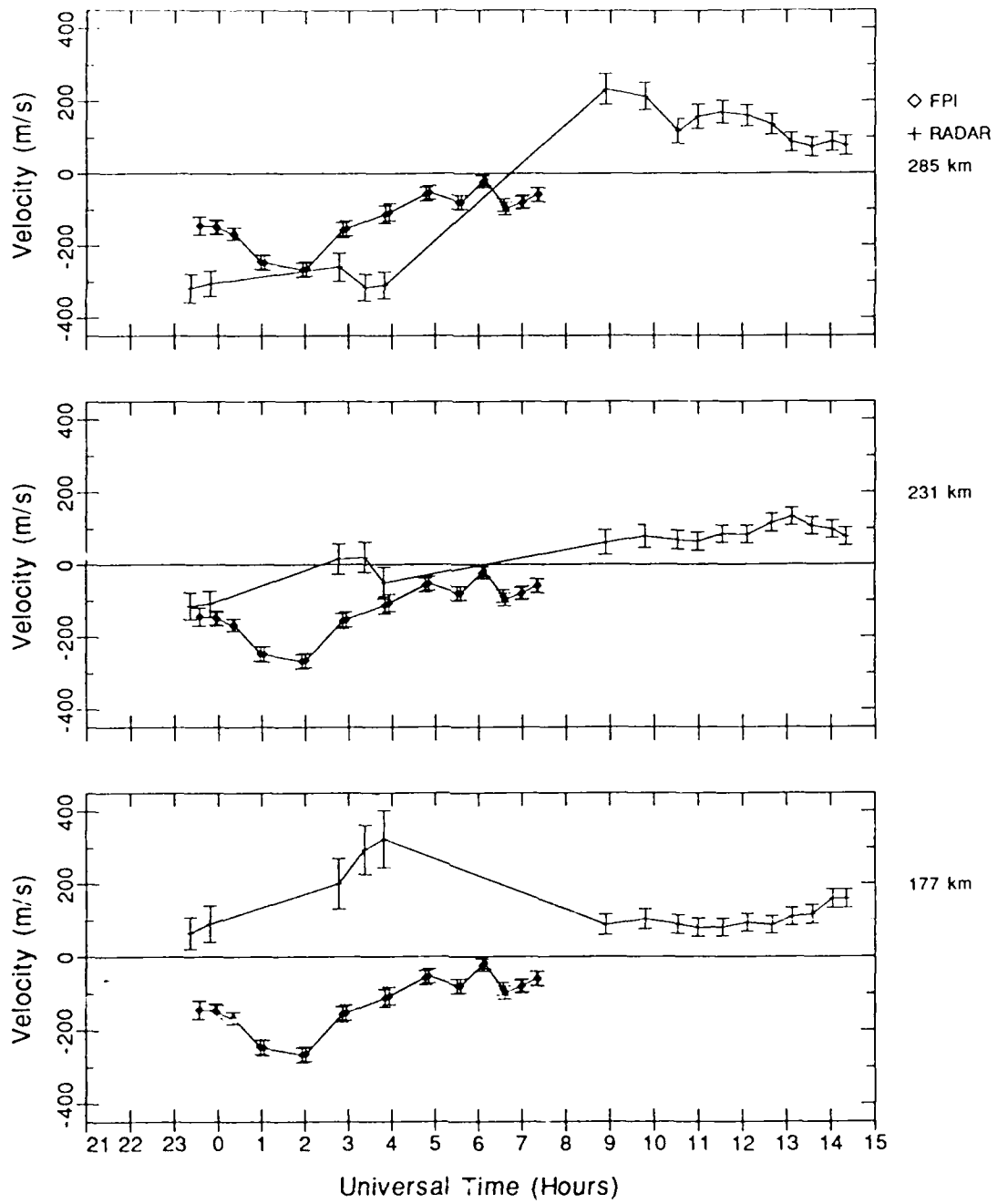
- 1987.
- Hedin, A. E., C. A. Reber, G. P. Newton, N. W. Spencer, H. C. Brinton, H. G. Mayr, and W. E. Potter, A global thermospheric model based on mass spectrometer and incoherent scatter data, MSIS 2, composition, *J. Geophys. Res.*, *82*, 2148-2156, 1977.
- Hernandez, G., Measurement of the thermospheric temperature and winds by remote Fabry-Perot spectrometry, *Opt. Engin.*, *19*, 518-532, 1980.
- Hernandez, G., *Fabry-Perot Interferometers*, Cambridge University Press, New York, New York, 1986.
- Hernandez, G., and R. G. Roble, Direct measurements of thermospheric winds and temperatures, 1, Seasonal variations during geomagnetically quiet periods, *J. Geophys. Res.* *81*, 2065-2074, 1976a.
- Hernandez, G., and R. G. Roble, Direct measurements of nighttime thermospheric winds and temperatures, 2, Geomagnetic storms, *J. Geophys. Res.*, *81*, 5173-5181, 1976b.
- Hernandez, G., and R. G. Roble, On divergence of thermospheric meridional winds at midlatitudes, *Geophys. Res. Lett.*, *6*, 294-296, 1979a.
- Hernandez, G., and R. G. Roble, Thermospheric dynamics investigations with very high resolution spectrometers, *Appl. Opt.*, *18*, 3376-3385, 1979b.
- Hunsucker, R. D., Atmospheric gravity waves generated in the high-latitude ionosphere: A review, *Rev. Geophys. and Space Phys.*, *20*, 293-315, 1982.
- Jacchia, L. G., Revised static models of the thermosphere and exosphere with empirical temperature profiles, *Smithson. Astrophys. Obs. Spec. Rep.*, 332, 1971.
- Johnson, R. M., V. B. Wickwar, R. G. Roble, and J. G. Luhmann, Lower-thermospheric winds at high latitude: Chatanika radar observations, *Annales. Geophys.*, *5A*, 383-404, 1987.
- Kelly, J. D., Sondrestrom radar-initial results, *Geophys. Res. Lett.*, *10*, 1112-1115, 1983.
- Link, R., J. C. McConnell, and G. G. Shepherd, A self consistent evaluation of the rate constants for the production of the OI 6300-Å airglow, *Planet. Space Sci.*, *6*, 589-594, 1981.
- Meier, R. R., D. J. Strickland, J. H. Hecht, and A. B. Christensen, Deducing composition and incident electron spectra from ground-based auroral optical measurements: A study of auroral red line processes, *J. Geophys. Res.*, *94*, 13541-13552,

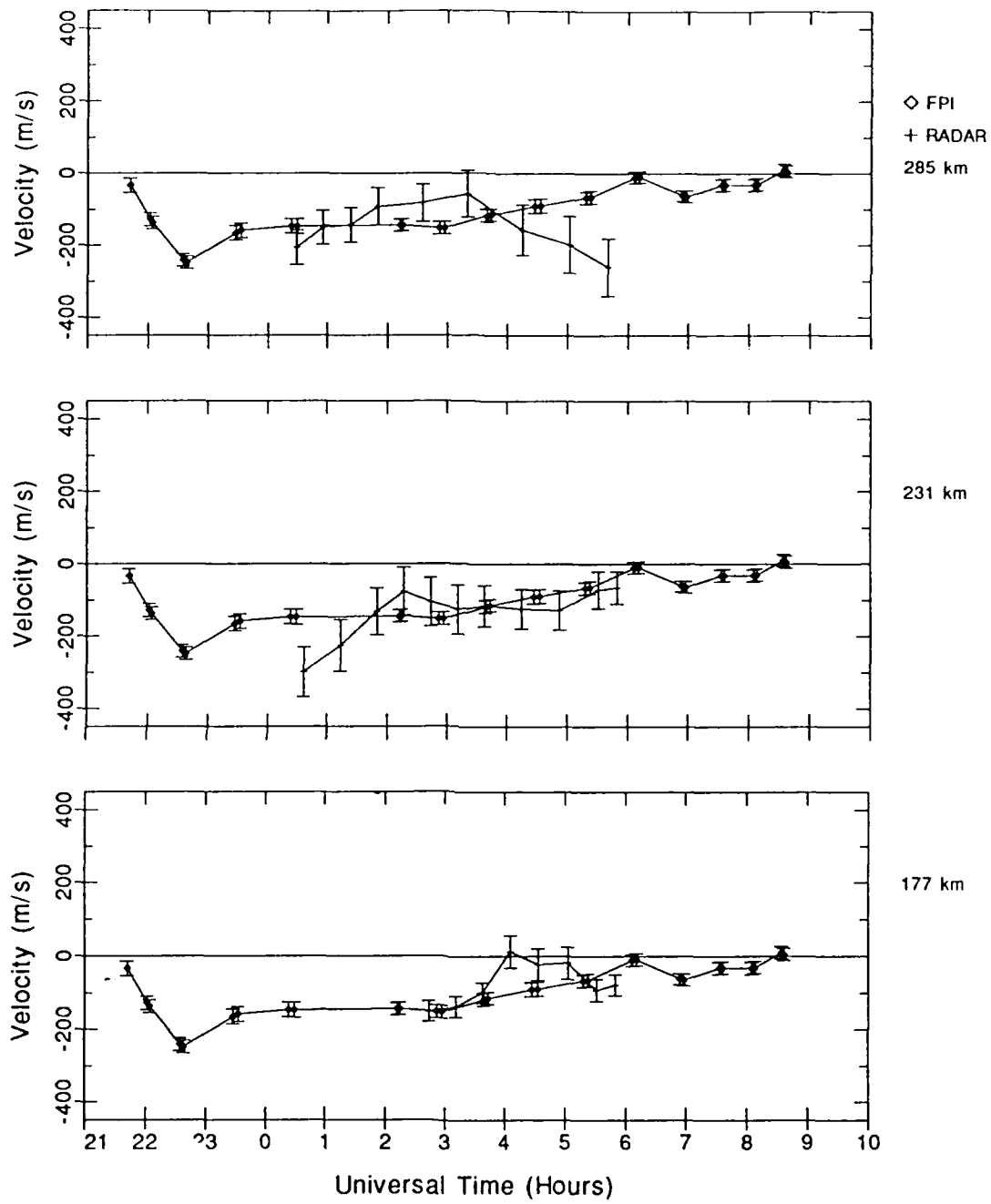
1989.

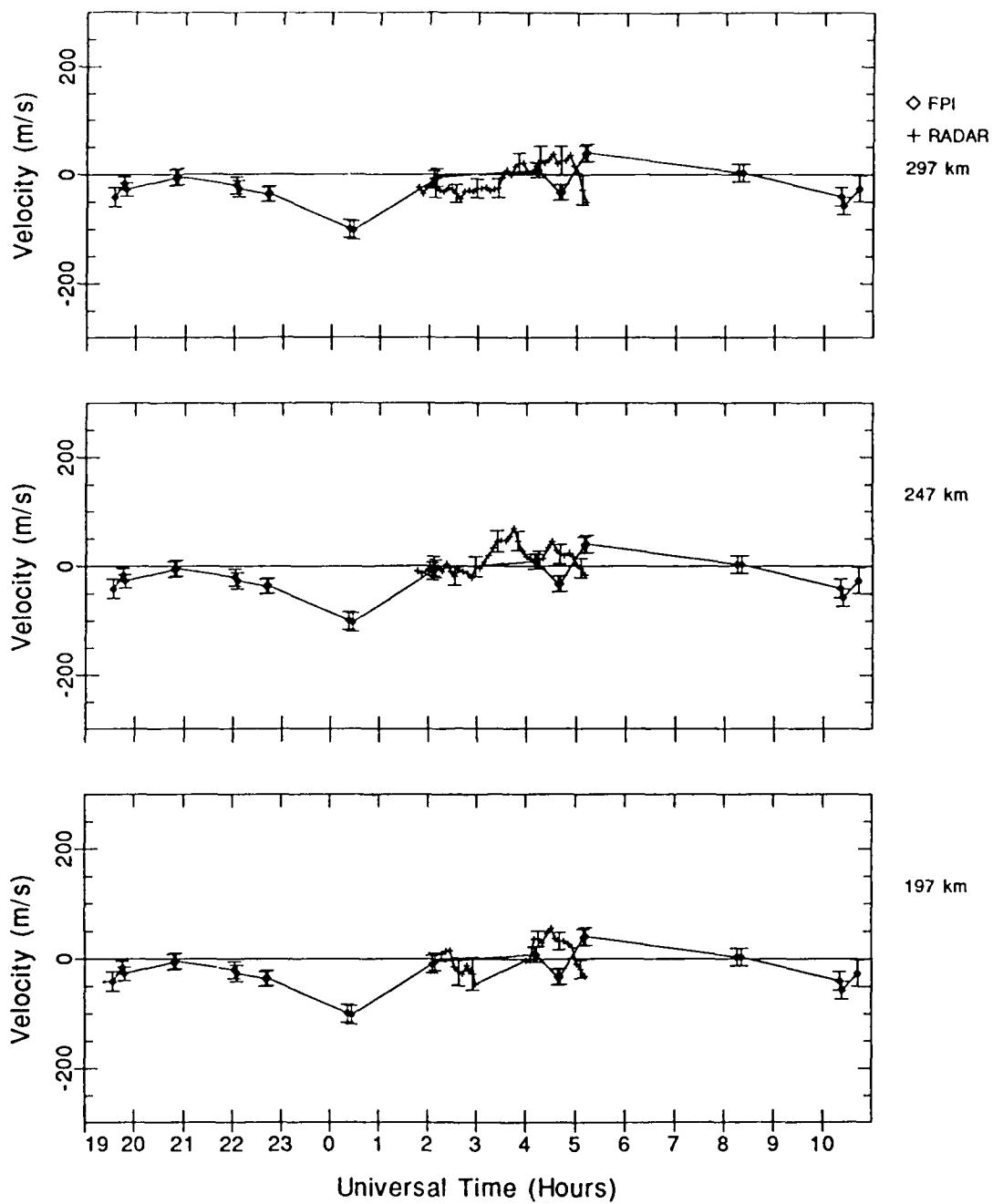
- Meriwether, J. W., Observations of thermospheric dynamics at high latitudes from ground and space, *Radio Sci.*, *18*, 1035-1052, 1983.
- Meriwether, J. W., P. Shih, T. L. Killeen, V. B. Wickwar, and R. G. Roble, Night-time thermospheric winds over Sondre StromFjord, Greenland, *Geophys. Res. Lett.*, *9*, 931-934, 1984.
- Meriwether, J. W., Jr., and P. Shih, On the nighttime signatures of thermospheric winds observed at Sondrestrom, Greenland, as correlated with interplanetary magnetic field parameters, *Annal. Geophys.*, *5A*, 329-336, 1987.
- Nagy, A. F., R. J. Cicerone, P. B. Hays, K. D. McWatters, and J. W. Meriwether, Simultaneous measurement of ion and neutral motions by radar and optical techniques, *Radio Sci.*, *9*, 315-321, 1974.
- Petersen, V. L., T. E. Van Zandt, and R. B. Norton, *F*-region night glow emissions of atomic oxygen, 1. Theory, *J. Geophys. Res.*, *71*, 2255-2265, 1966.
- Rees, M. H., and R. G. Roble, Excitation of O(<sup>2</sup>D) atoms in aurorae and emission of the OI 6300-A line, *Ann. J. Phys.*, 1608, 1986.
- Richmond, A., Thermospheric dynamics and electrodynamics, (R. L. Carovillano and J. M. Forbes, eds.), *Solar Terrestrial Physics*, 523-607, 1983.
- Rishbeth, H., Thermospheric winds in the F-region A review *J. Atmos. Terr. Phys.*, *34*, 1-47, 1972.
- Roble, R. G., The calculated and observed diurnal variation of the ionosphere over Millstone Hill on 23-24 Mar 1970, *Planet. Space Sci.*, *23*, 1017-1033, 1975.
- Schunk, R. W., The terrestrial ionosphere, (R. L. Carovillano and J. M. Forbes eds.), *Solar Terr. Phys.*, 609-676, 1983.
- Schunk, R. W., Polar Wind Tutorial, *Proceedings of the Cambridge Workshop*, 1988.
- Schunk, R. W., and J. C. G. Walker, Theoretical ion density in the lower ionosphere, *Planet. Space Sci.*, *21*, 1875-1896, 1973.
- Schunk, R. W., and A. Nagy, Electron temperatures in the *F*-region of the ionosphere: Theory and observations, *Rev. Geophys. Space Phys.*, *16*, 355-399, 1978.
- Sharp, W. E., Concerning sources of O(<sup>1</sup>D) in aurora: Electron impact and dissociative recombination, *J. Geophys. Res.*, *88*, 3229-3232, 1983.
- Sica, R. J., M. H. Rees, G. J. Romick, G. Hernandez, and R. G. Roble, Auroral zone thermospheric dynamics, 1., Averages, *J. Geophys. Res.*, *91*, 3231-3244, 1986.

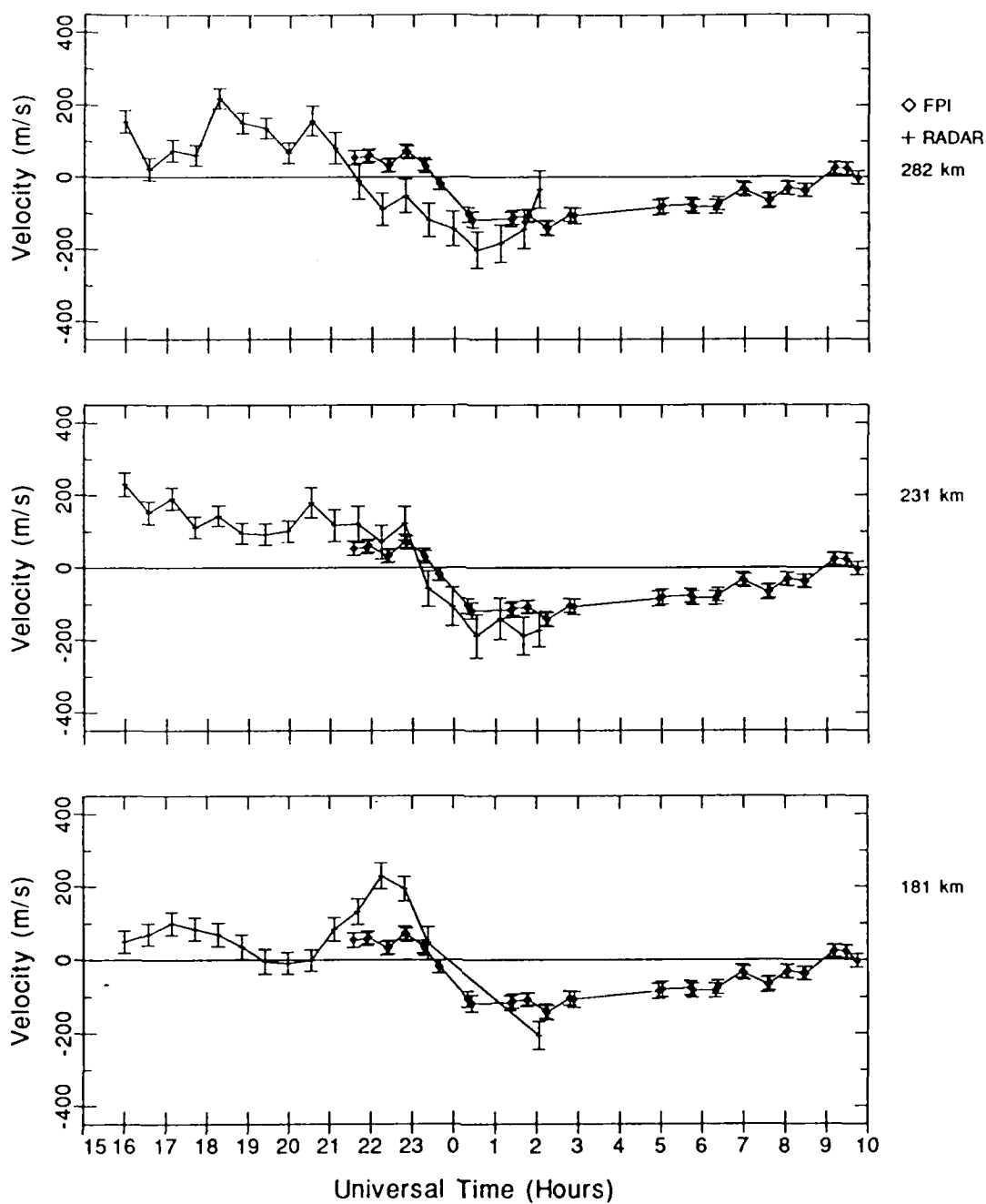
- Sipler, D. P., and M. E. Hagan, Comparisons of optical and radar measurements of F-region winds and temperatures at Millstone Hill, *EOS*, *70*, 43, 1243, Oct 24, 1989.
- Stebbing, R. F., A. C. H. Smith, H. Ebrhardt, Charge transfer between oxygen atoms and  $O^+$  and  $H^+$  ions, *J. Geophys. Res.*, *69*, 2349–2355, 1964.
- Testud, J., Gravity waves generated during magnetic substorms, *J. Atmos. Terr. Phys.*, *32*, 1793–1805, 1970.
- Thomas, D. P., and P. J. S. Williams, Measurements of ion-drag induced by plasma velocity in the F-region, *J. Atmos. Terr. Phys.*, *37*, 1271–1275, 1975.
- Vallance-Jones, A., *Aurora*, D. Reidel Publishing Co., Boston, Mass., 1974.
- Wallace, L., and M. B. McElroy, The visual dayglow, *Planet. Space Sci.*, *14*, 677–708, 1966.
- Wickwar, V. B., Thermospheric neutral wind at  $-39^\circ$  azimuth during the daytime sector at Sondrestrom, *Geophys. Res. Lett.*, *9*, 927–930, 1984.
- Wickwar, V. B., Global thermospheric studies of neutral dynamics using incoherent scatter radars, *Adv. Space Res.*, *9*, 87–102, 1989.
- Wickwar, V. B., L. L. Cogger, and H. C. Carlson, The 6300 Å  $O(^1D)$  airglow and dissociative recombination, *Planet. Space Sci.*, *22*, 709–724, 1974.
- Wickwar, V. B., C. Lathuillere, W. Kofman, and G. Lejeune, Elevated electron temperatures in the auroral *E* layer measured with the Chatanika Radar, *J. Geophys. Res.*, *86*, 4721–4730, 1981.
- Wickwar, V. B., and W. Kofman, Dayside red auroras at very high latitudes: The importance of thermal excitation, *Geophys. Res. Lett.*, *1*, 923–926, 1984.
- Wickwar, V. B., J. W. Meriwether, P. B. Hays, and A. F. Nagy, The meridional thermospheric neutral wind measured by radar and optical techniques in the auroral region, *J. Geophys. Res.*, *89*, 10,987–10,998, 1984a.
- Wickwar, V. B., J. D. Kelly, O. de la Beaujardiere, C. A. Leger, F. Steenstrup, and C. H. Dawson, Sondrestrom Overview, *Geophys. Res. Lett.*, *1*, 883–886, 1984b.
- Wickwar, V. B., R. G. Burnside, J. E. Salah, M. L. Duboin, and D. Alcayde, The meridional component of the thermospheric wind deduced from incoherent-scatter radar observations, submitted, 1990.

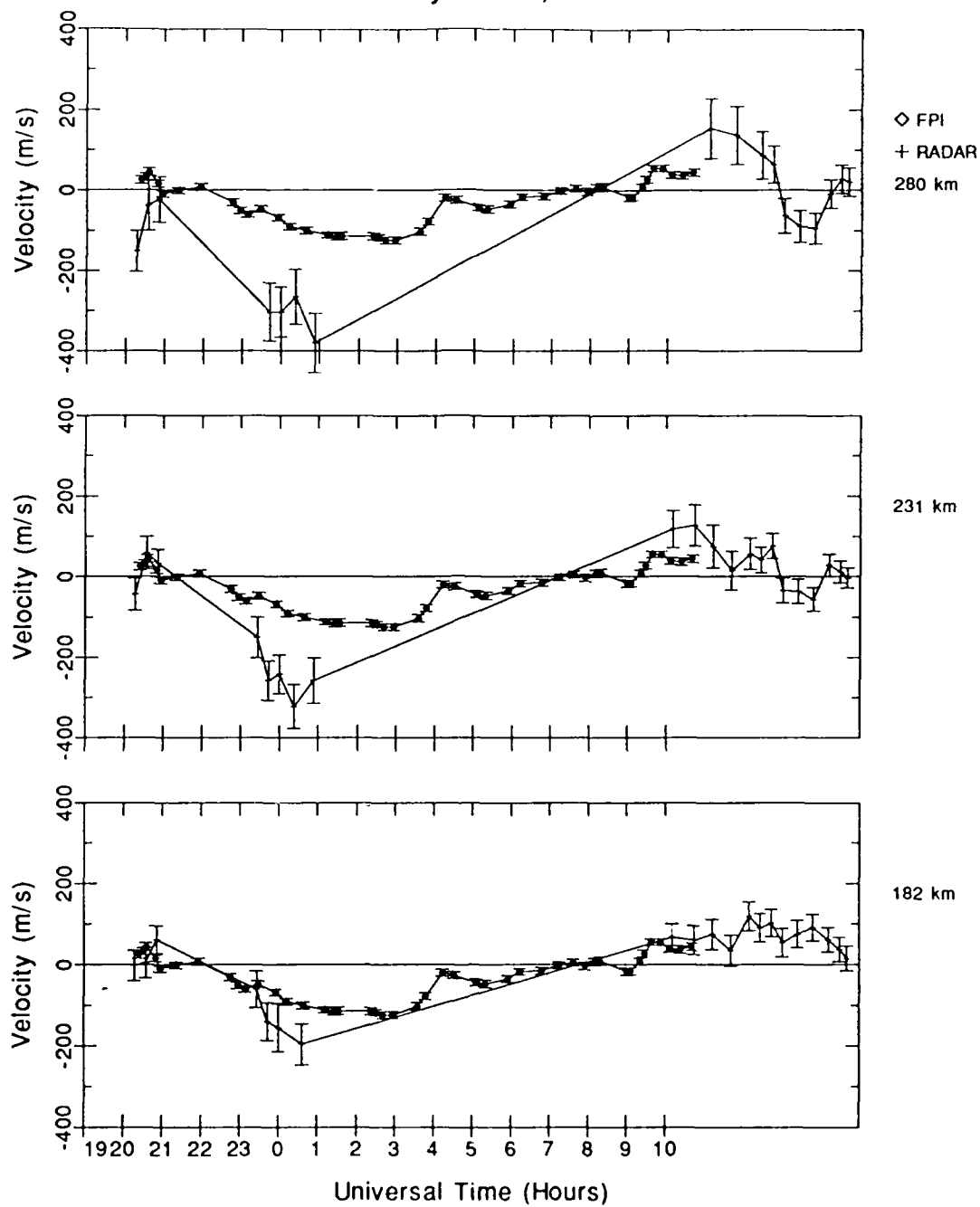
APPENDIX

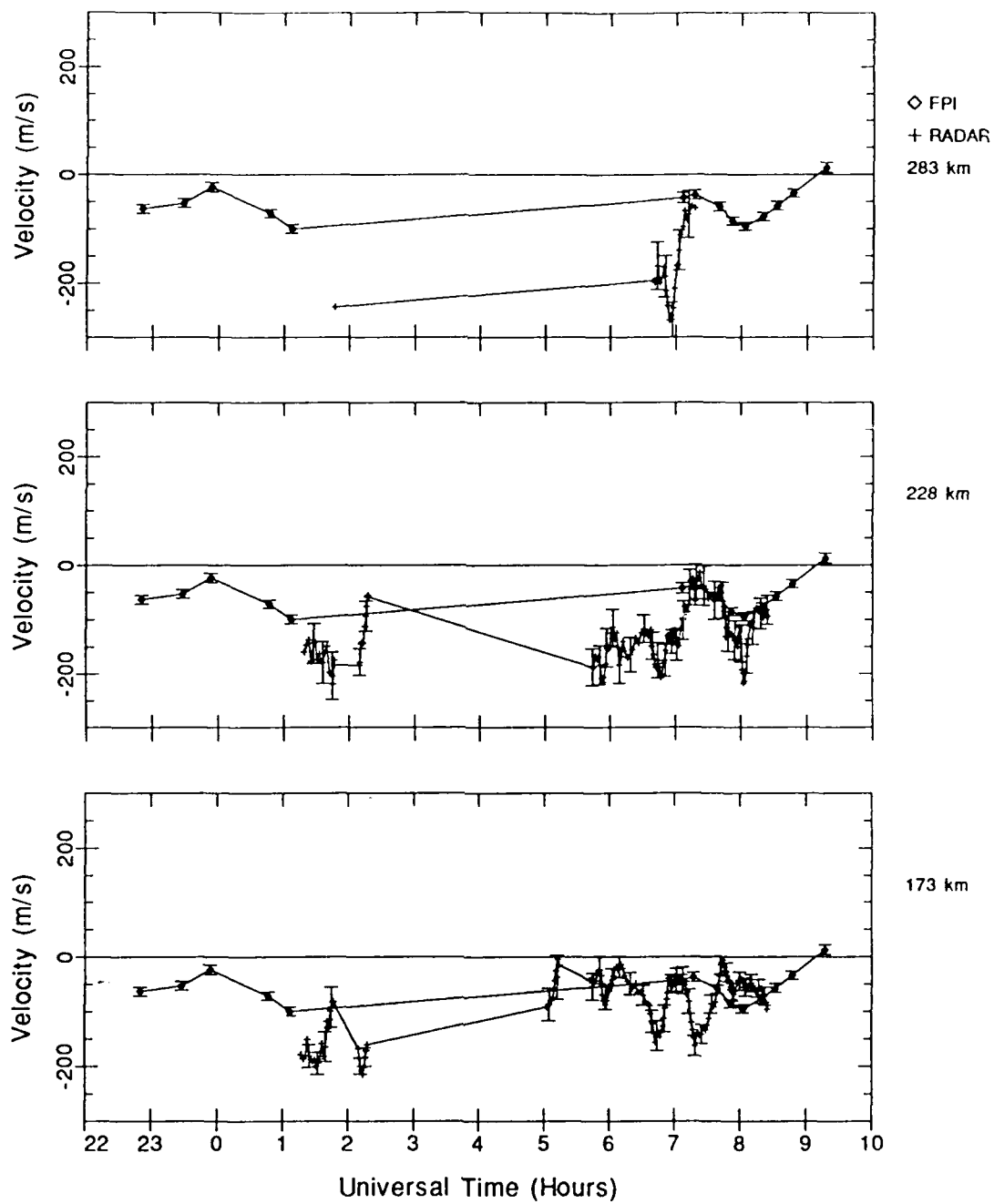
13 - 14 September 1983,  $f = 0.5$ 

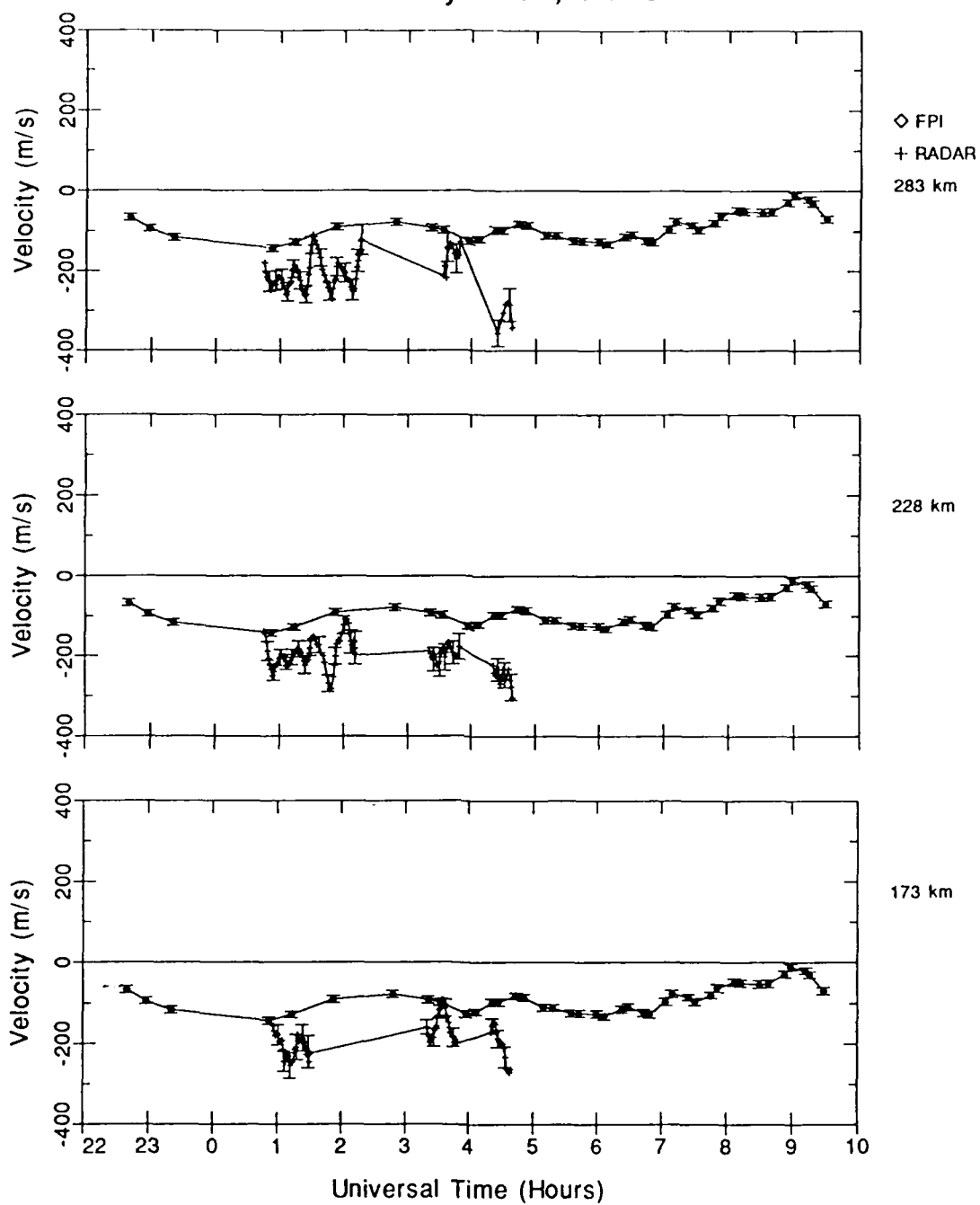
8 - 9 October 1983,  $f = 1.7$ 

6 - 7 November 1983,  $f > 5.1$ 

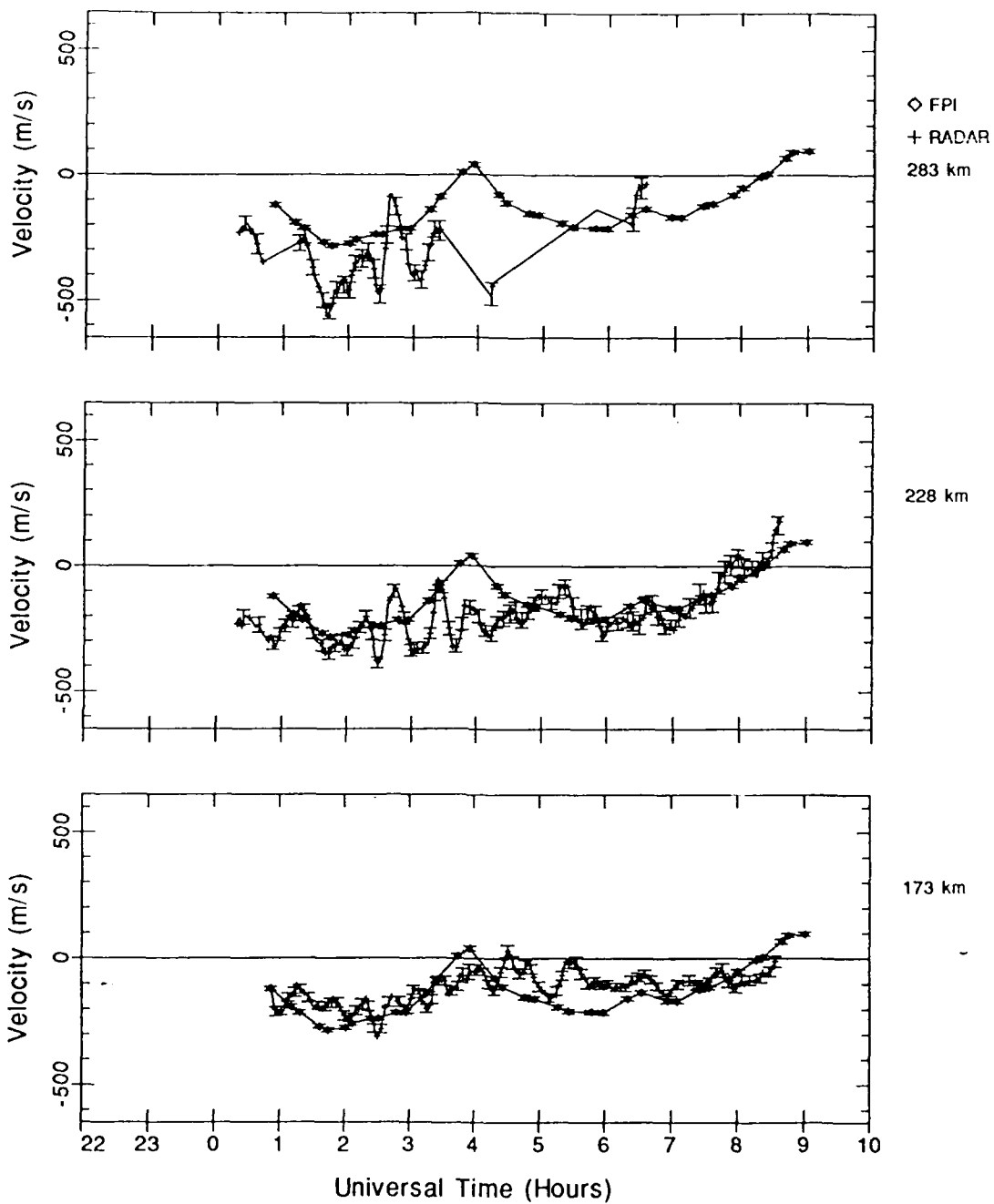
23 - 24 February 1984,  $f = 1.7$ 

28 - 29 January 1987,  $f = 1.7$ 

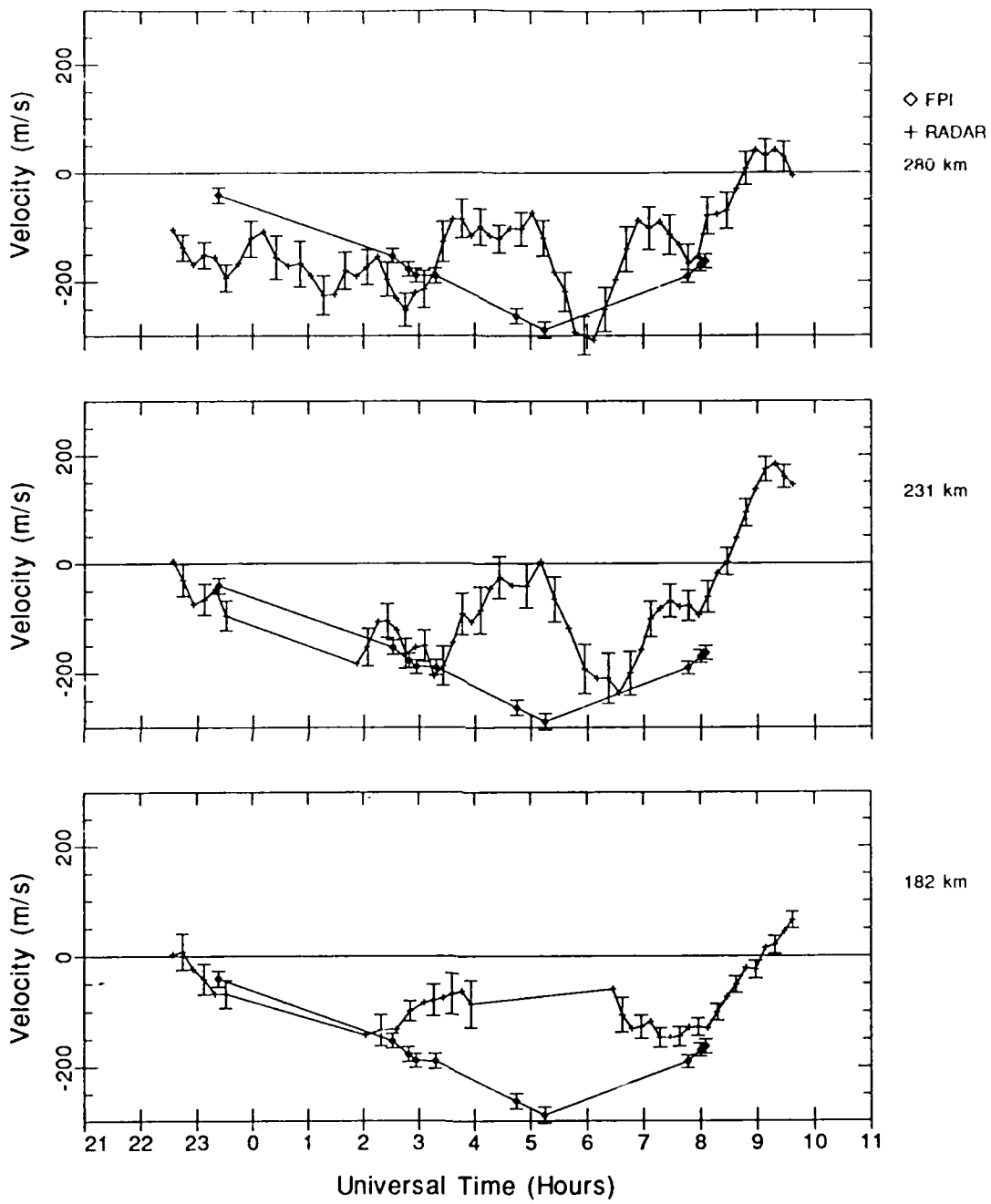
25 - 26 February 1987,  $f = 3.4$ 

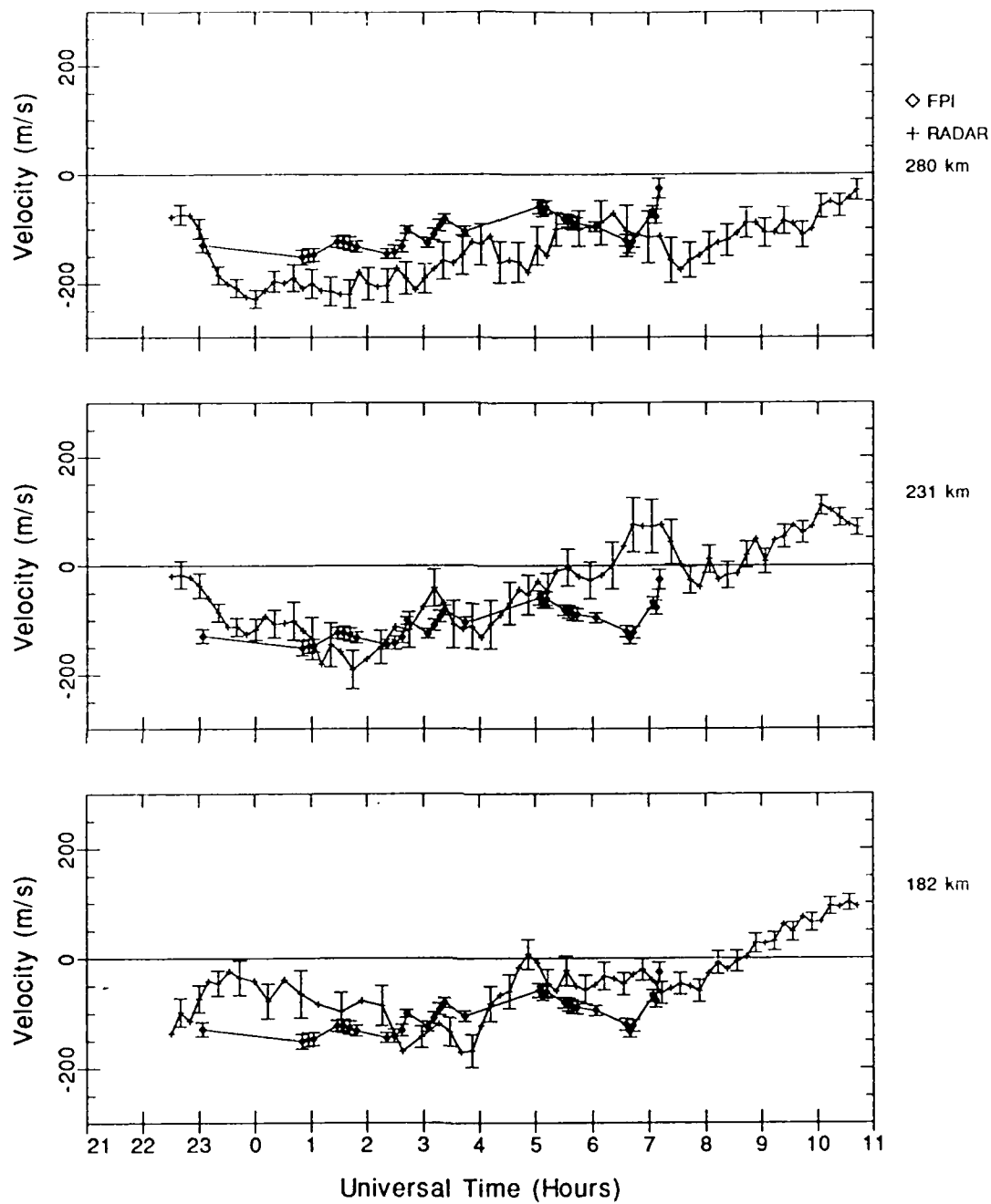
26 - 27 February 1987,  $f > 5.1$ 

3 - 4 March 1987,  $f = 3.4$



16 - 17 March 1988,  $f = 1.7$



17 - 18 March 1988,  $f = 1.0$ 

18 - 19 March 1988,  $f = 3.4$ 